2009

In-flight trajectory planning and guidance for autonomous parafoils

Branden James Rademacher
Iowa State University

In-flight trajectory planning and guidance for autonomous parafoils

by

Branden James Rademacher

A dissertation submitted to the graduate faculty

in partial fulfillment of the requirements for the degree of

DOCTOR OF PHILOSOPHY

Major: Aerospace Engineering

Program of Study Committee:
Ping Lu, Major Professor
Bion L. Pierson
Soon-Jo Chung
Jerald M. Vogel
Greg R. Leucke

Iowa State University

Ames, Iowa

2009

DEDICATION

I would like to dedicate this dissertation to my wife Elise without whose love and support I would not have been able to complete this work.

TABLE OF CONTENTS

LIST OF TABLES vi

LIST OF FIGURES viii

ABSTRACT xvi

CHAPTER 1. INTRODUCTION 1

1.1 Typical Mission Profile 5

1.2 The Parafoil Guidance Problem 5

1.3 Previous Work in Parafoil Guidance and Nonholonomic Trajectory Planning 6

1.4 Limitations of Current Parafoil GNC Algorithms 8

1.5 Research Objectives and Dissertation Overview 8

CHAPTER 2. PARAFOIL PERFORMANCE AND AERODYNAMICS 11

2.1 Introduction to the Parafoil 11

2.2 Fundamental Performance Parameters 14

2.3 Apparent Mass and Scale Effects 19

2.4 Parafoil Aerodynamics and Static Stability 22

CHAPTER 3. PARAFOIL MODELING 32

3.1 Parafoil Equations of Motion 32

3.2 Reduced-Order Model 35

3.2.1 Quasi-Equilibrium Glide Assumption 35

3.2.2 Change of Independent Variable 37

3.2.3 Wind-Fixed Coordinate Frame 38

3.3 Wind Field Modeling 39

CHAPTER 4. FIXED-TIME TRAJECTORY PLANNING 41

4.1 Optimal Control Problem 42

4.2 Minimum-Time Trajectories 44

4.3 A Necessary Condition 45

4.4 Minimum Control-Energy Paths 47

4.5 Solution and Sample Minimum Control-Energy Trajectories 49

4.6 Modified Dubins Paths 51

CHAPTER 5. REAL-TIME ON-BOARD WIND ESTIMATION . . . 59

5.1 Problem Formulation 59

5.2 Forming the Filter Measurements 62

5.3 Simulated Measurements 64

5.4 Wind Estimate Using Noisy Measurements Only 65

5.5 Wind Estimate Using a Fading Memory Filter 66

5.6 Wind Estimate Using a WNV Kalman Filter 67

5.7 Wind Estimate Using a WNA Kalman Filter 68

5.8 Wind Estimate Using a WPA Kalman Filter 70

CHAPTER 6. CLOSED LOOP GUIDANCE ALGORITHM 74

CHAPTER 7. TRAJECTORY TRACKING CONTROL 79

CHAPTER 8. SIMULATION RESULTS 82

8.1 Simulation Setup 82

8.2 Sensitivity to Sensor Noise 84

8.3 Sensitivity to Payload Mass Dispersion 86

8.4 Sensitivity to C_L and C_D Dispersions 88

8.5 Sensitivity to Wind Profile Errors 93

8.6 Performance With All Dispersions 97

8.7 Performance with Wind Estimation 101

CHAPTER 9. CONCLUSION 110

9.1 Contributions of this Study 111

9.2 Recommendations for Future Work 112

APPENDIX A. THE CONTINUOUS-DISCRETE KALMAN FILTER 113

APPENDIX B. PROCESS MODELS FOR TRACKING 116

APPENDIX C. UNBIASED POLAR-TO-CARTESIAN CONVERSION 121

APPENDIX D. THE UNSCENTED TRANSFORMATION 124

BIBLIOGRAPHY 126

LIST OF TABLES

Table 2.1 Summary of the effects of the fundamental performance parameters on parafoil motion. 20

Table 5.1 Typical measurement errors for low-cost, commercially available sensors. 62

Table 5.2 RMS measurement errors used in all simulations. 64

Table 5.3 The state vector, fundamental matrix, process noise covariance matrix, and measurement matrix for the WNV process model. . 69

Table 5.4 The state vector, fundamental matrix, process noise covariance matrix, and measurement matrix for the WNA process model. . 69

Table 5.5 The state vector, fundamental matrix, process noise covariance matrix, and measurement matrix for the WPA process model. . . 72

Table 8.1 Parameters used to generate C_L and C_D vs. symmetric brake deflection using Reference (37). 83

Table 8.2 Parameters required by the guidance algorithm and for the simulation. 84

Table 8.3 Sensor error statistics. 86

Table 8.4 Summary of simulation results for Parafoil 1 and Parafoil 2. The case listed as "All" includes sensor noise, 5% variation of payload mass, 5% variation of C_L and C_D, and 20% variation in wind. . . 100

Table 8.5 Summary of simulation results for Parafoil 2 using on-board wind estimation in an attempt to improve landing accuracy in the presence of unknown wind field variation. 108

Table C.1 Parameters required to compute the unbiased measurement conversion for cases where $\tilde{\psi}$ is uniformly and Gaussian distributed. 123

LIST OF FIGURES

Figure 1.1 An example of a traditional non-gliding parachute. Photo courtesy of NASA Langley Research Center. 2

Figure 1.2 An example of a parafoil in flight. This photo is of the NASA SpaceWedge system, a precursor to the X-38 program. Photo courtesy of NASA Dryden Flight Research Center. 3

Figure 2.1 Front view of the X-38 Crew Return Vehicle suspended under its 7500 ft^2 parafoil. This photo highlights the arc-anhedral common to parafoil rigging. Photo courtesy of NASA Dryden Flight Research Center. 12

Figure 2.2 Side view of the X-38 Crew Return Vehicle just prior to touchdown. A large symmetric flap deflection can clearly be seen. Photo courtesy of NASA Dryden Flight Research Center. 14

Figure 2.3 Forces and moments acting on a parafoil in a straight-line equilibrium glide. 16

Figure 2.4 Lift coefficient variation vs. angle of attack and symmetric flap deflection based on data from Ref. (37) for R/b=1.0 and an aspect ratio of 2.0. 23

Figure 2.5 Drag coefficient variation vs. angle of attack and symmetric flap deflection based on data from Ref. (37) for R/b=1.0 and an aspect ratio of 2.0. 24

Figure 2.6 Pitching moment coefficient about the quarter chord variation vs. angle of attack and symmetric flap deflection based on data from Ref. (37) for R/b=1.0 and an aspect ratio of 2.0. 25

Figure 2.7 Lift-to-drag ratio variation vs. angle of attack and symmetric flap deflection based on data from Ref. (37) for R/b=1.0 and an aspect ratio of 2.0. 26

Figure 2.8 Pitching moment coefficient about the system c.g. vs. angle of attack for various choices of the rigging angle at zero symmetric brake deflection. 27

Figure 2.9 Pitching moment coefficient about the system c.g. vs. angle of attack for various choices of the rigging angle at half symmetric brake deflection. 28

Figure 2.10 Pitching moment coefficient about the system c.g. vs. angle of attack for various choices of the rigging angle at full symmetric brake deflection. 29

Figure 2.11 Trim lift-to-drag ratio vs. rigging angle and symmetric brake deflection. 30

Figure 2.12 Tangent coefficient vs. rigging angle and symmetric brake deflection. 31

Figure 3.1 Force diagram for a parafoil in turning flight; fore view (left), side view (right). 33

Figure 4.1 Examples of Dubins paths: RSL (left), LSL (center), LRL (right). Note: the LRL path is not optimal in this example. The quantities t and q are the outer turn angles and the quantity p is the length of the straight line segment for type CSC paths and the middle turn angle for type CCC paths. 46

Figure 4.2 Minimum control-energy trajectories for an initial normalized altitude margin η=3, varying the initial heading. The initial position is the same for each case. 51

Figure 4.3 Minimum control-energy trajectories for the same initial configuration, varying the initial normalized altitude margin η from 0.2 to 2.2 in increments of 0.4. The dotted line corresponds to the minimal Dubins path. 52

Figure 4.4 This is an example trajectory with the initial position at the intended target and the initial heading opposite the required final heading. The normalized altitude margin for this example is 10. Note the symmetry of the trajectory about the downrange axis. . 53

Figure 4.5 Geometry and parameters used to calculate members of the Dubins set. 54

Figure 5.1 The relationship between the the airspeed vector V_A, the wind speed vector V_W, and the inertial velocity vector V_I. 60

Figure 5.2 The wind profile used to generate simulated sensor measurements. 65

Figure 5.3 The ground track of the nominal trajectory used to generate simulated sensor measurements. 66

Figure 5.4 Simulated sensor measurements for the nominal trajectory. . . . 67

Figure 5.5 Tracking errors using the unbiased converted measurements only along the x- (top) and y-axes (bottom). 68

Figure 5.6 Tracking errors using a first-order fading memory filter with β=0.85 along the x- (top) and y-axes (bottom). The dotted lines correspond to the predicted variance calculated using Eq. 5.17. 70

Figure 5.7 Tracking errors using a Kalman filter with a White Noise Velocity process model with Φ_s=1.0 along the x- (top) and y-axes (bottom). The dotted lines correspond to the square-root of the predicted variance estimate provided by the filter. 71

Figure 5.8 Tracking errors using a Kalman filter with a White Noise Acceleration process model with Φ_s=0.8 along the x- (top) and y-axes (bottom). The dotted lines correspond to the square-root of the predicted variance estimate provided by the filter. 72

Figure 5.9 Tracking errors using a Kalman filter with a Wiener Process Acceleration model with Φ_s=2.0 along the x- (top) and y-axes (bottom). The dotted lines correspond to the square-root of the predicted variance estimate provided by the filter. 73

Figure 6.1 Summary of the guidance logic. This sequence is performed at every guidance update. 77

Figure 6.2 An example of a case with a high initial altitude margin ($\eta \cong 7$) for a canopy with $L/D = 1$, $V_0 = 12m/s$, and $\dot{\psi}_{max} = 15°/sec$. The initial Dubins path portion of the energy management phase is clearly distinguished in the upper-left portion of the figure. The terminal phase of the trajectory can be seen in the lower-right portion of the figure. 78

Figure 8.1 This is the terminal phase of a typical closed-loop trajectory for Parafoil 1 in the presence of wind uncertainty. Observe that the true wind velocity magnitude (dark) is nearly half of the expected value (light) for most of the trajectory. 85

Figure 8.2 Landing dispersion results for Parafoil 1 for the case where the wind profile is perfectly known and navigation errors are present. Left: System with longitudinal and lateral control. Right: System with lateral control only. 87

Figure 8.3 Landing dispersion results for Parafoil 2 for the case where the wind profile is perfectly known and navigation errors are present. Left: System with longitudinal and lateral control. Right: System with lateral control only. 88

Figure 8.4 Landing dispersion results for Parafoil 1 for the case where the wind profile is perfectly known and the payload mass is varied $\pm 5\%$ (1σ) from the nominal value. Left: System with longitudinal and lateral control. Right: System with lateral control only. . 89

Figure 8.5 Landing dispersion results for Parafoil 2 for the case where the wind profile is perfectly known and the payload mass is varied $\pm 5\%$ (1σ) from the nominal value. Left: System with longitudinal and lateral control. Right: System with lateral control only. . 90

Figure 8.6 Landing dispersion results for Parafoil 1 for the case where the wind profile is perfectly known and the payload mass is varied $\pm 10\%$ (1σ) from the nominal value. Left: System with longitudinal and lateral control. Right: System with lateral control only. 91

Figure 8.7 Landing dispersion results for Parafoil 2 for the case where the wind profile is perfectly known and the payload mass is varied $\pm 10\%$ (1σ) from the nominal value. Left: System with longitudinal and lateral control. Right: System with lateral control only. 92

Figure 8.8 Landing dispersion results for Parafoil 1 for the case where the wind profile is perfectly known and the C_L and C_D are varied $\pm 5\%$ (1σ) from the nominal values. Left: System with longitudinal and lateral control. Right: System with lateral control only. 93

Figure 8.9 Landing dispersion results for Parafoil 2 for the case where the wind profile is perfectly known and the C_L and C_D are varied $\pm 5\%$ (1σ) from the nominal values. Left: System with longitudinal and lateral control. Right: System with lateral control only. 94

Figure 8.10 Landing dispersion results for Parafoil 1 for the case where the wind profile is perfectly known and the C_L and C_D are varied $\pm 10\%$ (1σ) from the nominal values. Left: System with longitudinal and lateral control. Right: System with lateral control only. 95

Figure 8.11 Landing dispersion results for Parafoil 2 for the case where the wind profile is perfectly known and the C_L and C_D are varied $\pm 10\%$ (1σ) from the nominal values. Left: System with longitudinal and lateral control. Right: System with lateral control only. 96

Figure 8.12 Landing dispersion results for Parafoil 1 for the case where there wind profile magnitude is in error by 20% of the nominal vehicle airspeed and the direction varies from 0 to 360°. Left: System with longitudinal and lateral control. Right: System with lateral control only. 98

Figure 8.13 Landing dispersion results for Parafoil 2 for the case where there wind profile magnitude is in error by 20% of the nominal vehicle airspeed and the direction varies from 0 to 360°. Left: System with longitudinal and lateral control. Right: System with lateral control only. 99

Figure 8.14 Landing dispersion results for Parafoil 1 for the case where there wind profile magnitude is in error by 40% of the nominal vehicle airspeed and the direction varies from 0 to 360°. Left: System with longitudinal and lateral control. Right: System with lateral control only. 101

Figure 8.15 Landing dispersion results for Parafoil 2 for the case where there wind profile magnitude is in error by 40% of the nominal vehicle airspeed and the direction varies from 0 to 360°. Left: System with longitudinal and lateral control. Right: System with lateral control only. 102

Figure 8.16 Landing dispersion results for Parafoil 1 for the case including navigation errors, wind uncertainty, and variations in aerodynamic performance and payload mass. Left: System with longitudinal and lateral control. Right: System with lateral control only. 103

Figure 8.17 Landing dispersion results for Parafoil 2 for the case including navigation errors, wind uncertainty, and variations in aerodynamic performance and payload mass. Left: System with longitudinal and lateral control. Right: System with lateral control only. 104

Figure 8.18 Landing dispersion results for Parafoil 2 with wind estimation for the case where the wind perturbation is constant. Left: wind error magnitude is uniformly distributed on [0,4] m/s, Right: wind error magnitude is uniformly distributed on [0,8] m/s. 105

Figure 8.19 Landing dispersion results for Parafoil 2 with wind estimation for the case where the direction of the wind perturbation is limited to be within a 15° window. Left: wind error magnitude is a first-order Markov process bounded by [0,4] m/s, Right: bounded by [0,8] m/s. 106

Figure 8.20 Landing dispersion results for Parafoil 2 with wind estimation for the case where the direction of the wind perturbation is limited to be within a 30° window. Left: wind error magnitude is a first-order Markov process bounded by [0,4] m/s, Right: bounded by [0,8] m/s. 107

Figure 8.21 Landing dispersion results for Parafoil 2 with wind estimation for the case where the direction of the wind perturbation is limited to be within a 60° window. Left: wind error magnitude is a first-order Markov process bounded by [0,4] m/s, Right: bounded by [0,8] m/s. 109

ABSTRACT

We present a framework for on-board trajectory planning and guidance for a large class of autonomously guided parafoils. The problem is for the parafoil to reach a given location at a specified altitude with a specified final heading. Through appropriate change of the independent variable, the trajectory planning problem is converted from a three-dimensional free-final time problem to a two-dimensional fixed-final time problem. Using the well-known Dubins path synthesis and known parafoil performance parameters a concept of altitude margin is developed as a quantitative measure of the available maneuvering energy for use in trajectory planning. A hybrid strategy using two methods to generate kinematically feasible fixed-time trajectories is presented, each targeting different range of initial values of the altitude margin. The trajectory can be re-planned on-board in every guidance cycle, making the guidance effectively closed loop, or re-planned whenever the deviation of the actual condition from the reference trajectory exceeds a threshold. The proposed planning and guidance algorithm applies to a large class of parafoil canopies and payloads which encompasses wide variations in the lift-to-drag ratio, wing loading, and maximum turn rate. The guidance logic requires no tuning to accommodate variations in canopy performance. Monte Carlo simulations are conducted to evaluate the effectiveness of the algorithm with dispersions in canopy performance, loading, wind profile errors, navigation uncertainty, using lateral control only and with both longitudinal and lateral control.

CHAPTER 1. INTRODUCTION

Autonomously guided parafoils offer a lightweight and efficient means for the delivery of cargo and supplies to specified ground coordinates. Conventional parachute systems use single or multiple clustered round canopies that descend vertically. Such systems are at the mercy of the wind as they have no ability to control horizontal motion. In contrast, parafoils and the broader class of gliding parachutes generate non-zero lift-to-drag (L/D) ratios and can achieve horizontal velocities that may exceed the vertical velocity. Most gliding parachutes also have some degree of turn control which when coupled with the glide capability gives the system the ability to compensate for wind and potentially steer toward a desired landing site. Such a parachute system coupled with an autonomous guidance and control system has far-reaching capability.

Both traditional and gliding parachute systems have many potential applications including military, scientific, and civil, with payloads ranging from a few pounds to many thousands of pounds. Military airdrop applications include the delivery of troops, supplies, and equipment to forward combat theaters and the resupply of troops in remote, inaccessible areas. Parachutes are also used to deliver munitions, sonar buoys, and electronic countermeasures and sensors. Scientific applications for parachute systems include the recovery of manned and unmanned spacecraft, recovery of sounding rockets or spacecraft booster components, recovery of high-altitude balloon payloads, and air-to-air retrieval of scientific payloads. Civil applications include airdrop of humanitarian aid, sport parachuting, and ejection seat stabilization and deceleration(1; 2). Examples of a traditional parachute and a parafoil are shown in Figures 1.1 and 1.2, respectively.

Figure 1.1 An example of a traditional non-gliding parachute. Photo courtesy of NASA Langley Research Center.

When a conventional parachute system is used, there are severe limitations placed on the size of the required landing zone, the altitudes from which the system can be deployed, and the region of acceptable release and/or deployment of the canopy, all due to uncertainty in the wind profile. To achieve acceptable landing accuracy in the presence of wind the system must be deployed from low altitudes (a few hundred to a few thousand feet) and from nearly overhead of the target. As the altitude of deployment increases, the size of the required landing zone (LZ) increases because the landing accuracy decreases. This is not ideal for many military applications as a low altitude deployment places the release aircraft and personnel at risk to ground fire. Low altitude deployment near the target also discloses the location of the LZ to the enemy which places covert operations at risk. Parachutes for recovery of scientific payloads from sounding rockets, balloons, or

Figure 1.2 An example of a parafoil in flight. This photo is of the NASA SpaceWedge system, a precursor to the X-38 program. Photo courtesy of NASA Dryden Flight Research Center.

spacecraft deploy at high altitude by necessity, making the potential landing dispersion quite large.

Steerable gliding parachutes offer many advantages over conventional parachute systems. The forward velocity allows the system to penetrate the wind field and minimize or eliminate the drift due to wind. This allows the system to be deployed from much higher altitudes and also significantly reduces the size of the required LZ. Furthermore, the gliding capability allows the system to be deployed at potentially large horizontal offsets from the target. This offers tactical and strategic advantage for military applications and logistic advantage for civil and scientific applications.

The parafoil, or ram-air parachute is a special class of gliding parachutes that when inflated resembles a low-aspect ratio wing. The parafoil is based on a kite design that

was discovered by D. Jalbert in the early 1960's. The University of Notre Dame refined the original Jalbert kite and coined the term parafoil which is a combination of parachute and airfoil (1). Parafoils can be steered and can achieve lift-to-drag ratios from 1 to 5, giving considerable glide performance. The use of autonomously guided parafoils for the precise placement of payloads was first considered in the 1960's. SSE Incorporated and ParaFlite developed the ParaPoint system which used a radio beacon located at the desired target to home in on the desired impact point (3). In the 1970's the U.S. Army Natick Research and Development Center began the development of technologies for autonomously guided parafoils (4). Systems in this era were primarily limited by the lack of navigation data and the non-availability of an on-board computer which prohibited implementation of an algorithm-based guidance scheme.

In the 1990's the Global Positioning System (GPS) was opened to the public and small embedded computer systems were increasingly available. In 1991 SSE Incorporated began development of the ORION Aiborne Delivery System which demonstrated the capability of flying parafoils from 288 ft^2 to 7360 ft^2 and payloads of 200 lb to 28,000 lb. The development program ended in 1995 and the production ORION system had a reported accuracy of 100 m (3). In 1994 the National Aeronautics and Space Administration (NASA) began a program to determine the feasibility of using a parafoil for the autonomous recovery of spacecraft during the final stages of reentry. The program began as the Spacecraft Autoland Project using the SpaceWedge vehicle and a sub-scale parafoil. The program eventually grew into the full-scale X-38 Crew Recovery Vehicle program (5). Concurrent to the NASA programs, the U.S. Army initiated the Guided Parafoil Airborne Delivery System (GPADS) program to demonstrate the applicability of a high glide recovery system for the stabilization, deceleration, and precision landing of a wide variety of military payloads (6). Recent advances in canopy performance, embedded computer systems, and guidance algorithms have led to a number of new autonomous airdrop systems in use today (7) .

1.1 Typical Mission Profile

We will discuss the typical mission profile for an autonomous parafoil system deployed by an aircraft. Prior to being released from the aircraft, known information about the wind profile and system performance is used to calculate the optimal release point or an acceptable launch window. Upon leaving the aircraft a small high-speed drogue chute is often deployed to stabilize the initial descent. After a specified time interval or upon reaching a specified altitude the main parafoil canopy is deployed. Large canopies may be deployed in stages to ensure proper inflation. After canopy deployment is complete, the GNC software and hardware become active. The software may trim the canopy to eliminate turn bias due to canopy or rigging asymmetries. At this point the guidance and control software will take over and fly the system to the target.

1.2 The Parafoil Guidance Problem

The parafoil guidance problem is to generate a trajectory from a given initial configuration (position and heading) (x_0, y_0, ψ_0) at some altitude h_0 to a given a terminal position (x_f, y_f) or configuration (x_f, y_f, ψ_f) at some specified final altitude h_f. There are many challenges facing any guidance algorithm for autonomous parafoils. Unlike powered vehicles, parafoils generally have no ability to ascend. This means that only one attempt can be made at landing. Most parafoil systems use yaw rate or yaw acceleration as the primary means of control and thus have little or no ability to reduce the along-track trajectory tracking error. Furthermore, the turn response and glide performance can vary greatly depending on canopy size and loading, which may change from mission to mission. Another significant complication is that the wind profile has a profound impact on the motion of the system and is often not known in advance or may only be known approximately. The wind velocity at certain altitudes may exceed the vehicle airspeed, meaning that during certain portions of the flight the system may

not be able to make forward progress with respect to the ground. A good guidance algorithm must be robust to all of these adverse conditions. For a given canopy and loading, this is best accomplished by preserving maneuvering energy as long as possible in the trajectory.

There are many applications where it is desired to minimize the impact force upon landing. This requirement conflicts with the requirement to minimize the landing dispersion resulting from uncertainty in the wind profile. Overcoming wind uncertainty is best accomplished with a higher canopy loading which increases the system airspeed. The side effect is that both the horizontal and vertical airspeed are larger, increasing the impact force. Some systems such as the Onyx by Atair Aerospace(8) or the Screamer by Strong Enterprises(7) overcome this problem by using a smaller, higher loaded parafoil canopy to track to the target and dissipate excess altitude and then release a secondary non-gliding parachute over the target to achieve a soft landing. However, in certain missions the size of the parafoil or the extra weight of the secondary chute may not allow for this approach. In such instances, the alternative is to use a lower canopy loading and land with the vehicle airspeed vector pointed into the wind.

1.3 Previous Work in Parafoil Guidance and Nonholonomic Trajectory Planning

Several algorithms for parafoil guidance, navigation, and control (GNC) are found in the literature. The algorithms generate trajectories that typically fall into one of three categories. Waypoint based algorithms(9; 10) generate a sequence of waypoints to manage excess altitude and have various criteria for exiting the energy management phase and tracking to the target. Maneuver based algorithms(8) generate a reference glide-slope to the target, usually biased from the true system glide-slope to allow for wind uncertainty, and perform a sequence of maneuvers to maintain the reference glide-slope.

Path based algorithms(11; 12; 13) generate a continuous reference trajectory connecting the system position and orientation to the target, and the trajectory is usually parameterized by time or altitude. Other algorithms(14; 15) may use a hybrid combination of these methods, typically one for energy management and one for final tracking to the target. Most algorithms conduct planning in the plane and remove the influence of the wind by working in a wind-fixed coordinate frame. Some algorithms can handle additional constraints placed on the trajectory including the addition of specific geographic waypoints, obstacle or geographic area avoidance, and final heading constraints.

Parafoil dynamics are non-holonomic as instantaneous motion is constrained to be tangent to the velocity vector. There is a significant body of related research on non-holonomic path planning in the robotics community. The original work by Dubins(16) and subsequent work by Boissonnat, et al.(17) discuss minimum-time paths connecting two configurations for car-like vehicles with constant forward velocity and maximum turn rate constraints. This type of vehicle is commonly referred to as the the Dubins car, and the minimum-time paths are referred to as Dubins paths or Dubins curves. McGee, et al.(18) apply the Dubins path approach to find trajectories for unmanned aerial vehicles operating in a constant wind field. McNeely, et al.(19) generalize the result of McGee to include multiple waypoints in the trajectory. Larson, et al.(20) uses a Dubins path synthesis and dynamic programming to generate trajectories for UAVs to reach the final configuration at a specified time. A three-dimensional extension to Dubins' work is given by Sussmann(21). Liang, et al.(22) generate curvature bounded trajectories for Dubins car-like robots using cubic spirals. Moll(23) describes a method for finding minimal energy paths of constant length. Lu, et al.(24) use an optimal control synthesis to generate minimum-control (turn rate) trajectories for both free and fixed final heading cases in a free final time.

1.4 Limitations of Current Parafoil GNC Algorithms

The algorithms that generate trajectories with a fixed final heading are typically tailored to a specific parafoil canopy and payload, and would require modification to be applied to a different class of canopy and payload. For example, the algorithms in Refs. (11), (12), and (13) assume that the glide path angle and airspeed are constant during both straight-line and turning portions of the reference trajectory. This assumption works well for very large canopies which see little variation in airspeed and glide path angle even at the maximum turning rate. Smaller canopies, however, can see significant variation in both quantities and neglecting these variations in trajectory planning overestimates the glide performance of the system. As a second example, the algorithm in Ref. (9) generates a waypoint-based trajectory. The spacing of the waypoints and the tolerances for determining when a waypoint is considered reached need to be adjusted based on the minimum turn radius of the system which is dependent on the canopy and loading. The resulting trajectory also contains a series of possibly alternating turns of large magnitude that may not be suitable for larger canopies with limited maximum turn rates. In general, the available GNC algorithms are best applied to a restricted class of parafoils with a limited range of canopy performance. What is generally lacking is a unified guidance approach that performs well for a large class of parafoils and is easily adaptable to gross variations in the lift-to-drag ratio (L/D), wing loading (W/S), and maximum turn rate/acceleration.

1.5 Research Objectives and Dissertation Overview

In this dissertation we consider the parafoil trajectory planning problem with the final configuration fixed. The primary objective of this work is to devise a guidance algorithm that can easily be applied to a large class of parafoil canopies and payloads with minimal or no tuning to accommodate variations in canopy performance or loading.

The dissertation is organized into nine chapters with four supporting appendices. Chapter 1 introduces the parafoil guidance problem and reviews past work in the area. Chapter 2 introduces the parafoil in greater detail, focusing on the primary characteristics that affect parafoil motion. In Chapter 3 a reduced order parafoil model is developed for trajectory planning. Using this reduced order model, and a novel change of the independent variable, the trajectory planning problem is reduced from a three dimensional free-final time problem to a two-dimensional fixed-final time problem. In Chapter 4 we present an optimal control synthesis to solve the resulting boundary value problem. Using the well-known Dubins path result for minimum time trajectories we are able to define a parameter, the altitude margin, that is used by the guidance algorithm to determine if the specified final configuration is reachable and give a qualitative measure of the difficulty in reaching it. A necessary condition for the existence of a fixed time path is also derived. We present two methods for calculating fixed-time trajectories, one targeting the cases of very low or very high altitude margin, and the other for the rest of the cases. In Chapter 5 we present filter designs for measuring the local wind field from on-board the parafoil system. In Chapter 6 we present the guidance strategy used to determine which of the two trajectory types to generate. The guidance logic is parameterized directly on the parafoil canopy performance. In this way the guidance logic can be easily applied to a large class of parafoil canopies and payloads. In Chapter 7 we present a simple base-line trajectory tracking controller. In Chapter 8 we present the results from Monte Carlo simulations to predict the expected landing accuracy and determine the sensitivity of the proposed guidance algorithm to a number of potential disturbances. Monte Carlo simulations are performed using only lateral control and using both lateral and longitudinal glide-slope control. The results indicate that a significant improvement in landing accuracy can be obtained when longitudinal control is available. Chapter 9 gives some concluding remarks and proposes future work. Appendix A lists the equations for implementing a linear Kalman filter. Appendix B presents the stan-

dard process models used for tracking applications. Appendix C presents an unbiased polar-to-Cartesian conversion for transformation of noisy measurements. Appendix D presents the Unscented (Sigma-Point) Transformation which provides a means for approximating the mean and covariance of a random variable that undergoes a nonlinear transformation.

CHAPTER 2. PARAFOIL PERFORMANCE AND AERODYNAMICS

In this chapter we introduce the parafoil and key elements that affect the motion and behavior of the parafoil/payload system. We begin by discussing the parafoil canopy itself and methods for affecting trajectory control. Next we discuss three fundamental parameters that determine canopy performance. We continue with a discussion on the affects of so-called apparent mass and the effects of scale on canopy behavior. The chapter concludes with a discussion on canopy aerodynamics and static longitudinal stability which leads to conclusions on the effect of both rigging angle and symmetric flap deflection on longitudinal control.

2.1 Introduction to the Parafoil

Once inflated the parafoil resembles a low-aspect ratio wing. The canopy is made entirely of fabric with airfoil shaped ribs sewn chord-wise between the upper and lower surfaces, giving the canopy an airfoil cross section. The leading edge edge of the canopy is open over the stagnation region so that stagnation pressure maintains the inflated form. The planform is typically rectangular, but newer high-performance canopies have an elliptical planform. Suspension lines are attached to the ribs at multiple points both span-wise and chord-wise. The suspension lines distribute the weight of the payload on the canopy and maintain the chord-wise profile of the canopy's lower surface. In the span-wise direction, lines are typically rigged with a constant length leading to an

arc-anhedral, as shown in Figure 2.1. The anhedral is essential to provide directional stability(25).

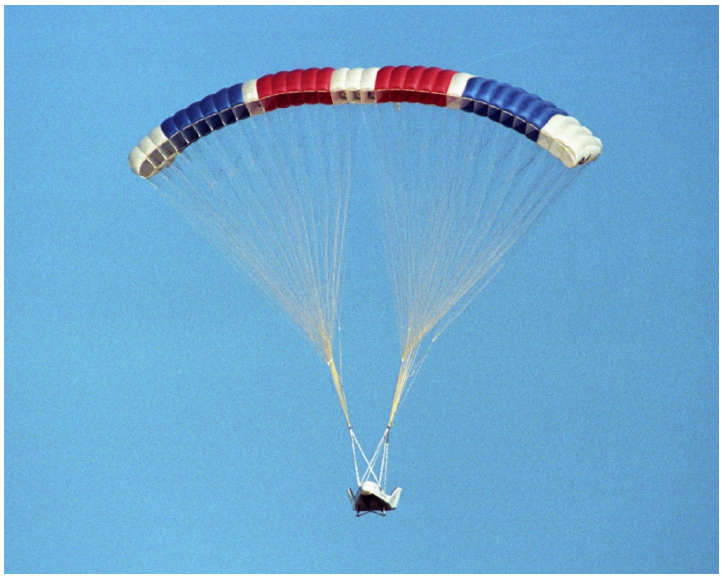

Figure 2.1 Front view of the X-38 Crew Return Vehicle suspended under its 7500 ft^2 parafoil. This photo highlights the arc-anhedral common to parafoil rigging. Photo courtesy of NASA Dryden Flight Research Center.

Parafoils generally have two control degrees of freedom. Lateral (directional) control can be achieved by two different means. The first method is referred to as canopy tilt and is achieved by deflecting the outer edge of the the canopy on the side inboard of the desired turn. Physically this is accomplished by shortening the suspension lines attached to the edge of the canopy. The result is a decrease in lift on the deflected side which effectively tilts or rolls the canopy and the lift force into the turn (26; 27). The second method of lateral control is achieved by an asymmetric deflection of portions of the trailing edge of the canopy. The deflected portions of the canopy are referred to as flaps or brakes and typically include the outer quarter of the trailing edge. A photo showing a parafoil with a symmetric flap deflection is given in Figure 2.2. The effect

of an asymmetric flap deflection depends on the magnitude of the deflection and the rigging of the canopy. In general the flap deflection generates only a small increase in lift and a large increase in drag on the deflected side, inducing a yaw moment rather than a roll moment as occurs on a conventional aircraft. The drag differential creates a sideslip angle which creates a side-force which rolls the canopy into the turn. The yaw moment from the flap deflection is eventually balanced out by the adverse yaw moment due to yaw rate, resulting in a steady-state turn. Depending on the canopy and rigging, analytical and experimental results in (28) and (29) show that small flap deflections can lead to control reversal, i.e. turn rates in the opposite direction of the desired turn. This problem can be overcome by flying with a sufficient non-zero symmetric flap deflection, however this may cause a small decrease in glide performance. Asymmetric flap deflection is by far the most common method of turn control used in practice.

Longitudinal control can also be achieved by two different means. The first is by changing the canopy rigging angle φ which is defined in Figure 2.3. This alters the trim angle of attack which effects both the lift-to-drag ratio (thus glide path angle) and the glide airspeed. Changing the rigging angle in flight requires lengthening or shortening the suspension lines along the leading and trailing edges of the canopy. This is a nontrivial feat and is most easily accomplished only on smaller canopies. Rigging angle modulation was demonstrated in flight for a small-scale parafoil system in Ref. (15). Great care must be used in implementing such a scheme as incorrect rigging can lead to stall onset, leading edge collapse, unintentional re-trimming at multiple angles of attack, and loss of lateral stability(30). The second means of longitudinal control is achieved by a symmetric deflection of the flaps. Small symmetric deflections typically increase both lift and drag proportionately so that L/D changes very little, essentially resulting in a change in glide airspeed but no change in glide path angle. Larger symmetric flap deflections often do effect L/D and thus glide path angle, but the magnitude of the effect is dependent on the canopy and rigging (31; 30; 32). This will be discussed in more detail in Section 2.4.

Figure 2.2 Side view of the X-38 Crew Return Vehicle just prior to touchdown. A large symmetric flap deflection can clearly be seen. Photo courtesy of NASA Dryden Flight Research Center.

2.2 Fundamental Performance Parameters

Parafoil canopies range from less than a square meter to over a thousand square meters, and payloads may range from a few kilograms to over 20 metric tons. Even with gross variations in canopy and payload sizes, to a large degree the gliding performance and macro-scale motion behavior of the canopy/payload motion are well described by three key parameters: the lift to drag ratio (L/D), the wing loading (W/S), and the maximum turn rate ($\dot{\psi}_{\max}$). We shall discuss the effects of each in turn.

Consider a parafoil in a straight-line equilibrium glide as shown in Figure 2.3. Here, V is the glide velocity, γ is the flight path angle (negative as shown), L_c is the lift force generated by the canopy, and D_c and D_p are the drag forces acting on the canopy and

payload, respectively. Summing the forces in the horizontal and vertical directions, the equilibrium condition is given by

$$0 = -L_c \sin\gamma - (D_c + D_p)\cos\gamma \tag{2.1}$$

$$(m_c + m_p)g = L_c \cos\gamma - (D_c + D_p)\sin\gamma \tag{2.2}$$

where m_c and m_p are the canopy and payload mass, respectively, and g is the acceleration due to gravity. The lift and drag forces can be written in non-dimensional form as

$$L = L_c = 0.5\rho V^2 S C_L \tag{2.3}$$

$$D = (D_c + D_p) = 0.5\rho V^2 S C_D \tag{2.4}$$

where ρ is the density of the air, S is the canopy reference area and the quantity $0.5\rho V^2$ is the dynamic pressure. Using Eq. 2.1 we see that

$$\tan\gamma = -\frac{1}{L/D} \tag{2.5}$$

which is the standard equation of efficiency in gliding flight. Eq. 2.5 implies that as the lift-to-drag ratio increases the flight path angle becomes shallower, allowing the system to glide farther for a given altitude loss. Eq. 2.5 also implies that the glide angle is independent of the wing loading and air density. Thus in the absence of wind a given canopy has the same glide range for a given change in altitude regardless of the payload weight.

If we square both Eq. 2.1 and Eq. 2.2, add the results, and simplify we can show

$$W = (L^2 + D^2)^{0.5} \tag{2.6}$$

where $W = (m_c + m_p)g$. This can also be written in coefficient form as

$$W = 0.5\rho V^2 S (C_L^2 + C_D^2)^{0.5} \tag{2.7}$$

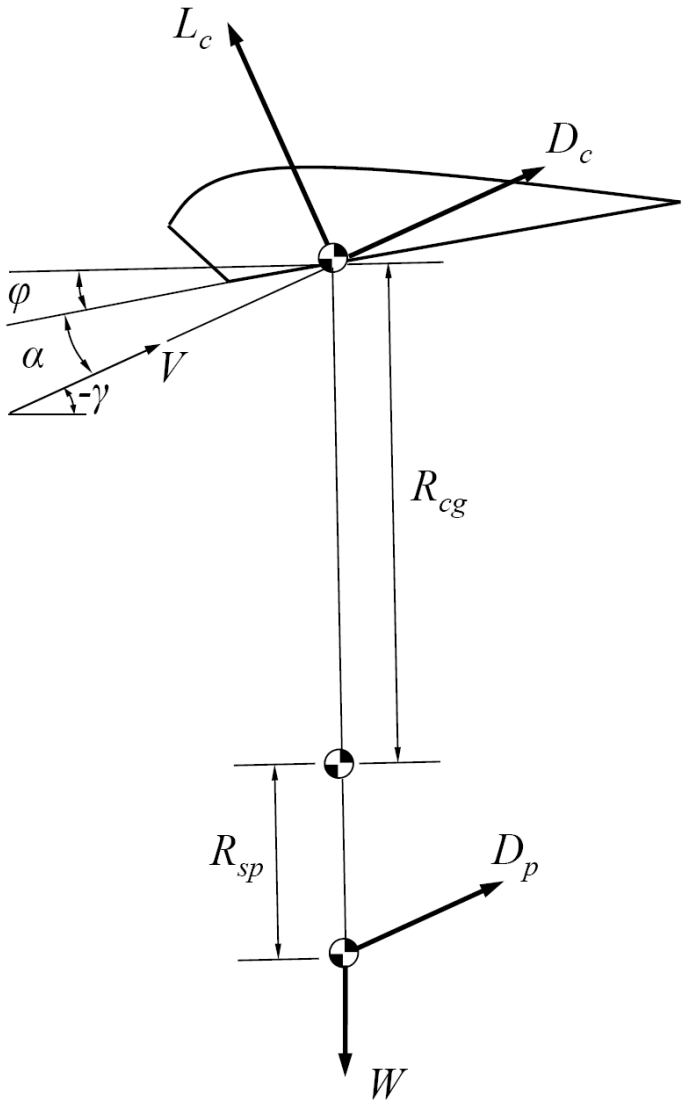

Figure 2.3 Forces and moments acting on a parafoil in a straight-line equilibrium glide.

where C_L and C_D are the lift and drag coefficients, respectively. We define the so-called tangent coefficient as

$$C_T = (C_L^2 + C_D^2)^{0.5} \tag{2.8}$$

so that Eq. 2.7 can be written as

$$W = 0.5\rho V^2 S C_T \tag{2.9}$$

The straight-line equilibrium glide velocity is then given by

$$V = \left(\frac{2}{\rho}\frac{W}{S}\frac{1}{C_T}\right)^{0.5} \tag{2.10}$$

An equilibrium glide will maintain constant dynamic pressure, thus C_T in Eq. 2.10 will remain constant. The value of C_T is dependent on the canopy rigging and lift-to-drag ratio and does not generally change from flight to flight. Eq. 2.10 indicates that the glide velocity is dependent on the air density (and thus altitude) and wing loading. As the altitude decreases the air density increases, decreasing the glide velocity. The velocity also increases with the square-root of wing loading.

The glide velocity can be broken into horizontal and vertical components as follows:

$$V_{xy} = V\cos\gamma \tag{2.11}$$

$$V_z = V\sin\gamma \tag{2.12}$$

where V_{xy} is the horizontal component and V_z is the vertical component. The horizontal component of the glide velocity determines the maximum wind velocity the system can penetrate and still make forward progress with respect to the ground. The vertical velocity, also called the sink rate, determines the the impact force upon landing. This implies that for a given wing loading, increasing L/D increases the ability to penetrate wind, decreases the landing impact velocity, and increases the duration of the flight from a given starting altitude. Furthermore, it can be seen for a given L/D that increasing the

wing loading also increases the ability to penetrate wind, increases the landing impact velocity, and decreases the duration of the flight from a given starting altitude.

The lift-to-drag ratio and wing loading play critical roles in determining the maximum glide distance in a non-zero wind field. In the presence of a constant horizontal wind field with velocity V_w, the horizontal velocity of the parafoil relative to the ground is $V_{xy} + V_w$. The glide angle with respect to the ground γ_w is given by

$$\tan \gamma_w = \frac{V_z}{V_{xy} + V_w} \tag{2.13}$$

or equivalently

$$\cot \gamma_w = \frac{V_{xy}}{V_z} + \frac{V_w}{V_z} \tag{2.14}$$

Using Eqs. (2.11) and (2.12) we can rewrite Eq. (2.14) as

$$\cot \gamma_w = -\frac{L}{D} + \frac{V_w}{V_z} \tag{2.15}$$

Maximizing the glide distance equates to minimizing $\cot \gamma_w$ (recall $\gamma_w < 0$). We see that when flying with the wind ($V_w > 0$), maximizing glide distance requires a large lift-to-drag ratio and small descent rate (V_z) which implies low wing loading. When flying into the wind ($V_w < 0$), maximizing the glide distance requires a large lift-to-drag ratio and a large descent rate which implies high wing loading.

For a given lift-to-drag ratio and wing loading, the maximum turn rate determines the minimum turn radius which is a direct measure of the maneuvering capability of the system. Furthermore, in Chapter 4 we will show that the minimum turn radius is critical in determining whether a given landing site is reachable from a given position and altitude.

In general the velocity of the system increases and the glide path angle steepens monotonically with the turn rate magnitude. This relationship will be discussed in more detail in the next chapter. For now we will denote the equilibrium velocity in a turn as

V_T and the equilibrium glide path angle as γ_T. Then the horizontal and vertical velocity components in a turn can be written as

$$V_{xy,T} = V_T \cos\gamma_T \tag{2.16}$$

$$V_{z,T} = V_T \sin\gamma_T \tag{2.17}$$

From standard kinematics, the turn rate $\dot{\psi}$ is related to the horizontal velocity and the turn radius r by the relation

$$\dot{\psi} = \frac{V_{xy,T}}{r} \tag{2.18}$$

which implies that the minimum turning radius $r_{\min}$ is given by

$$r_{min} = \frac{V_{xy,T}}{\dot{\psi}_{max}} \tag{2.19}$$

The effects of L/D and wind loading on $V_{xy,T}$ are the same as the effects on V discussed above. Thus we see that increasing L/D and wing loading and decreasing $\dot{\psi}_{max}$ increase the minimum turn radius.

The effects of the fundamental performance parameters on parafoil motion are summarized in Table 2.1.

2.3 Apparent Mass and Scale Effects

The parafoil canopy is a very light structure that is far removed from the center of mass of the parafoil/ payload system. As such, parafoil motion is strongly influenced by the so-called apparent mass effects of the surrounding air. Apparent mass effects arise from resistance of a fluid to changes in the motion of a body moving within the fluid. Since the fluid particles resist acceleration, accelerating the body requires additional forces over and above those that would be required to accelerate the body in a vacuum. The resulting motion of the body is as if it had a larger mass, where the apparent additional mass is due to the forces required to accelerate the fluid. The study of

Parameter	Large/Increasing	Small/Decreasing
L/D	Shallower flight path angle	Steeper flight path angle
	Larger glide distance	Smaller glide distance
	Increasing horizontal velocity	Decreasing horizontal velocity
	Decreasing descent rate	Increasing descent rate
	Increases minimum turn radius	Decreases minimum turn radius
W/S	Increasing airspeed	Decreasing airspeed
	Increasing descent rate	Decreasing descent rate
	Increases glide distance in a following wind	Decreases glide distance in a following wind
	Decreases glide distance in a head wind	Increases glide distance in a head wind
	Increases minimum turn radius	Decreases minimum turn radius
$\dot{\psi}_{max}$	Decreasing minimum turn radius	Increasing minimum turn radius

Table 2.1 Summary of the effects of the fundamental performance parameters on parafoil motion.

apparent mass effects on parafoil motion was first discussed by Lissaman and Brown in (33) which also gives analytical expressions for approximating the apparent mass terms for a flat-rigged canopy. They show that for a typical canopy the apparent roll inertia is about five times that of the payload-canopy system itself. Lissaman and Brown also show that apparent mass grows with the cube of dimension, as compared to aerodynamic forces which grow with the square of dimension. This has strong implications on system scale. The origins of apparent mass forces are discussed at length in Ref. (34). Barrows gives expressions for calculating the apparent mass terms for a canopy rigged with arc-anhedral in Ref. (35) by applying corrections to the apparent mass term expressions of Lissaman and Brown.

The preceding discussion indicates that apparent mass effects impact the transient response of the system to disturbances and control input. Analysis by Brown in Ref. (36) indicates that apparent mass forces also play a critical role in determining the steady-state response to turn-control input. Brown shows as canopy size increases the true bank angle becomes significantly less than the bank angle required for a coordinated turn, resulting in a skid. The flight path angle is also shallower than would be expected for a given turn rate. Brown explains this as follows. Turning flight is accelerated motion in an inertial frame and larger turn rates require larger accelerations of the surrounding fluid. Thus the apparent mass increases, causing a displacement between the true center of mass and the apparent center of mass, creating an anti-roll moment. As mentioned above, the apparent mass grows with the cube of dimension so larger canopies see a larger anti-roll moment and thus experience flatter turns. Brown also shows that the sensitivity of the canopy to control deflection is dependent on the canopy size, with small, highly loaded canopies tending to be extremely sensitive and almost twitchy, and large canopies having an overly sluggish response.

2.4 Parafoil Aerodynamics and Static Stability

The system lift-to-drag ratio is determined by the trim angle-of-attack which, in turn, is determined by the position of the payload and the rigging of the canopy. The trim angle-of-attack is defined as the angle-of-attack where the sum of the moments acting on the system is zero and will be stable when the slope of the moment curve is negative.

The lift, drag, and pitching moment coefficients about the quarter chord with respect to angle of attack and flap deflection are given in Ref. (37) for an example parafoil canopy. The data correspond to a canopy with an aspect ratio of 2.0 and line length-to-span ratio (R/b) of 1.0. The lift, drag, and moment coefficients versus angle-of-attack are shown in Figures 2.4, 2.5, and 2.6, respectively. The lift-to-drag ratio versus angle-of-attack is shown in Figure 2.7.

We see from Figure 2.4 the initial stall at zero brakes occurs at approximately α =10 degrees and is relatively gentle. As α continues to increase there is a second peak near α =25 degrees. The lift coefficient decreases as α increases from 25 to 35 degrees and then remains roughly constant as α increases from 35 to 50 degrees. The effect of symmetric brake deflection is generally to shift the C_L–α curve up. We see for this canopy that increasing the symmetric brake deflection from half brakes to full brakes does not increase the maximum lift coefficient, but does reduce the stalling angle-of-attack.

Figure 2.5 shows that the drag polar strongly resembles the parabolic profile for traditional airfoils. We see minimum drag occurs at negative angle-of-attack and the effect of symmetric brake deflection is an upward shift of the C_D–α curve. We see from Figure 2.6 the effect of symmetric brake deflection is a downward shift of the $C_{m_{c/4}}$–α curve, increasing the strength of the pitching moment.

Figure 2.7 shows that maximum L/D is achieved at approximately α=8 degrees and falls off rapidly as α increases further. We see that increasing symmetric brake deflection from zero to half brakes causes a small decrease in the maximum achievable L/D and

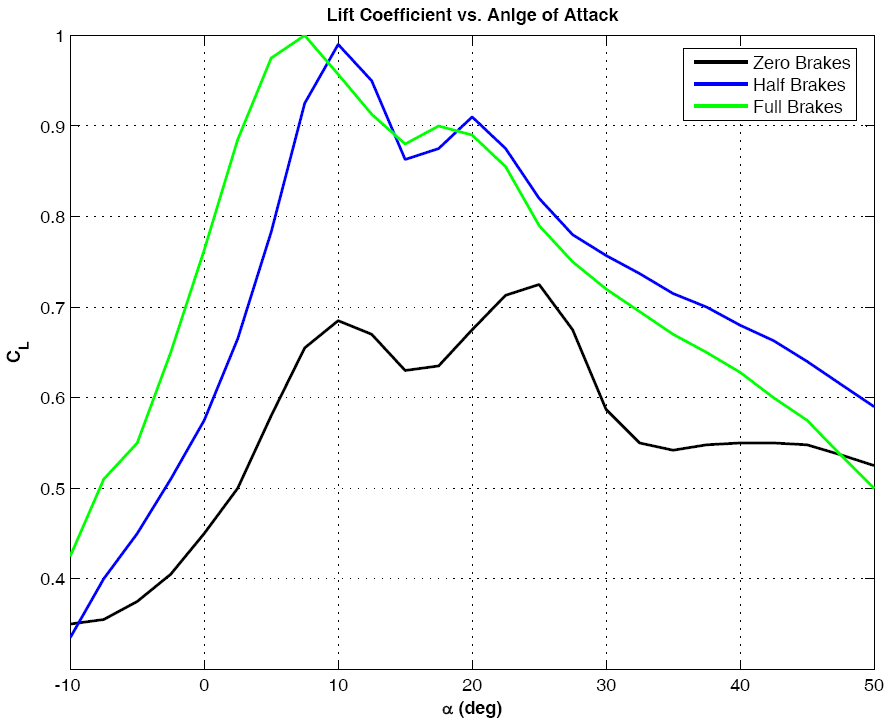

Figure 2.4 Lift coefficient variation vs. angle of attack and symmetric flap deflection based on data from Ref. (37) for R/b=1.0 and an aspect ratio of 2.0.

has almost no effect on the angle of attack where maximum L/D occurs. Increasing the brake deflection from half to full brakes causes a further reduction in the maximum achievable L/D, and the maximum L/D is achieved at a smaller angle of attack.

Using Figure 2.3, the pitching moment about the c.g. can be written

$$M = M_{c/4} + R_{cg}\left(D_c \cos(\alpha+\phi) - L_c \sin(\alpha+\phi)\right) - R_{pg} D_s \cos(\alpha+\phi) \tag{2.20}$$

where $M_{c/4}$ is the aerodynamic pitching moment about the quarter chord, R_{cg} is the distance from the canopy c.g. to the system c.g., D_c is the drag of the canopy, L_c is the lift of the canopy, R_{pg} is the distance from the payload c.g. to the system c.g., D_p is the drag of the payload, ϕ is the rigging angle, and α is the angle-of-attack. Eq. 2.20 assumes the system is rigid, the canopy and line mass are lumped at the quarter chord

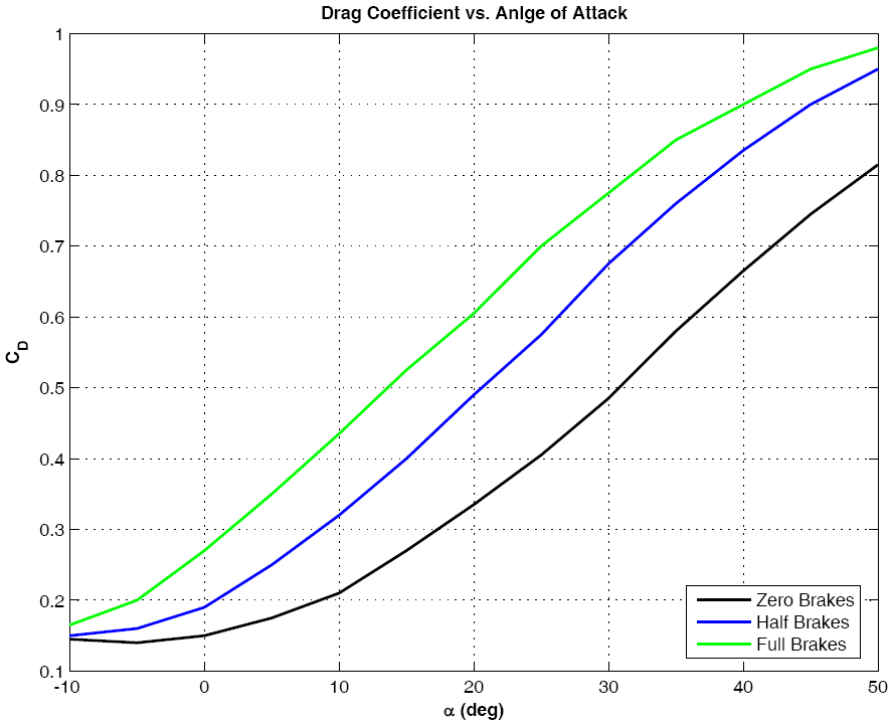

Figure 2.5 Drag coefficient variation vs. angle of attack and symmetric flap deflection based on data from Ref. (37) for R/b=1.0 and an aspect ratio of 2.0.

point, and the canopy force and moment terms include the effects of the lines.

The pitching moment can be written in coefficient form as

$$M = 0.5\rho V^2 ScC_m \tag{2.21}$$

where C_m is the pitching moment coefficient and c is the reference chord length of the canopy. Eq. 2.20 can then be written as

$$C_m = C_{m_{c/4}} + R_{cg}\left(C_{D_c}\cos(\alpha+\phi) - C_L\sin(\alpha+\phi)\right) - R_{pg}C_{D_s}\cos(\alpha+\phi) \tag{2.22}$$

where $C_{m_{c/4}}$ is the pitching moment coefficient of the canopy about the quarter chord point.

Using Eq. 2.22 and the lift, drag, and moment data from Figures 2.4, 2.5, and 2.6, the pitching moment coefficient about the system c.g. has been calculated for various rigging

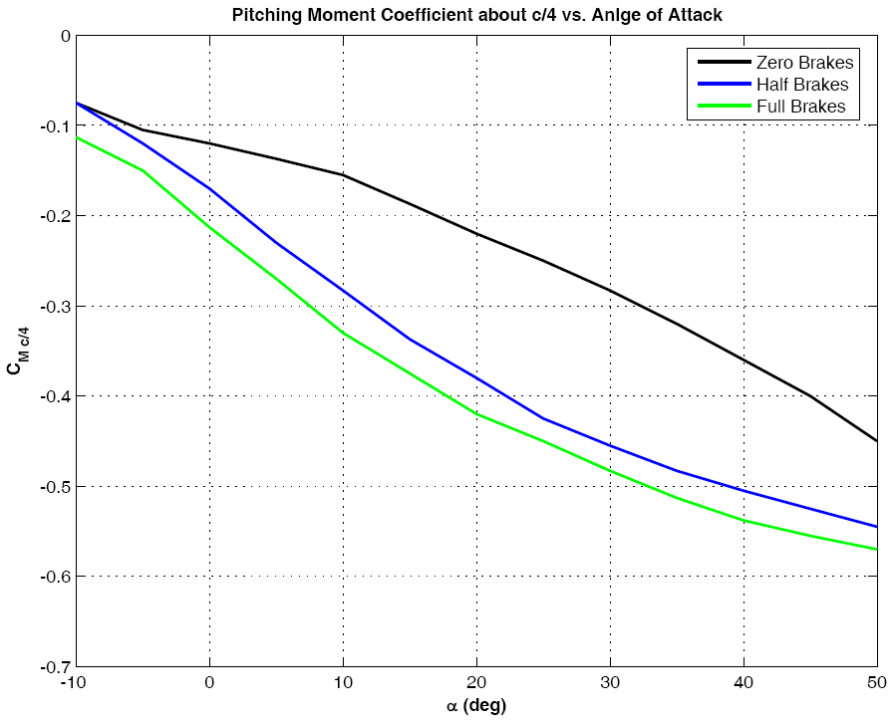

Figure 2.6 Pitching moment coefficient about the quarter chord variation vs. angle of attack and symmetric flap deflection based on data from Ref. (37) for R/b=1.0 and an aspect ratio of 2.0.

angles and is plotted in Figures 2.8, 2.9, and 2.10 for zero, half, and full symmetric brake deflections, respectively.

Figures 2.8–2.10 indicate a number of trends. We see in Figure 2.8 that rigging angles from 0–10 degrees yield trim angles-of-attack from 0–15 degrees, with increasing rigging angle decreasing the trim angle-of-attack. We see that for low rigging angles there may be multiple trim-angles of attack. Indeed, for φ=0 degrees we see three trim angles of attack at α =15, 32, and 35 degrees, with α = 15 and 35 degrees being stable trim points. In light of Figure 2.7 we see that the higher trim angle-of-attack has much smaller L/D and thus much poorer glide performance.

From Figures 2.9 and 2.10 we see for a given rigging angle that increasing the sym-

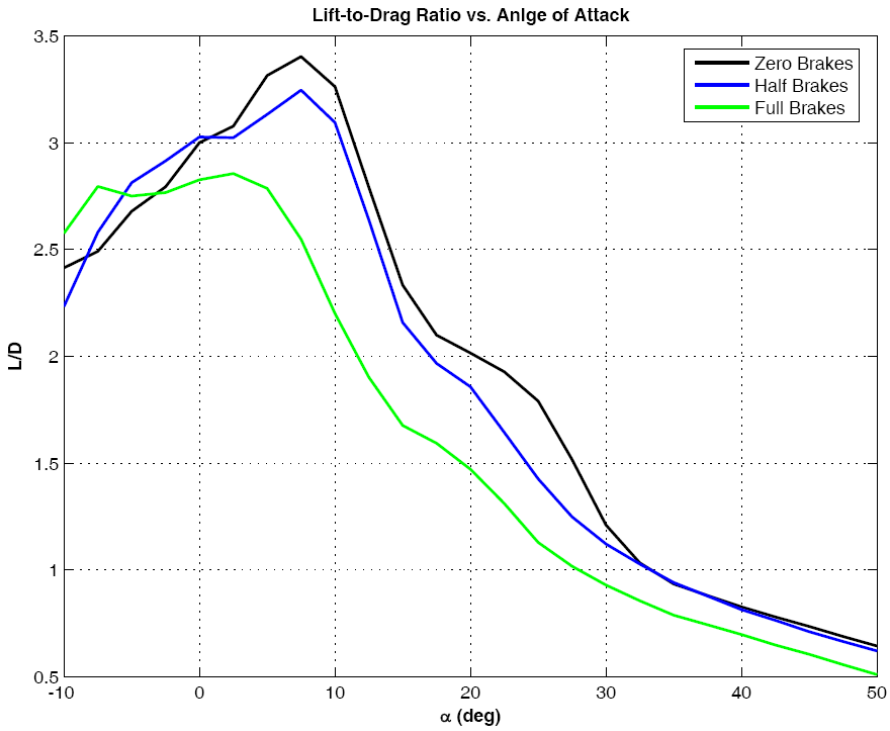

Figure 2.7 Lift-to-drag ratio variation vs. angle of attack and symmetric flap deflection based on data from Ref. (37) for R/b=1.0 and an aspect ratio of 2.0.

metric brake deflection from zero to half brakes has little effect on the trim angle of attack (and thus L/D) but increasing from half to full brakes significantly increases the trim angle of attack (decreasing L/D). Comparing Figure 2.10 to Figure 2.8 we also see that rigging angles that have only one stable trim angle-of-attack at zero brakes may have multiple trim angles-of-attack at higher brake settings.

Using the values of angle of attack corresponding to zero pitching moment from Figures 2.8 to 2.10, the trim values of L/D and the tangent coefficient C_T are plotted versus both symmetric brake deflection and rigging angle in Figures 2.11 and 2.12, respectively. In general we see that both the symmetric brake deflection and variation of the rigging angle can be used to modulate L/D. Symmetric brake deflection has the

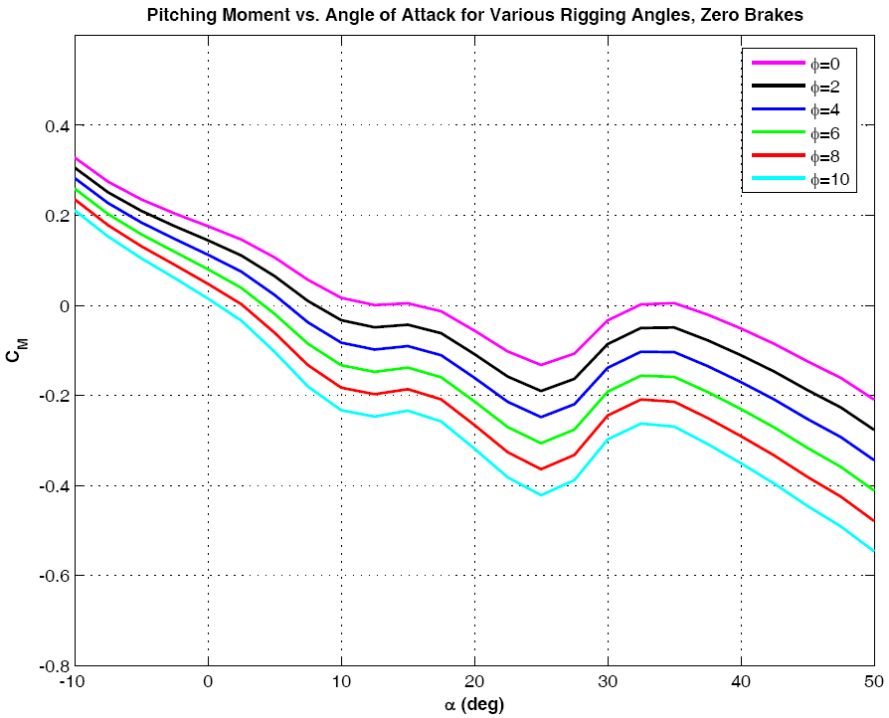

Figure 2.8 Pitching moment coefficient about the system c.g. vs. angle of attack for various choices of the rigging angle at zero symmetric brake deflection.

largest effect at larger brake deflections and lower rigging angles. Altering the rigging angle has the largest effect on L/D at smaller rigging angles both at high and low symmetric brake deflections.

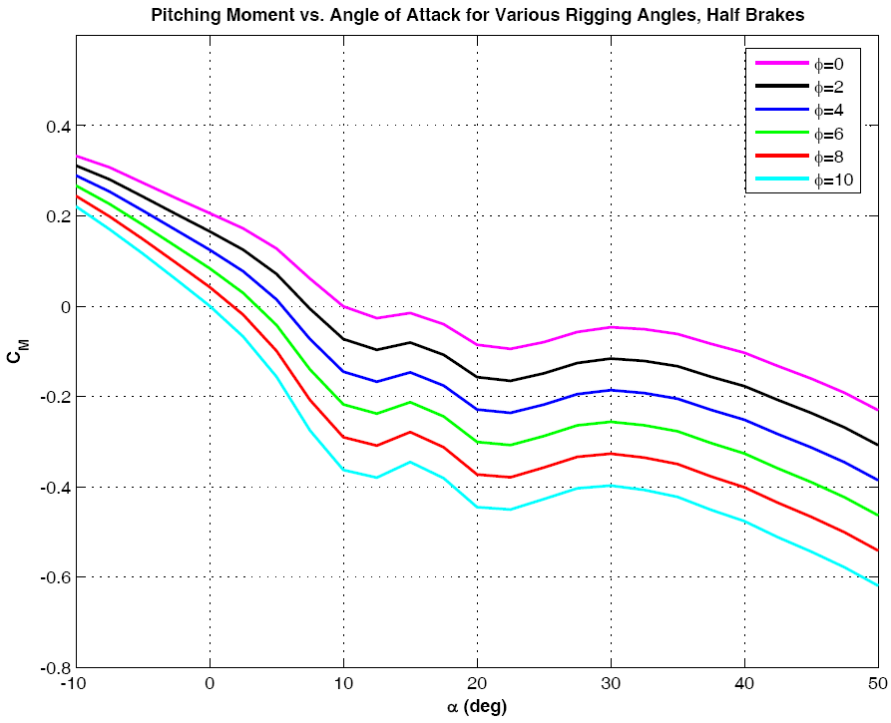

Figure 2.9 Pitching moment coefficient about the system c.g. vs. angle of attack for various choices of the rigging angle at half symmetric brake deflection.

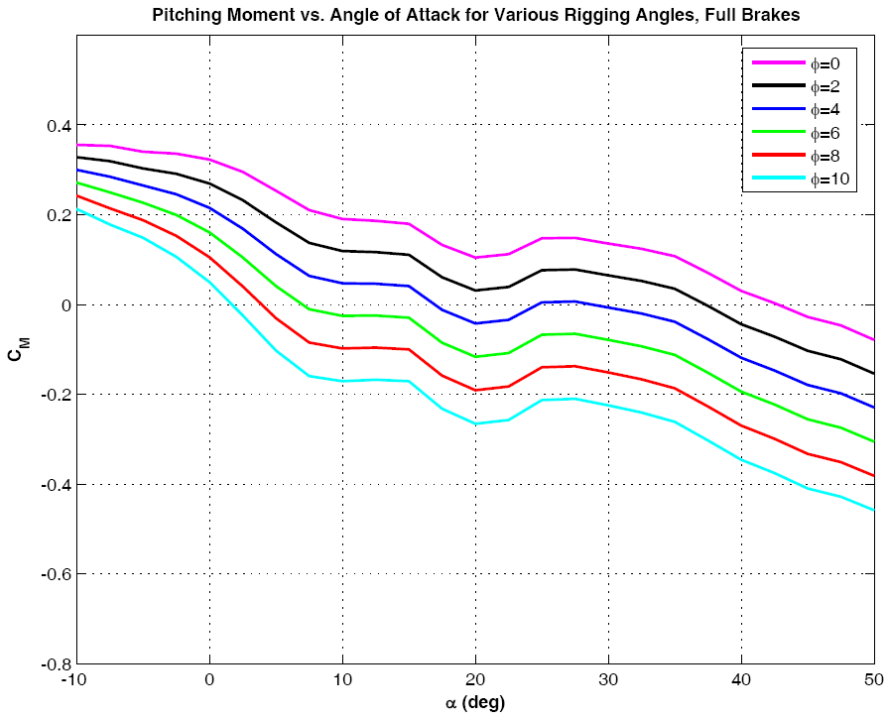

Figure 2.10 Pitching moment coefficient about the system c.g. vs. angle of attack for various choices of the rigging angle at full symmetric brake deflection.

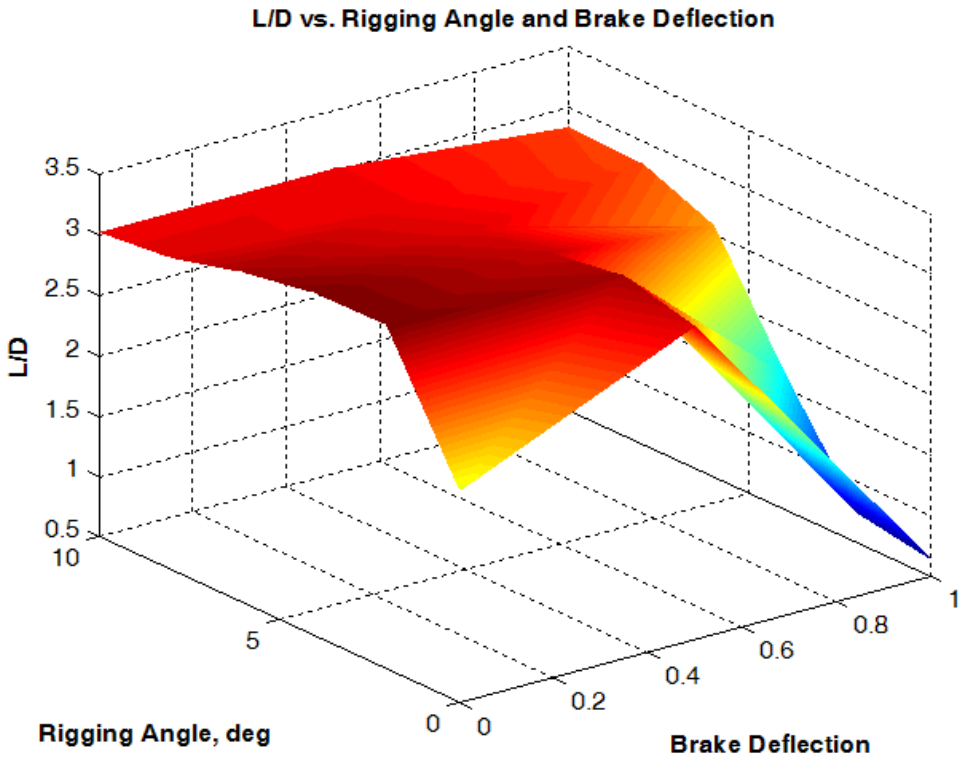

Figure 2.11 Trim lift-to-drag ratio vs. rigging angle and symmetric brake deflection.

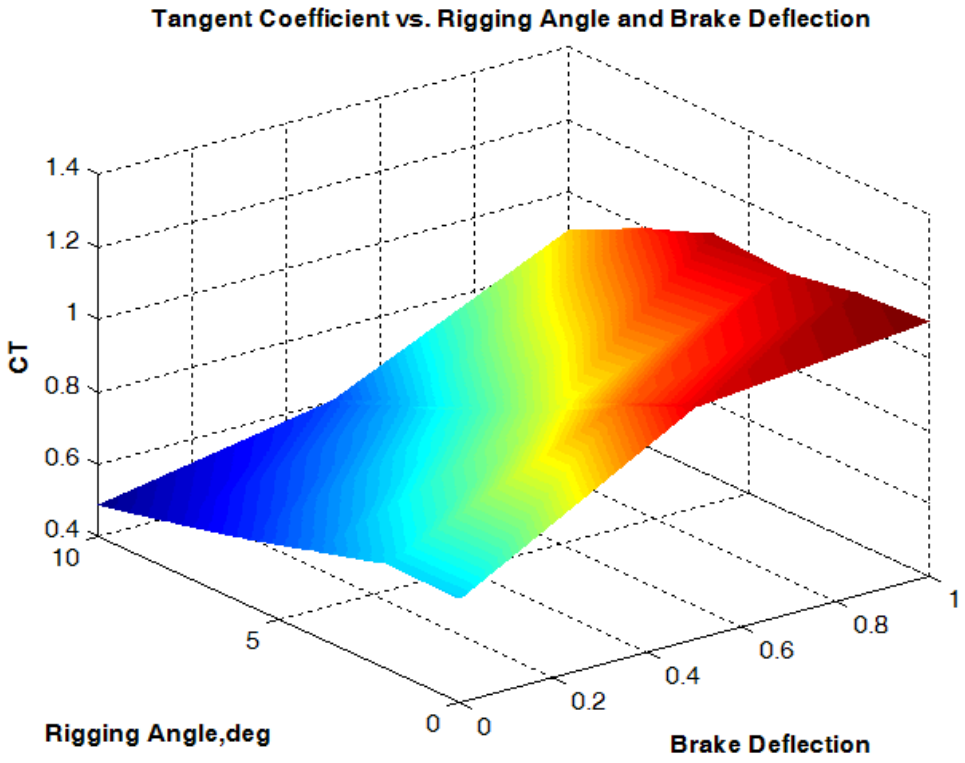

Figure 2.12 Tangent coefficient vs. rigging angle and symmetric brake deflection.

CHAPTER 3. PARAFOIL MODELING

In this chapter we describe a low-fidelity dynamic model to represent the macro-motion of a parafoil for use in guidance and control design. Transient motion due to changes in the angle of attack tends to be small in magnitude and damps out quickly relative to the time required to change flap settings due to inherent rate limitations in the winches used to affect control flap deflections. The model discussed herein applies to a wide range of parafoil canopies and payloads which encompass gross variations in canopy size, loading, aerodynamic performance and maximum turn rate. The model captures all of the key behaviors particular to parafoil motion while requiring as few parameters as possible. The key macro-motion behaviors of interest are that the glide-path angle and glide airspeed increase with turn rate. Apparent mass (see Section 2.3) terms do not explicitly show up in the model, we will show that the primary effects resulting from apparent mass important for guidance design are sufficiently captured. Finally, the model readily lends itself to reduction and simplification for trajectory planning purposes. We follow the modeling approach in Ref. (8) with some subtle differences to add the capability for longitudinal control.

3.1 Parafoil Equations of Motion

Consider the fore view of the traditional wind frame of a parafoil in turning flight, shown on the left side of Fig. 3.1. Here L is the sum of the aerodynamic forces perpendicular to the velocity vector, W is the weight force vector, ϕ is the true bank angle, and

σ can be thought of as the 'bank' angle of L. Note, the velocity and drag force vector components are omitted for clarity, and L as shown is the vertical projection of the true force onto the page.

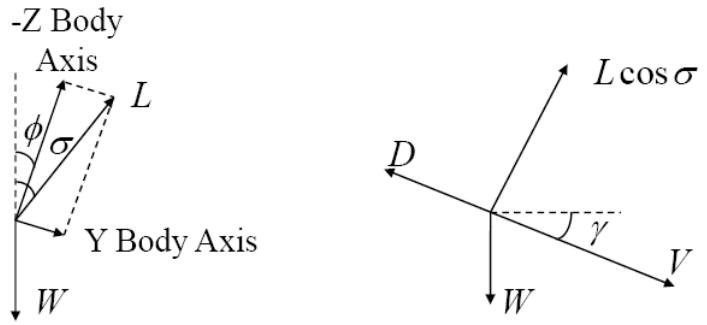

Figure 3.1 Force diagram for a parafoil in turning flight; fore view (left), side view (right).

The side view is shown on the right side of Fig. 3.1. Here V is the airspeed velocity vector, D is the vector sum the aerodynamic forces parallel to the airspeed vector, and γ is the flight path angle (negative as shown). The equations of motion for a parafoil over a flat, non-rotating Earth in a locally constant wind field can be written as

$$\dot{V} = -\frac{(D + W\sin\gamma)}{m} \tag{3.1}$$

$$\dot{\gamma} = \frac{(L\cos\sigma - W\cos\gamma)}{mV} \tag{3.2}$$

$$\dot{\psi} = \frac{L\sin\sigma}{mV\cos\gamma} \tag{3.3}$$

$$\dot{x} = V\cos\gamma\cos\psi + w_x \tag{3.4}$$

$$\dot{y} = V\cos\gamma\sin\psi + w_y \tag{3.5}$$

$$\dot{h} = V\sin\gamma \tag{3.6}$$

$$\dot{\sigma} = (\sigma_{com} - \sigma)/\tau_\sigma \tag{3.7}$$

$$\dot{\varepsilon} = (\varepsilon_{com} - \varepsilon)/\tau_\varepsilon \tag{3.8}$$

Here, ψ is the azimuth angle of the velocity vector, x is the downrange distance, y is the cross-range distance, h is the altitude above the ground, σ is the pseudo-bank angle, ε is a parameter that affects the lift and drag forces, W is the weight of the system (including the payload and the canopy), and w_x and w_y are the x and y components of the wind at the current position and altitude. The coordinate frame is chosen such that the origin coincides with the target at $h = 0$ with the x-axis in the ground plane *pointing into* the assumed wind at $h = 0$. The y-axis is rotated 90 degrees clockwise and also in the ground plane. The z-axis completes the right-handed coordinate frame so that $h = -z$. In addition, limits on $\dot{\psi}$, $\dot{\sigma}$, and $\dot{\varepsilon}$ are enforced. The lift and drag forces are modeled as

$$L = 0.5\rho V^2 S(C_{L_{\text{trim}}} + \delta C_L(\varepsilon)) \tag{3.9}$$

$$D = 0.5\rho V^2 S(C_{D_{\text{trim}}} + \delta C_D(\varepsilon)) \tag{3.10}$$

where ρ is the density of the air and is a function of altitude, S is the canopy area, and $C_L = C_{L_{trim}} + \delta C_L$ and $C_D = C_{D_{trim}} + \delta C_D$ are the lift and drag coefficients, respectively. Variations in ε represent the effects of altering the symmetric flap defection and/or the canopy rigging angle, and they produce increments δC_L and δC_D. It is assumed that for $\varepsilon = 0$, $\delta C_L = 0$ and $\delta C_D = 0$, thus C_L and C_D take on their trim values $C_{L_{trim}}$ and $C_{D_{trim}}$.

There are two control inputs for this model. The first is σ_{com} which is essentially a commanded turn rate and represents an asymmetric flap deflection. The second control input is ε_{com} which represents the commanded change in the longitudinal control, either a symmetric flap deflection or change of the rigging angle and is essentially a commanded glide-path angle. The variables τ_σ and τ_ε are the time constants of the control lag. These terms capture the time lag in the control due to actuator rate limitations and apparent mass effects.

3.2 Reduced-Order Model

For trajectory planning purposes a further simplified model is required to reduce computational burden and aid analysis. To simplify the model in the preceding section we begin by enforcing a quasi-equilibrium glide assumption and then change the independent variable from time to a function of altitude. These changes reduce the system order and simplify the trajectory planning problem. The final step in simplifying the model is converting to a wind-fixed coordinate frame to remove the time-varying drift due to the wind field.

3.2.1 Quasi-Equilibrium Glide Assumption

Consider an equilibrium gliding turn given by the condition $\dot{V} = \dot{\gamma} = \ddot{\psi} = 0$. Eqs. 3.1 and 3.2 imply

$$D = -W \sin\gamma \tag{3.11}$$

$$L\cos\sigma = W\cos\gamma \tag{3.12}$$

Dividing these two equations yields

$$\tan\gamma = -\frac{D}{L\cos\sigma} \tag{3.13}$$

In general, the equilibrium values of V and γ and the value of $\dot{\psi}$ are nonlinear functions of the state variables and canopy-specific performance parameters. For example, the nonlinear functional dependence may have the form

$$\gamma = \gamma(h, \sigma, L/D) \tag{3.14}$$

$$V = V(h, \sigma, W/S) \tag{3.15}$$

$$\dot{\psi} = \dot{\psi}(V, \sigma, L/D, \dot{\psi}_{max}) \tag{3.16}$$

where the dependence of γ on h comes from the dependence of the apparent mass forces on air density. The form of Eqs. 3.14–3.16 assumes planning will be done at a constant

value of $\varepsilon = 0$ (i.e. L/D will not be modulated when constructing reference trajectories). This is as far as we can go without making explicit assumptions about the aerodynamic and apparent mass forces. The following development will yield explicit forms for two of the above equations and simplify the form of the third.

It is convenient to specify the canopy performance in terms of the straight-line equilibrium values of the lift-to-drag ratio L/D and glide velocity V_0 at some specified altitude h_0, and the maximum turn rate $\dot{\psi}_{\max}$. Define the straight-line equilibrium glide path angle γ_G as

$$\tan\gamma_G = -\frac{D}{L} \tag{3.17}$$

Assuming that L/D remains constant with respect to σ (or implicitly with respect to the asymmetric flap deflection), from Eq. 3.13 we have

$$\tan\gamma = \frac{\tan\gamma_G}{\cos\sigma} \tag{3.18}$$

and from Eqs. 3.12 and 3.3 we have

$$\dot{\psi} = \frac{g}{V}\tan\sigma \tag{3.19}$$

A straight-line equilibrium glide will maintain constant dynamic pressure. This implies that the straight-line equilibrium glide velocity V_G at an altitude h is given by

$$V_G = \left(\frac{\rho(h_0)}{\rho(h)}V_0^2\right)^{1/2} \tag{3.20}$$

Observe that V_0 includes the effects of wing loading and V_G as defined in Eq. 3.20 includes the effects of altitude. This implies that the functional dependencies in Eq. 3.15 can be reduced to the non-turning velocity V_G and the bank angle σ, i.e.

$$V = V(V_G, \sigma) \tag{3.21}$$

If one further assumes that the lift and drag coefficients remain constant with respect to σ, we can show that

$$V = \sqrt{\frac{V_G^2\cos\gamma}{\cos\gamma_G\cos\sigma}} \tag{3.22}$$

3.2.2 Change of Independent Variable

Without loss of generality we shall define the final time t_f as the time when $h = 0$. We see from Eqs. 3.6, 3.14, and 3.15 that t_f is dependent on the time history of σ. Define

$$\tau = h(t_0) - h(t) \tag{3.23}$$

We have $\tau = 0$ at $t = 0$ and $\tau = h(t_0)$ at $t = t_f$. In all practical scenarios τ is strictly increasing (as the altitude is strictly decreasing). Consider τ as the new independent variable. We have

$$d\tau = -V \sin\gamma dt \tag{3.24}$$

This change of variable offers several benefits. First, it lowers the order of the system by one, decreasing the computational cost of evaluating trajectories. Second, all trajectories from a given initial condition–with any arbitrary control history $u(\tau)$–have the same final time τ_f. Third, the wind profile is often known or easily expressed as a function of altitude. This property will be used in the next section to simplify the trajectory planning task by 'factoring out' the influence of the wind. The key benefit of this variable change, though, is it converts the guidance task from a three-dimensional path planning problem to a two-dimensional problem.

To further simplify the trajectory planning problem, the turn acceleration dynamics are ignored. The new equations of motion incorporating this assumption and the quasi-equilibrium glide assumption reduce to

$$\dot{x} = -\left(\frac{\cos\psi}{\tan\gamma} + \frac{w_x(\tau)}{V\sin\gamma}\right) \tag{3.25}$$

$$\dot{y} = -\left(\frac{\sin\psi}{\tan\gamma} + \frac{w_y(\tau)}{V\sin\gamma}\right) \tag{3.26}$$

$$\dot{\psi} = -\frac{g\tan\tilde{u}}{V^2\sin\gamma} \tag{3.27}$$

where $\tilde{u}$ is the commanded pseudo bank angle σ (control input).

3.2.3 Wind-Fixed Coordinate Frame

In the sequel we shall find it convenient to remove the τ-varying drift induced by the wind profile. Without loss of generality we shall fix the origin of the inertial coordinate frame at the targeted landing site with the x-axis aligned with the desired final heading. Consider a second coordinate frame that moves with the air mass and has the same orientation as the inertial frame. The origin of this 'wind-fixed' frame is located such that it exactly coincides with the origin of the inertial frame at $\tau = \tau_f$. The exact position in this coordinate frame is given by

$$x_w(\tau) = x(\tau) - \int_{\tau}^{\tau_f} \kappa(\tau) w_x(\tau) d\tau \tag{3.28}$$

$$y_w(\tau) = y(\tau) - \int_{\tau}^{\tau_f} \kappa(\tau) w_y(\tau) d\tau \tag{3.29}$$

where $\kappa = (V(\tau)\sin\gamma(\tau))^{-1}$. Thus determining the exact position in this coordinate frame requires knowledge of the control history for the remaining portion of the trajectory (through the dependence of V and γ on $\dot{\psi}$). If we replace (V, γ) with (V_G, γ_G), the position in this wind-fixed frame can be approximated by

$$x_w(\tau) = x(\tau) - \int_{\tau}^{\tau_f} \kappa_G(\tau) w_x(\tau) d\tau \tag{3.30}$$

$$y_w(\tau) = y(\tau) - \int_{\tau}^{\tau_f} \kappa_G(\tau) w_y(\tau) d\tau \tag{3.31}$$

where $\kappa_G = (V_G(\tau)\sin\gamma_G(\tau))^{-1}$. The velocity and flight path angle magnitudes increase in a turn, thus choosing the equilibrium glide values of V and γ will tend to overestimate the total drift due to wind. However, this substitution provides a reasonable approximation to the position in the wind-fixed coordinate frame and significantly reduces computational cost.

Working in the wind-fixed frame further simplifies the motion planning problem as

the equations of motion (3.25-3.27) simplify to:

$$\dot{x}_w = \tilde{a}\cos\psi \tag{3.32}$$

$$\dot{y}_w = \tilde{a}\sin\psi \tag{3.33}$$

$$\dot{\psi} = \tilde{a}u \tag{3.34}$$

where $\tilde{a} = -(\tan\gamma)^{-1}$, $u = 1/(r\cos\gamma)$, and the turning radius r is given by $(V^2\cos\gamma)/(g\tan\sigma)$. In the sequel we shall omit the subscript w unless the context is not clear.

3.3 Wind Field Modeling

In the most general case the wind velocity vector has components along all three axes which vary in space and time:

$$\mathbf{W} = \mathbf{W}(x, y, h, t) = \begin{bmatrix} w_x \\ w_y \\ w_z \end{bmatrix} \tag{3.35}$$

In the present work we make the following assumptions about the wind profile:

1. The z-axis component w_z is zero.

2. The horizontal wind can be written as the sum of a (relatively) low frequency mean wind component and a (relatively) high frequency turbulence component.

3. The mean wind components are functions of altitude and time only.

Often times an a priori estimate of the wind profile is available and given as a function of altitude. The mean wind profile can then be written as the sum of the altitude-varying a priori wind profile and a time-varying perturbation

$$\mathbf{W} = \mathbf{W}_{ap}(h) + \tilde{\mathbf{W}}(t) \tag{3.36}$$

In light of the independent variable change defined in Eq. 3.23 we can write

$$\mathbf{W} = \begin{bmatrix} w_x \\ w_y \end{bmatrix} = \mathbf{W}_{ap}(\tau) + \tilde{\mathbf{W}}(\tau) \tag{3.37}$$

which justifies the τ dependence of w_x and w_y in Eqs. 3.32–3.34.

There are many potential sources for the a priori wind profile such as radar observations, RUC forecast data (38), and balloon soundings or drop-sondes (39). In the event that no a priori wind profile is available $\mathbf{W}_{ap}$ can be set to zero and the entire mean wind field can be encompassed in the unknown wind field perturbation $\tilde{\mathbf{W}}(\tau)$.

CHAPTER 4. FIXED-TIME TRAJECTORY PLANNING

In the previous chapter it was shown that the parafoil trajectory planning problem could be cast as a fixed-time two-point boundary value problem. The planning problem consists of finding a kinematically feasible trajectory from an initial position and orientation $(x(0), y(0), \psi(0))$ to a final position and orientation $(x(\tau_f), y(\tau_f), \psi(\tau_f))$ (which by the choice of coordinate frame discussed in the previous section can be written $(0, 0, 0)$) where τ_f is the specified final time. That is, in the wind-fixed frame, the required terminal constraints are always

$$x(\tau_f) = 0 \tag{4.1}$$

$$y(\tau_f) = 0 \tag{4.2}$$

$$\psi(\tau_f) = 0 \tag{4.3}$$

This boundary value problem is readily solved within the framework of optimal control, provided a meaningful performance index is defined. In this section we begin by deriving the conditions for a generalized trajectory optimization problem which leads to insight into the nature of the optimal trajectories. We then proceed to derive minimum-time trajectories which leads to a necessary condition for a kinematically feasible fixed-final time trajectory to exist and the definition of a parameter, the altitude margin, that can be used in trajectory planning logic. Next we present two methods for generating fixed-time trajectories, each particularly suited to certain classes of initial conditions and values of the altitude margin.

4.1 Optimal Control Problem

In this section we consider a generalized trajectory optimization problem. Much insight into the nature of the optimal control solutions can be obtained from the costate solutions to this problem. Recall that the optimal control problem is to find $u(t)$ to minimize the performance index

$$J = \int_0^{\tau_f} L(\mathbf{x}, u) d\tau \tag{4.4}$$

subject to the constraints

$$\dot{\mathbf{x}} = \mathbf{f}(\mathbf{x}, u) \tag{4.5}$$

$$\mathbf{x}(\tau_0) \text{ given} \tag{4.6}$$

$$\Psi(\mathbf{x}(\tau_f)) = 0 \tag{4.7}$$

$$u \in U = [a, b] \tag{4.8}$$

where the dynamics in Eq. 4.5 are given by the kinematic model (3.32–3.34) with the 'velocity' $\tilde{a}$ normalized to one, the state vector $\mathbf{x} = \begin{bmatrix} x & y & \psi \end{bmatrix}^T$ and a and b are real scalars such that $a < 0 < b$. The terminal constraints (4.7) are defined in Eqs. 4.1–4.3. We assume that the function L in Eq. 4.4 is continuous in its arguments and not an explicit function of τ or the state $\mathbf{x}$. The Hamiltonian for this system is given by

$$H = p_x \cos\psi + p_y \sin\psi + p_\psi u + L(u) \tag{4.9}$$

where $\mathbf{p} = \begin{bmatrix} p_x & p_y & p_\psi \end{bmatrix}^T$ is the adjoint or costate vector. The costate equations are

$$\dot{p_x} = -\frac{\partial H}{\partial x} = 0 \tag{4.10}$$

$$\dot{p_y} = -\frac{\partial H}{\partial y} = 0 \tag{4.11}$$

$$\dot{p_\psi} = -\frac{\partial H}{\partial \psi} = p_x \sin\psi - p_y \cos\psi \tag{4.12}$$

Substituting Eqs. 3.32 and 3.33 into Eq. 4.12 we get

$$\dot{p_\psi} = p_x\dot{y} - p_y\dot{x} \tag{4.13}$$

Observe from Eqs. 4.10 and 4.11 that p_x and p_y are constant. With this observation, integrating Eq. 4.12 with respect to τ yields

$$p_\psi = p_x y - p_y x - \tilde{c} \tag{4.14}$$

where $\tilde{c}$ is a constant of integration. We can also write

$$p_\psi = c_1 x + c_2 y + c_3 \tag{4.15}$$

where $c_1 = -p_y$, $c_2 = p_x$, and $c_3 = \tilde{c}$. Observe that $p_\psi = 0$ defines a line in the x–y plane and contours of constant p_ψ are lines parallel to this line. In the sequel we shall refer to the line $p_\psi = 0$ as the switching line for reasons that will become apparent.

Consider the variable change given by

$$\begin{aligned} p_x &= b_1 \cos b_2 \\ p_y &= -b_1 \sin b_2 \end{aligned} \tag{4.16}$$

for constants b_1 and b_2. Note, b_1 and b_2 can always be found such that this transformation holds for arbitrary p_x and p_y. The reverse transformation is given by

$$\begin{aligned} b_1 &= \left(p_x^2 + p_y^2\right)^{1/2} \\ b_2 &= \tan^{-1}\left(-\frac{p_y}{p_x}\right) \end{aligned} \tag{4.17}$$

Substituting Eq. 4.16 into Eq. 4.9, the Hamiltonian can now be written

$$H = b_1 \cos(b_2 + \psi) + p_\psi u + L(u). \tag{4.18}$$

Finally, we shall also find it convenient to rewrite the third costate equation using Eq. 4.16 as

$$\dot{p}_\psi = b_1 \sin(b_2 + \psi) \tag{4.19}$$

The Minimum Principle of Pontryagin states that along an optimal trajectory $(\mathbf{x}^*, \mathbf{p}^*)$ the optimal value of the control, u^* minimizes the Hamiltonian over the set of all possible inputs at each moment in time, i.e.

$$H(\mathbf{x}^*, \mathbf{p}^*, u^*, \tau) = \min_{u \in U, \tau \in [\tau_0, \tau_f]} H(\mathbf{x}^*, \mathbf{p}^*, u, \tau) \tag{4.20}$$

and that $\mathbf{p} \neq 0$ for $\tau \in [\tau_0, \tau_f]$.

4.2 Minimum-Time Trajectories

For minimum-time trajectories we have

$$L(u) = 1 \tag{4.21}$$

The minimizing control u^* satisfying Eq. 4.20 is given by

$$p_\psi u^* \leq p_\psi u \qquad \forall \quad u \in U \tag{4.22}$$

If the minimizing control lies at one of the limits then minimizing Eq. 4.18 implies

$$p_\psi u < 0 \tag{4.23}$$

If the minimizing control lies within the admissible region we have

$$\frac{\partial H}{\partial u} = p_\psi = 0 \tag{4.24}$$

Since $p_\psi \equiv 0$ we must have $\dot{p}_\psi \equiv 0$ which in light of Eq. 4.19 admits two possibilities. If $b_1 = 0$ then we have $p_x = p_y = p_\psi = 0$ which is ruled out by the Minimum Principle. If $b_1 \neq 0$ either $\psi = -b_1$ or $\psi = -b_1 + \pi$ (both modulo 2π). Hence $\dot{p}_\psi = 0 \Rightarrow \dot{\psi} = 0$ so that $u = 0$. Summarizing we have

$$u = \begin{cases} a & p_\psi > 0 \\ 0 & p_\psi = 0 \\ b & p_\psi < 0 \end{cases} \tag{4.25}$$

The preceding discussion implies a number of properties for the minimum-time trajectories:

1. All optimal trajectories consist of maximum rate turns and straight lines.

2. All straight line segments are parallel to one fixed direction.

3. The line $p_\psi = 0$ divides the plane such that the control is strictly positive on one side and strictly negative on the other side.

4. All straight line segments of the trajectory and all changes in turning direction occur on a single line in the plane.

The optimal minimum-time trajectory was shown by Dubins in Ref. (16) and later by Boissonnat et. al in Ref. (17) to consist of no more than three constant-control segments. Each segment is either a maximum-rate (minimum-radius) turn or a straight line ($u = 0$). Furthermore, the minimum-time trajectories are generated using one of six possible control sequences: RSR, RSL, LSR, LSL, LRL, or RLR where R corresponds to a maximum right-hand turn, L corresponds to a maximum left-hand turn, and S corresponds to a straight line. These trajectories are referred to as Dubins curves or Dubins paths. Examples of the RSL, LSL and LRL Dubins paths are shown in Fig. 4.1. The circles in this figure correspond to the minimum turn radius.

4.3 A Necessary Condition

Let the cost associated with each admissible Dubins path be denoted τ_{RSR}, τ_{LSL}, etc. and define

$$\tau_{\min} = \min\left\{\tau_{\mathrm{RSR}}, \tau_{\mathrm{LSL}}, \tau_{\mathrm{RSL}}, \tau_{\mathrm{LSR}}, \tau_{\mathrm{RLR}}, \tau_{\mathrm{LRL}}\right\} \tag{4.26}$$

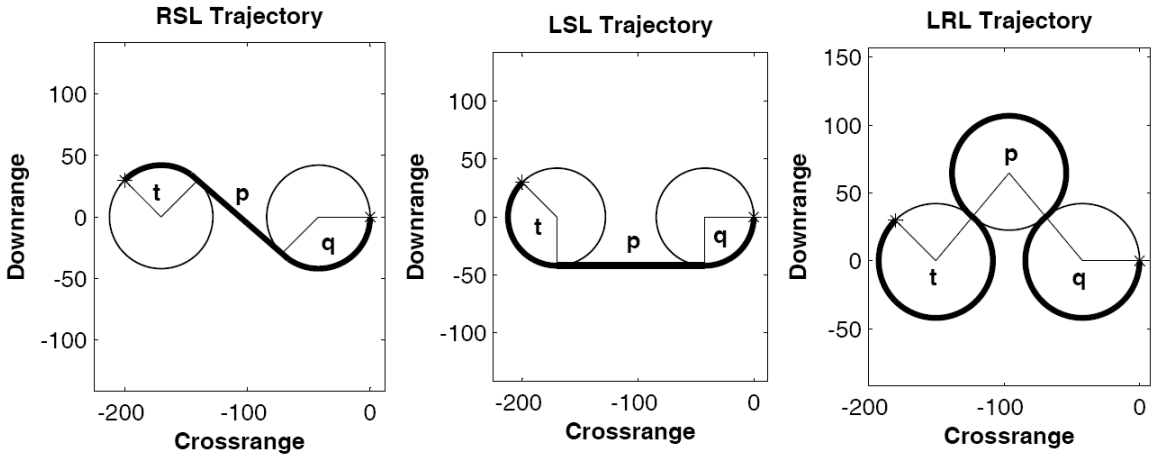

Figure 4.1 Examples of Dubins paths: RSL (left), LSL (center), LRL (right). Note: the LRL path is not optimal in this example. The quantities t and q are the outer turn angles and the quantity p is the length of the straight line segment for type CSC paths and the middle turn angle for type CCC paths.

Clearly, for a trajectory satisfying the specified initial conditions, terminal conditions, and the specified final time τ_f to exist we require that

$$\tau_{\min} \leq \tau_f \tag{4.27}$$

Now let τ_{360} equal the cost of completing one full 360° turn at maximum turn rate. We now define the altitude margin as

$$\eta = \frac{\tau_f - \tau_{\min}}{\tau_{360}} \tag{4.28}$$

so that the necessary condition (4.27) can also be written as

$$\eta \geq 0 \tag{4.29}$$

Considering the definition of τ in Eq. 3.23, one can see that the altitude margin is a normalized measure of the altitude in excess of the minimum altitude required for the constrained system to reach the specified terminal conditions from the specified initial

conditions. The altitude margin provides a quantitative measure of the difficulty in attaining the final conditions in the specified time interval. An altitude margin of zero indicates the initial altitude is exactly the required altitude to reach the final condition. A negative value of the altitude margin indicates the initial altitude is not sufficient to reach the final conditions for any choice of the control history $u(\tau)$. A positive altitude margin indicates the amount of excess energy (altitude) is available for maneuvering and the degree of wind uncertainty that can be overcome.

4.4 Minimum Control-Energy Paths

Consider now the case where the final time is *fixed* at τ_f and the performance index is the control energy(24)

$$L(u) = \frac{1}{2}u^2 \tag{4.30}$$

The minimizing control u^* satisfying Eq. 4.18 is given by

$$p_\psi u^* + \frac{1}{2}u^{*2} \leq p_\psi u + \frac{1}{2}u^2 \qquad \forall \quad u \in U \tag{4.31}$$

As before, if the minimizing control lies at one of the limits then minimizing Eq. 4.18 implies

$$p_\psi u < 0 \tag{4.32}$$

If the minimizing control lies in the interior of the admissible control set, we have

$$\frac{\partial H}{\partial u} = p_\psi + u = 0 \tag{4.33}$$

Summarizing we have

$$u = \begin{cases} a & -p_\psi < a \\ -p_\psi & -p_\psi \in [a, b] \\ b & -p_\psi > b \end{cases} \tag{4.34}$$

Using Eqs. 4.15 and 4.33, the guidance law in the absence of control saturation can be written

$$u = -(c_1 x + c_2 y + c_3) \tag{4.35}$$

We now illustrate some properties of the optimal trajectories. Observe from Eq. 4.35 that $u = 0$ defines the parametric line

$$c_1 x + c_2 y + c_3 = 0 \tag{4.36}$$

which is the same as the switching line defined in Eq. 4.15.

Property 1. The control u can be written as

$$u = d\sqrt{c_1^2 + c_2^2} \tag{4.37}$$

where d is the signed perpendicular distance of the point (x, y) from the line given by Eq. 4.36.

Proof: The signed perpendicular distance d of a point (x, y) from the general parametric line $ax + by + c = 0$ can be shown to be $(ax + by + c)/\sqrt{a^2 + b^2}$. Substituting $a = c_1$, $b = c_2$, and $c = c_3$ completes the proof.

Property 2. The line (4.36) divides the x–y plane so that the control u is strictly positive on one side of the line and strictly negative on the other. The proof follows directly from Property 1, observing that c_1 and c_2 are constant.

Property 3. In general, the trajectory resulting from the guidance law (4.35) contains no straight line.

Proof: A straight-line trajectory requires $u \equiv 0$. Observe that u remains zero only when the trajectory lies along the line (4.36). If any portion of the trajectory lies along this line the entire trajectory must lie along the line as $u = 0 \Rightarrow \dot{\psi} = 0$. Only the trivial case where the entire trajectory lies on the negative x-axis contains a straight line. This

is a pathological case where the initial condition lies exactly on the negative x-axis with an initial heading of zero and the specified final time is such that the system just reaches the target.

Property 4. In the absence of turn rate limit, the trajectories contain no circular arcs.

Proof: Suppose the trajectory contains a circular arc. This means that u is a nonzero constant and $\dot{u} = 0$ and for some finite time interval. By Eq. 4.35, $\dot{u} = 0$ for the unsaturated u implies that

$$c_1\dot{x} = -c_2\dot{y} \tag{4.38}$$

which by Eqs. 3.32 and 3.33, in turn, results in that

$$-\frac{c_1}{c_2} = \tan\psi = \text{constant} \tag{4.39}$$

However, the above condition of constant ψ contradicts the requirement of nonzero constant $u = \dot{\psi}$. Thus the trajectories cannot contain circular arcs in the absence of turn rate limit.

As discussed in Section 4.2, the Dubins paths consist of a series of circular arcs and straight-line segments. Properties 3 and 4 above indicate that the minimum control-energy trajectories in general will not coincide with Dubins paths.

4.5 Solution and Sample Minimum Control-Energy Trajectories

The solution to the above fixed-time minimum control-energy problem is ensured whenever the problem admits feasible solutions. More specifically, if any feasible trajectory exists that satisfies the given initial condition and terminal constraints at τ_f with an admissible control $u(\tau) \in U$ for $0 \leq \tau \leq \tau_f$, this optimal control problem is guaranteed

to have a solution. This conclusion directly follows from Corollary 2 of Chapter 4 in Ref. (40) because the system equations in Eq. (4.5) are affine in the control u, and for any fixed $\mathbf{x}$ the set $\{L(\mathbf{x}, u)\ \mathbf{f}(\mathbf{x}, u)\}$, $\forall u \in U$, is strictly convex in R^4 (where $U = [a,\ b]$ is compact and convex). This property is very reassuring for our purpose of trajectory planning.

To determine the solution, the required values of c_1, c_2, and c_3 in Eq. 4.35 need to be found numerically to satisfy the terminal condition in Eqs. 4.1–4.3. The convergence behavior is dependent on both the initial offset of the system from the target and the altitude margin. For sufficient altitude margin, the solution is found easily with a wide range of initial guesses. For large offsets, small changes in c_1, c_2, and c_3 lead to large changes in the final position. Hence convergence tends to be become more sensitive with respect to initial guesses as the initial offset becomes very large ($> 10^3$ in consistent units). As the altitude margin decreases, the convergence behavior also becomes increasingly dependent on the initial guess of the solution. In general, if the normalized altitude margin is less than about one it becomes considerably more difficult to converge. This is because in such cases the trajectory gets close to the minimizing Dubins path but the minimum control-energy trajectories cannot converge directly to the Dubins path (cf. Property 4 in the preceding section).

A number of example trajectories are shown in Fig. 4.2. Each trajectory has the same starting position and the initial altitude is such that the initial normalized altitude margin is three. But the initial heading is different. The figure shows the general shape of the trajectories computed using the presented optimal control approach (recall that the targeted landing site is at the origin).

A number of example trajectories with the same starting configuration are shown in Fig. 4.3. For these trajectories, the altitude margin is varied from 0.2 to 2.2 in increments of 0.4. A feature worth noting in Fig. 4.3 is that as the altitude margin decreases the trajectory begins to approach to the Dubins path, indicated by the dotted line.

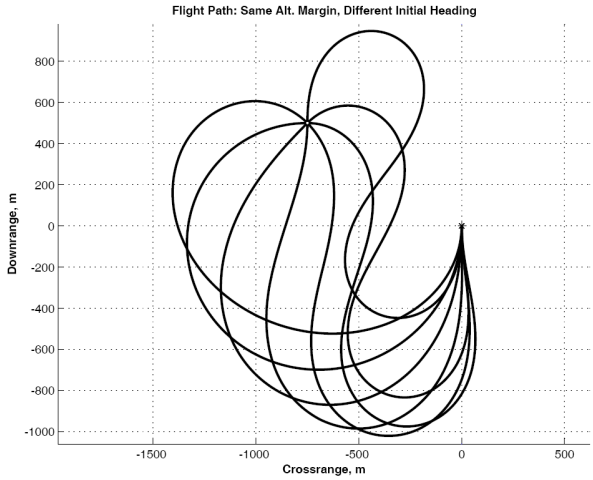

Figure 4.2 Minimum control-energy trajectories for an initial normalized altitude margin η=3, varying the initial heading. The initial position is the same for each case.

Another example trajectory is shown in Fig. 4.4. This is a pathological example in which the initial position is directly above the desired target with the initial heading opposite the desired final heading. The initial normalized altitude margin is relatively large at 10. Observe the symmetry of the trajectory about the downrange axis, which is due to the initial condition. For this case, the value of c_2 in the guidance law is zero. This example illustrates that the trajectory generation method is robust to cases with obscure initial conditions and a large initial altitude margin.

4.6 Modified Dubins Paths

The minimum-time Dubins paths in Section 4.2 cannot be directly applied to our problem because it is a *fixed-time* problem. However, it is possible to modify the Dubins path calculation to generate fixed-time reference trajectories for cases where the altitude margin is greater than or equal to zero. In this case the trajectory is no longer optimal in any sense, but we will show that a simple closed-form expression can be used to generate

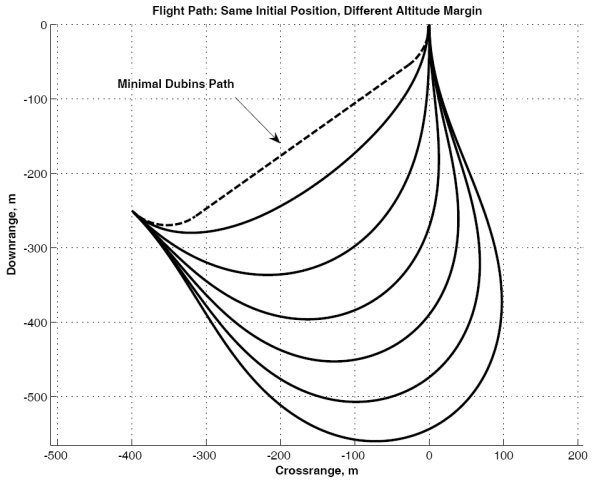

Figure 4.3 Minimum control-energy trajectories for the same initial configuration, varying the initial normalized altitude margin η from 0.2 to 2.2 in increments of 0.4. The dotted line corresponds to the minimal Dubins path.

the modified Dubins path. The idea is to increase the turn radius from the minimum until the altitude margin (using the new turn radius) of the resulting path is equal to zero, in other words the cost of the path is increased until the cost equals the specified terminal time. A path generated in this fashion satisfies the initial and final conditions imposed on the trajectory, as well as the fixed final time (altitude margin).

The turning radius is defined by

$$r = \frac{V^2 \cos\gamma}{g \tan\sigma} \tag{4.40}$$

where γ is given by Eq. 3.14 or 3.18 and V is given by Eq. 3.15 or 3.22 are also functions of σ. Given an initial position and orientation (x_0, y_0, ψ_0), a final position and orientation (x_f, y_f, ψ_f) and turning radius r (or, implicitly, σ) one can find an analytical expression for the quantities t, p, and q defined in Fig. 4.1 as well as the cost for each of the admissible Dubins paths. Fig. 4.5 illustrates the geometry of the problem and defines some key parameters that will be used in the following development.

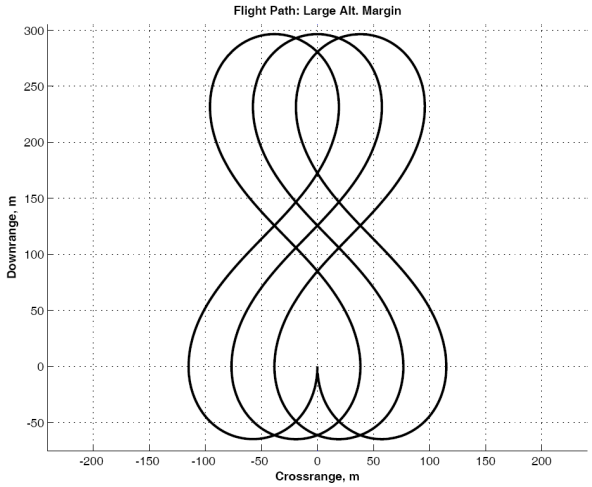

Figure 4.4 This is an example trajectory with the initial position at the intended target and the initial heading opposite the required final heading. The normalized altitude margin for this example is 10. Note the symmetry of the trajectory about the downrange axis.

From Fig. 4.5 we see that

$$\Gamma = \tan^{-1}\left(\frac{y_f - y_0}{x_f - x_0}\right) \tag{4.41}$$

$$\lambda = \Gamma - \psi_0 \quad \{\text{mod } 2\pi\} \tag{4.42}$$

$$\mu = \Gamma - \psi_f \quad \{\text{mod } 2\pi\} \tag{4.43}$$

$$d = \left((x_f - x_0)^2 + (y_f - y_0)^2\right)^{1/2} \tag{4.44}$$

Recall that Dubins path consists of three segments of elementary motion: turning right along an arc with radius r (denoted by R), turning left along an arc of the same radius r (L), and motion in a straight line (S). We will limit the sequence of motion primitives to the 6 sequences corresponding to the minimum-time Dubins paths described in Section 4.2: RSR, RSL, LSR, LSL, LRL, or RLR. Suppose the system is at the point (x_1, y_1, ψ_1) and then performs a right turn through an angle ν. Following the approach in (42), define an operator R_ν that transforms the point (x_1, y_1, ψ_1) to the point at the

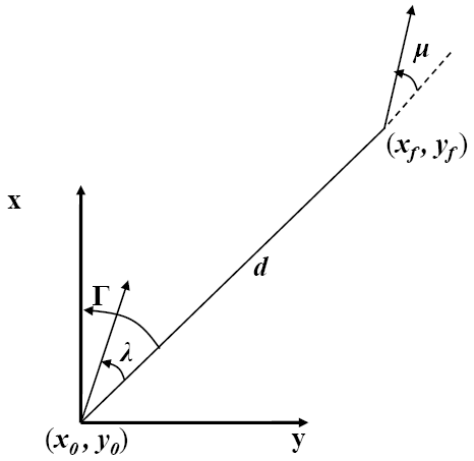

Figure 4.5 Geometry and parameters used to calculate members of the Dubins set.

end of the turn, denoted (x_2, y_2, ψ_2). Similar operators L_ν and S_ν can be defined for left turns and straight-line segments, respectively. These operators are given by

$$R_\nu(x_1, y_1, \psi_1) = \begin{pmatrix} x_1 + r\sin(\psi_1 + \nu) - r\sin\psi_1 \\ y_1 - r\cos(\psi_1 + \nu) + r\cos\psi_1 \\ \psi_1 + \nu \end{pmatrix} \tag{4.45}$$

$$L_\nu(x_1, y_1, \psi_1) = \begin{pmatrix} x_1 - r\sin(\psi_1 - \nu) + r\sin\psi_1 \\ y_1 + r\cos(\psi_1 - \nu) - r\cos\psi_1 \\ \psi_1 - \nu \end{pmatrix} \tag{4.46}$$

$$S_\nu(x_1, y_1, \psi_1) = \begin{pmatrix} x_1 + \nu\cos\psi_1 \\ y_1 + \nu\sin\psi_1 \\ \psi_1 \end{pmatrix} \tag{4.47}$$

Consider a new coordinate frame found by rotating the coordinate frame in Fig. 4.5 clockwise by an angle Γ with the origin located at the initial point (x_0, y_0). In this new frame, the initial position and orientation are $(0, 0, \lambda)$ and the final position and orientation are $(d, 0, \mu)$. By composition of the operators (4.45–4.47) one can find analytical

expressions for the turn angles or line lengths t, p, and q defined in Fig. 4.1. For example, the result of an RSL turn can be found by the composition $L_q(S_p(R_t(0,0,\lambda)))$. Using the final condition $(d,0,\mu)$ leads to the scalar system of equations

$$\begin{aligned} d &= p\cos(\lambda+t) + 2r\sin(\lambda+t) - r\sin\lambda - r\sin\mu \\ 0 &= p\sin(\lambda+t) - 2r\cos(\lambda+t) + r\cos\lambda + r\cos\mu \\ \mu &= \lambda + t - q \end{aligned} \tag{4.48}$$

which can be solved to yield the corresponding lengths of the trajectory segments:

$$\begin{aligned} t_{\mathrm{RSL}} &= -\lambda - \tan^{-1}\left(\frac{2r}{p}\right) + \tan^{-1}\left(\frac{-r\cos\lambda - r\cos\mu}{d + r\sin\lambda + r\sin\mu}\right) \\ q_{\mathrm{RSL}} &= -\mu - \tan^{-1}\left(\frac{2r}{p}\right) + \tan^{-1}\left(\frac{-r\cos\lambda - r\cos\mu}{d + r\sin\lambda + r\sin\mu}\right) \\ p_{\mathrm{RSL}} &= \left(-2r^2 + d^2 + 2r^2\cos(\lambda-\mu) + 2rd(\sin\mu + \sin\lambda)\right)^{1/2} \end{aligned} \tag{4.49}$$

The cost (which is "time", or the altitude drop for the parafoil) of the RSL path can be shown to be

$$\tau_{\mathrm{RSL}} = r\tan\gamma(\lambda - \mu + 2t_{RSL}) + p_{RSL}\tan\gamma_G \tag{4.50}$$

In a similar fashion we can find t, p, and q and the cost for the remaining Dubins paths. For LSR we have

$$\begin{aligned} t_{\mathrm{LSR}} &= \lambda + tan^{-1}\left(\frac{2p}{r}\right) - \tan^{-1}\left(\frac{r\cos\lambda + r\cos\mu}{d - r\sin\lambda - r\sin\mu}\right) \\ q_{\mathrm{LSR}} &= \mu + tan^{-1}\left(\frac{2p}{r}\right) - \tan^{-1}\left(\frac{r\cos\lambda + r\cos\mu}{d - r\sin\lambda - r\sin\mu}\right) \\ p_{\mathrm{LSR}} &= \left(-2r^2 + d^2 + 2r^2\cos(\lambda-\mu) - 2rd(\sin\mu + \sin\lambda)\right)^{1/2} \end{aligned} \tag{4.51}$$

$$\tau_{\mathrm{LSR}} = r\tan\gamma(\mu - \lambda + 2t) + p\tan\gamma_G \tag{4.52}$$

For RSR we have

$$\begin{aligned} t_{\mathrm{RSR}} &= -\lambda - \tan^{-1}\left(\frac{r\cos\mu - r\cos\lambda}{d + r\sin\lambda - r\sin\mu}\right) \\ q_{\mathrm{RSR}} &= \mu\{\bmod 2\pi\} - \tan^{-1}\left(\frac{r\cos\mu - r\cos\lambda}{d + r\sin\lambda - r\sin\mu}\right) \\ p_{\mathrm{RSR}} &= \left(2r^2 + d^2 - 2r^2\cos(\lambda-\mu) + 2rd(\sin\mu - \sin\lambda)\right)^{1/2} \end{aligned} \tag{4.53}$$

$$\tau_{\mathrm{RSR}} = r\tan\gamma(\mu - \lambda + 2t) + p\tan\gamma_G \tag{4.54}$$

For LSL we have

$$\begin{aligned} t_{\mathrm{LSL}} &= \lambda - \tan^{-1}\left(\frac{r\cos\lambda - r\cos\mu}{d - r\sin\lambda + r\sin\mu}\right) \\ q_{\mathrm{LSL}} &= -\mu\{\bmod 2\pi\} + \tan^{-1}\left(\frac{r\cos\lambda - r\cos\mu}{d - r\sin\lambda + r\sin\mu}\right)\{\bmod 2\pi\} \\ p_{\mathrm{LSL}} &= \left(2r^2 + d^2 - 2r^2\cos(\lambda-\mu) + 2rd(\sin\mu - \sin\lambda)\right)^{1/2} \end{aligned} \tag{4.55}$$

$$\tau_{\mathrm{LSL}} = r\tan\gamma(\lambda - \mu) + p\tan\gamma_G \tag{4.56}$$

For LRL we have

$$\begin{aligned} t_{\mathrm{LRL}} &= \lambda + \frac{p}{2} - \tan^{-1}\left(\frac{r\cos\lambda - r\cos\mu}{d - r\sin\lambda + r\sin\mu}\right) \\ q_{\mathrm{LRL}} &= \lambda - t_{\mathrm{LRL}} + p_{\mathrm{LRL}} - \mu \\ p_{\mathrm{LRL}} &= \cos^{-1}\left[\frac{1}{8}\left(6 + 2\cos(\lambda-\mu) + \frac{2d}{r}(\sin\lambda - \sin\mu) - \frac{d^2}{r^2}\right)\right] \end{aligned} \tag{4.57}$$

$$\tau_{\mathrm{LRL}} = r\tan\gamma(\lambda - \mu + 2p) \tag{4.58}$$

And finally for RLR we have

$$t_{\mathrm{RLR}} = \left(-\lambda + \frac{p}{2} + \tan^{-1}\left(-\frac{r\cos\lambda + r\cos\mu}{d + r\sin\lambda - r\sin\mu}\right)\right)$$

$$q_{\mathrm{RLR}} = \mu - \lambda - t_{\mathrm{LRL}} + p_{\mathrm{LRL}} - \mu \tag{4.59}$$

$$p_{\mathrm{RLR}} = \cos^{-1}\left[\frac{1}{8}\left(6 + 2\cos(\lambda - \mu) - \frac{2d}{r}(\sin\lambda - \sin\mu) - \frac{d^2}{r^2}\right)\right]$$

$$\tau_{\mathrm{RLR}} = r\tan\gamma(\mu - \lambda + 2p) \tag{4.60}$$

To find a modified Dubins path with a fixed final time we select an initial guess value for σ, from which γ and V and r are calculated by Eqs. 3.18, 3.22, and 4.40, respectively. The cost (time) of the Dubins path is then computed. The value of σ is iterated on using a secant method until the time of the modified Dubins path equals the specified final time for the trajectory. This process is done in a preferred order among the 6 possible turn sequences, starting with the sequence corresponding to the minimum-time path and then in the order of RSR, LSL, RSL, LSR, LRL, and RLR. When the solution is found for a path, the process stops and no further search is done. Only when it is determined that the solution does not exist for a particular turn sequence, the search is continued using the next sequence.

The convergence of this method is well behaved as long as the distance between the turn centers is sufficiently large and/or the normalized altitude margin is less than one. One can see from the above equations that the cost of each Dubins path (i.e. τ_{RSR}, τ_{LSL}, τ_{RSL}, τ_{LSR}, τ_{RLR}, and τ_{LRL}) is at least piecewise-continuous in r. However, not all Dubins paths exist for a given set of initial conditions (λ, μ, and d) and a given r. For example, we see that the RSL and LSR paths fail to exist when r is increased beyond a certain threshold (as p_{RSL} and p_{LSR} become imaginary). Similarly, the LRL and RLR paths fail to exist when r is decreased beyond a certain threshold (as p_{RLR} and p_{LRL}

become imaginary). The RSR and LSL paths exist for all $r > 0$, however τ_{RSR} and τ_{LSL} are piecewise continuous in r, where a jump discontinuity exists for sufficiently large r. What all this means is that there are cases for which no modified Dubins path exists with a cost equal to the specified τ_f, even though a feasible trajectory does exist in the case that leads from the given initial condition to the specified final condition at the specified final time. This possibility of nonexistence of modified Dubins path in a feasible case arises as a consequence of limiting the search for trajectory in a finite-dimensional space defined by the 6 path sequences while the original problem is in infinite dimensional functional space. Expanding the number of path sequences may remedy some of the cases, but cannot eliminate the problem as the expanded search space is still finite dimensional. In Ref. (18) an extended set of turn sequence is used for trajectory search using Dubins paths. Still the nonexistence problem is noted in certain cases.

CHAPTER 5. REAL-TIME ON-BOARD WIND ESTIMATION

In this chapter we present a filter for the real-time estimation of the local wind speed and direction on-board the parafoil system. Wind plays a pivotal role in the motion of parafoils and other gliding parachutes. For autonomous parafoils this can severely complicate the guidance task as the vehicle airspeed is on the order of the wind speed. For lightly loaded parafoils there may be cases where the wind speed exceeds the vehicle airspeed making it impossible for the vehicle to make forward progress with respect to the ground. For accurate landing precision the wind profile must be taken into account. However, the wind profile is often not known or only approximately known a priori due to the difficulty in forecasting the wind and also because the wind profile varies in both space and time. Therefore it is desirable to have an on-board capability for measuring the local wind field for use in guidance planning.

5.1 Problem Formulation

The inertial velocity vector of a parafoil in the presence of wind is the sum of the vehicle airspeed vector and the wind speed vector as indicated in Figure 5.1, where $V_A = V\cos\gamma$ is the magnitude of the planar (horizontal) airspeed, ψ is the azimuth of the airspeed velocity vector, V_W is the wind speed magnitude, ψ_W is the azimuth of the wind vector, V_I is the magnitude of the planar inertial velocity, and χ is the azimuth of the inertial velocity vector, also referred to as the course angle. The inertial coordinate

frame is chosen such that the x and y axes point North and East, respectively, and all angles are measured clockwise from North.

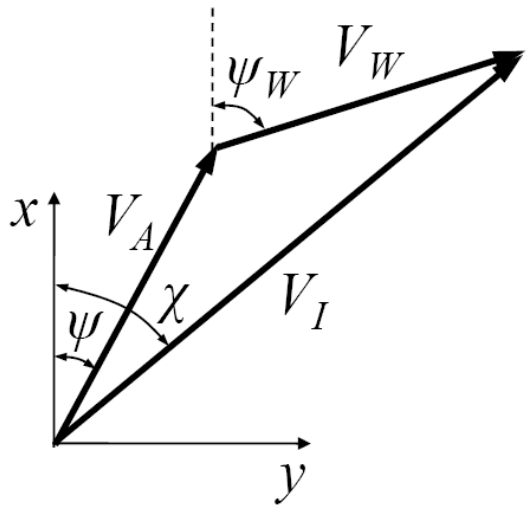

Figure 5.1 The relationship between the the airspeed vector V_A, the wind speed vector V_W, and the inertial velocity vector V_I.

Using Figure 5.1 the x and y components of the inertial velocity can be written as

$$V_I \cos\chi = V_A \cos\psi + V_W \cos\psi_W \quad (5.1)$$

$$V_I \sin\chi = V_A \sin\psi + V_W \sin\psi_W \quad (5.2)$$

Rearranging we have

$$w_x = V_W \cos\psi_W = V_I \cos\chi - V_A \cos\psi \quad (5.3)$$

$$w_y = V_W \sin\psi_W = V_I \sin\chi - V_A \sin\psi \quad (5.4)$$

Eqs. 5.3 and 5.4 indicate that the x and y components of the wind profile can be measured if V_I, χ, V_A, and ψ can be measured. The inertial velocity and course V_I and χ can be measured directly with a Global Positioning System (GPS) receiver, or are available as output from an inertial navigation system (INS). Determining the

airspeed azimuth can be done with a digital compass or an INS. These sensors provide the azimuth of some fixed axis on the body with respect to inertial coordinates and must be correlated to the airspeed measurement to determine the airspeed azimuth. The INS or compass output can only be used directly if the measurement axis is collinear with the axis of the air-data system. Measuring the airspeed magnitude V requires an air-data system (ADS). This may include tri-axial pitot-static probes or a single-axis probe with angle-of-attack and sideslip sensors. If the payload is a returning spacecraft such as the NASA X-38 Crew Return Vehicle, a flush air-data system (FADS) may be available to provide the airspeed measurement. Assuming the vertical component of the wind is zero, the horizontal component of the airspeed can be extracted if both V and the vertical inertial velocity V_z are measured.

In general, the measurements are corrupted by noise. The measured values can be written as

$$V_{I_m} = V_I + \delta V_I \tag{5.5}$$

$$V_{z_m} = V_z + \delta V_z \tag{5.6}$$

$$\chi_m = \chi + \delta\chi \tag{5.7}$$

$$V_m = V + \delta V \tag{5.8}$$

$$\psi_m = \psi + \delta\psi \tag{5.9}$$

The typical error statistics for the δ quantities above for various sensors are given in Table 5.1.

We wish to estimate the wind components w_x and w_y as defined in Eqs. 5.3 and 5.4. The standard process models used for tracking random signals are linear in the filter states. However, we see that these quantities are a nonlinear function of the available measurements. This is because the physical quantities being measured are naturally expressed in polar coordinates whereas the desired quantities are given in Cartesian coordinates. In the current formulation, this would require the use of a nonlinear filter

Measurement	RMS Error
Commercial 12-Channel GPS	
Inertial Velocity	0.1–0.2 Knots
Inertial Course	0.1–0.4°
Digital Compass	
Heading Noise	1–5°
Heading Bias	0–2°
Air Data System	
Airspeed Magnitude	1–3 m/s
Airspeed Bias	0–2 m/s

Table 5.1 Typical measurement errors for low-cost, commercially available sensors.

such as an Extended Kalman Filter or and Unscented (Sigma-Point) Kalman filter. The nonlinear Kalman filter implementations require careful tuning to achieve filter consistency and to avoid divergence. Since the nonlinearity arises from the nature of the measurements we will form pseudo-measurements that are linear in the filter states, allowing a linear Kalman filter implementation.

5.2 Forming the Filter Measurements

The first step in forming the required measurements is to extract the horizontal component of the airspeed magnitude from the available measurements. The airspeed magnitude and the vertical component of the inertial velocity can be used to determine the horizontal component of the airspeed vector. The vertical component of the inertial velocity is often available as a direct output of a GPS receiver or INS and is given by

$$V_z = V \sin \gamma \tag{5.10}$$

assuming that the vertical component of the wind profile is zero. The horizontal component of the airspeed is

$$V_A = V \cos\gamma \tag{5.11}$$

The horizontal airspeed measurement is then given by

$$V_A = \left(V^2 - V_z^2\right)^{1/2} \tag{5.12}$$

The mean and covariance of the horizontal airspeed 'measurement' based on the mean and covariance of the measurements of V_{z_m} and V_m are be found using the Unscented Transformation described in Appendix D.

The next step is to form the pseudo-measurements of the wind components w_x and w_y. This involves a polar-to-Cartesian coordinate transformation of both the airspeed vector and the inertial velocity vector. In Appendix C we show that blindly applying the standard conversion introduces a bias in the measurement mean and errors in the measurement covariance matrix. Therefore the unbiased conversion presented in Appendix C is used to create direct 'measurements' of the wind velocity components. In doing so we assume either the sideslip angle is zero or it has been accounted for in the measurement of ψ. Using Eqs. 5.3 and 5.4 we have

$$w_{x_m} = \lambda_\chi^{-1} V_{I_m} \cos\chi_m - \lambda_\psi^{-1} V_{A_m} \cos\psi_m \tag{5.13}$$

$$w_{y_m} = \lambda_\chi^{-1} V_{I_m} \sin\chi_m - \lambda_\psi^{-1} V_{A_m} \sin\psi_m \tag{5.14}$$

where λ_χ and λ_ψ are defined in Table C.1 in Appendix C.

Let $\mathbf{R}_I$ denote the covariance of the inertial speed transformation and $\mathbf{R}_A$ denote the covariance of the airspeed transformation where the components of the covariance matrices are given by Eqs. C.14–C.16. If we assume that the errors in the airspeed and inertial velocity conversions are uncorrelated, the covariance matrix for the wind component measurements is given by

$$\mathbf{R}_k = \mathbf{R}_I + \mathbf{R}_A \tag{5.15}$$

Measurement	RMS Error
V_I	0.7 m/s
V_z	0.7 m/s
χ	2°
V	2 m/s
ψ	2°

Table 5.2 RMS measurement errors used in all simulations.

since the measurement errors are independent. This measurement covariance matrix can be used with any of the process models described in Appendix B and can also be used to determine the measurement variance for the fading memory filter that will be described in Section 5.5.

5.3 Simulated Measurements

To evaluate various filter designs we simulate the parafoil model in Eqs. 3.1–3.8. The canopy and loading are such that the nominal airspeed magnitude V=20 m/s and L/D=3. The measurement error statistics used in all simulations are given in Table 5.2. The initial altitude is set to 500 meters and the trajectory is a nominal example of a minimum control energy trajectory as discussed in Chapter 4. The wind profile considered is shown in Figure 5.2 and was generated by balloon sounding (43). The profile was selected for the level of wind speed variation along both axes. The ground track of the flown trajectory is shown in Figure 5.3. The sample time is selected as 5 Hz and the simulated measurements are given in Figure 5.4.

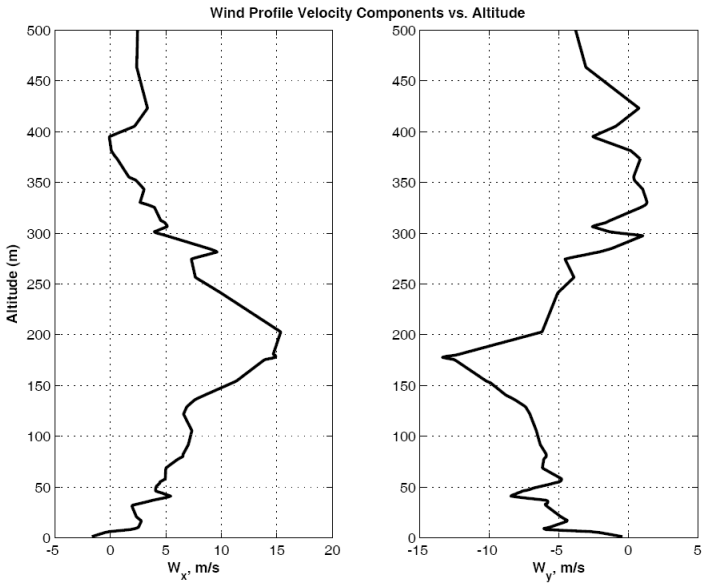

Figure 5.2 The wind profile used to generate simulated sensor measurements.

5.4 Wind Estimate Using Noisy Measurements Only

One might wonder the accuracy that can be achieved using only the noisy measurements. The tracking error was calculated by comparing the output of Eqs. 5.13 and 5.14 to the actual wind profile and the typical result is shown in Figure 5.5. The standard deviation for one example run was 1.42 and 1.88 m/s for the x and y components, respectively. The maximum error for both channels was approximately 5 m/s. The tracking error using only noisy measurements is a significant fraction of the vehicle airspeed and thus not suitable for use in practice.

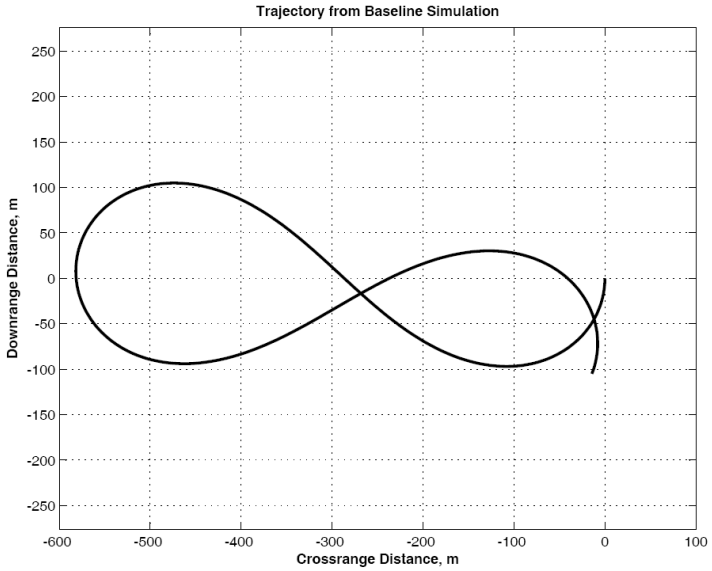

Figure 5.3 The ground track of the nominal trajectory used to generate simulated sensor measurements.

5.5 Wind Estimate Using a Fading Memory Filter

In this section we consider a first-order fading memory filter to reduce the tracking error. The filter update equation for each channel is given by

$$\hat{x}_k = \hat{x}_{k-1} + (1-\beta)(x_k^* - \hat{x}_{k-1}) \tag{5.16}$$

where $\hat{x}_k$ is the filter estimate at the k^{th} interval, β is the filter gain, and x_k^* is the measurement at the k^{th} interval. The variance of the estimation error can be shown to be

$$P_{11} = \left(\frac{1-\beta}{1+\beta}\right)\sigma^2 \tag{5.17}$$

where σ is the standard deviation of the input signal.

The filter equation is applied to each of Eqs. 5.13–5.14 and the typical tracking error for β=0.85 is shown in Figure 5.6. The dotted lines correspond to the variance bounds calculated using Eq. 5.17. Theoretically the tracking error should lie within

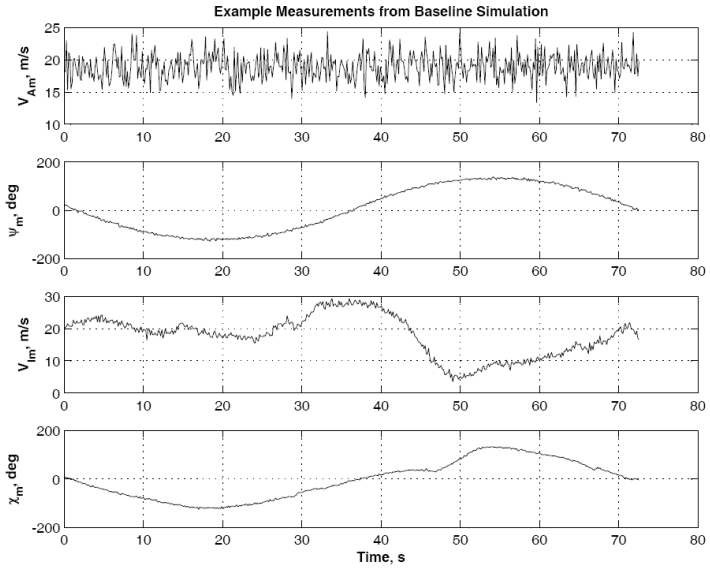

Figure 5.4 Simulated sensor measurements for the nominal trajectory.

those bounds 66% of the time if the filter is consistent, which appears to be the case here. The standard deviation for one example run was 0.73 and 0.78 m/s for the x and y components, respectively. The maximum tracking error in this example was 3 m/s with typical tracking errors less than 1 m/s. We see that using a very simple filter reduces the standard deviation of the tracking error by approximately 50%. and provides a much more reasonable estimate of the wind.

5.6 Wind Estimate Using a WNV Kalman Filter

In this section we apply a linear Kalman filter using the White Noise Velocity process model described in Appendix B. The Kalman filter equations are given in Appendix A. The state vector, fundamental matrix, process covariance matrix, and measurement matrices corresponding to this process model are given in Table 5.3.

The typical tracking error using $\Phi_s = 1.0$ is shown in Figure 5.7. The dotted lines correspond to the variance of the state estimated by the Kalman filter. The standard

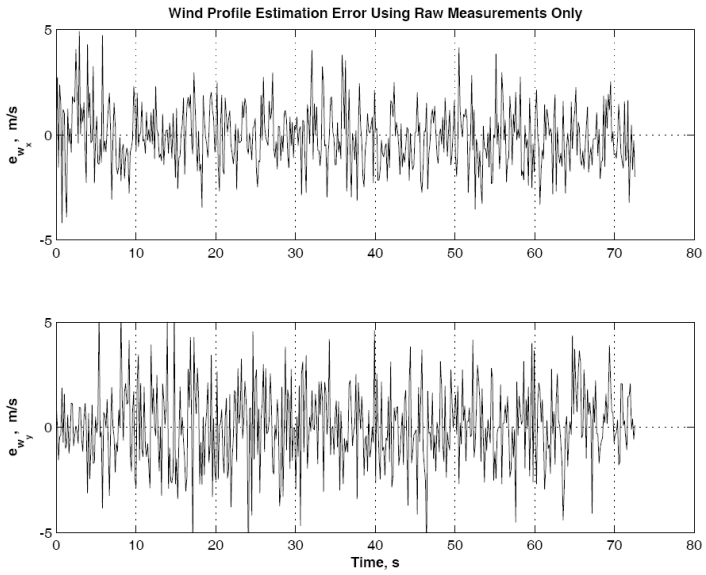

Figure 5.5 Tracking errors using the unbiased converted measurements only along the x- (top) and y-axes (bottom).

deviation for the example run shown here was 0.67 and 0.78 m/s for the x and y channels, respectively. The maximum tracking error was 3 m/s for this example, with typical tracking errors less than 1 m/s. Overall we see a minor improvement in tracking performance over the fading memory filter.

5.7 Wind Estimate Using a WNA Kalman Filter

In this section attempt to improve upon the performance of the WNV Kalman filter by increasing the order of the assumed state model. We now apply a linear Kalman filter using the White Noise Acceleration process model described in Appendix B. The state vector, fundamental matrix, process covariance matrix, and measurement matrices corresponding to this process model are given in Table 5.4.

The typical tracking error using $\Phi_s = 0.80$ is shown in Figure 5.8. This is the same case as presented in the previous section and the output of this second-order filter

$\mathbf{x} = \begin{bmatrix} w_x \\ w_y \end{bmatrix}$	$\mathbf{\Phi}_k = \begin{bmatrix} 1 & 0 \\ 0 & 1 \end{bmatrix}$
$\mathbf{Q}_k = \Phi_s \begin{bmatrix} 1 & 0 \\ 0 & 1 \end{bmatrix}$	$\mathbf{H} = \begin{bmatrix} 1 & 0 \\ 0 & 1 \end{bmatrix}$

Table 5.3 The state vector, fundamental matrix, process noise covariance matrix, and measurement matrix for the WNV process model.

$\mathbf{x} = \begin{bmatrix} w_x \\ \dot{w}_x \\ w_y \\ \dot{w}_y \end{bmatrix}$	$\mathbf{\Phi}_k = \begin{bmatrix} 1 & T & 0 & 0 \\ 0 & 1 & 0 & 0 \\ 0 & 0 & 1 & T \\ 0 & 0 & 0 & 1 \end{bmatrix}$
$\mathbf{Q}_k = \Phi_s \begin{bmatrix} \frac{T^3}{3} & \frac{T^2}{2} & 0 & 0 \\ \frac{T^2}{2} & T & 0 & 0 \\ 0 & 0 & \frac{T^3}{3} & \frac{T^2}{2} \\ 0 & 0 & \frac{T^2}{2} & T \end{bmatrix}$	$\mathbf{H} = \begin{bmatrix} 1 & 0 & 0 & 0 \\ 0 & 0 & 1 & 0 \end{bmatrix}$

Table 5.4 The state vector, fundamental matrix, process noise covariance matrix, and measurement matrix for the WNA process model.

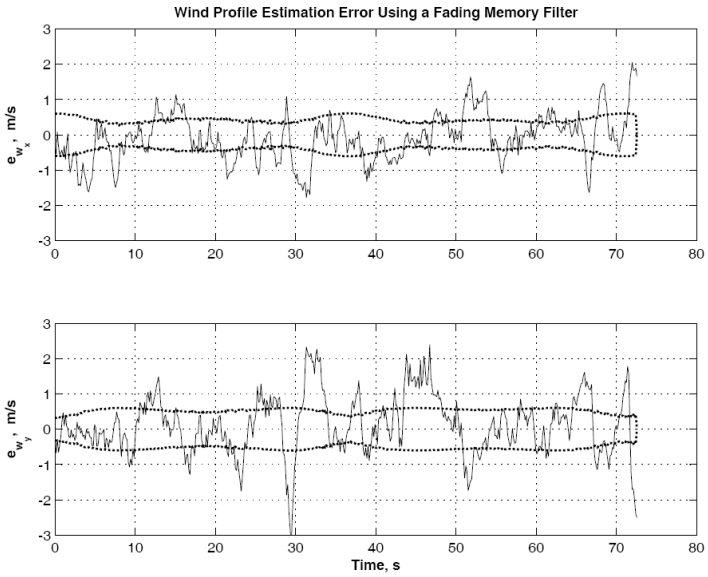

Figure 5.6 Tracking errors using a first-order fading memory filter with β=0.85 along the x- (top) and y-axes (bottom). The dotted lines correspond to the predicted variance calculated using Eq. 5.17.

appears identical to the output of the first-order filter. However, the standard deviation for the second order filter was 0.72 and 0.81 m/s for the x and y channels, respectively. Thus we see a decrease in filter performance with increasing order for this example. This trend was found to be consistent when using other trajectories and wind profiles.

5.8 Wind Estimate Using a WPA Kalman Filter

Although we saw a decrease in performance when moving from the WNV filter to the WNA filter, it is possible that a further increase in filter order will yield better results. We now apply a linear Kalman filter using the Wiener Process Acceleration model described in Appendix B. The state vector, fundamental matrix, process covariance matrix, and measurement matrices corresponding to this process model are given in Table 5.5.

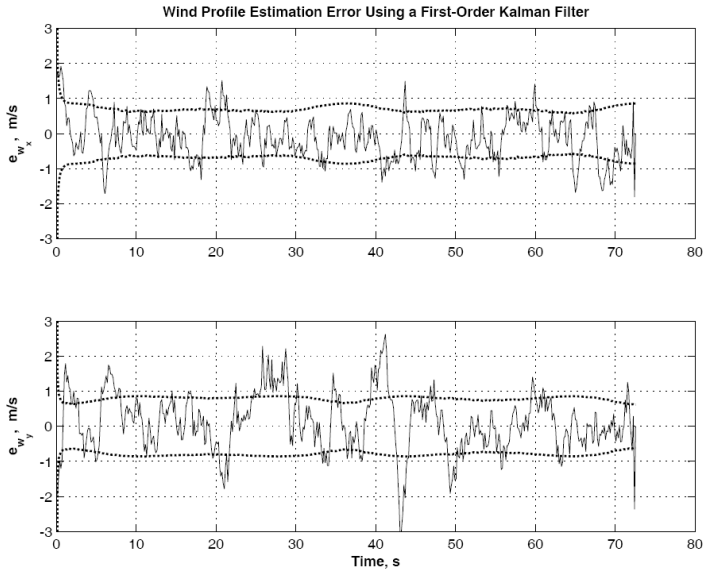

Figure 5.7 Tracking errors using a Kalman filter with a White Noise Velocity process model with Φ_s=1.0 along the x- (top) and y-axes (bottom). The dotted lines correspond to the square-root of the predicted variance estimate provided by the filter.

Using the same example as in the previous two sections, the typical tracking error using $\Phi_s = 2.0$ is shown in Figure 5.9. The standard deviation for this third-order filter was 0.73 and 0.86 m/s for the x and y channels, respectively. The typical tracking error is on the order of 1 m/s and is visibly worse than for the first- or second-order filters.

Our conclusion is then that there is no benefit to increasing filter order above first order using the WNV process model. Furthermore, for systems in which computational power is limited, we see that a first-order fading memory filter offers similar performance to the WNV Kalman filter implementation and only requires scalar operations. We see that RMS wind measurement errors on the order of 1 m/s are possible even with measurements containing more noise than typical commercial off-the-shelf sensors are used.

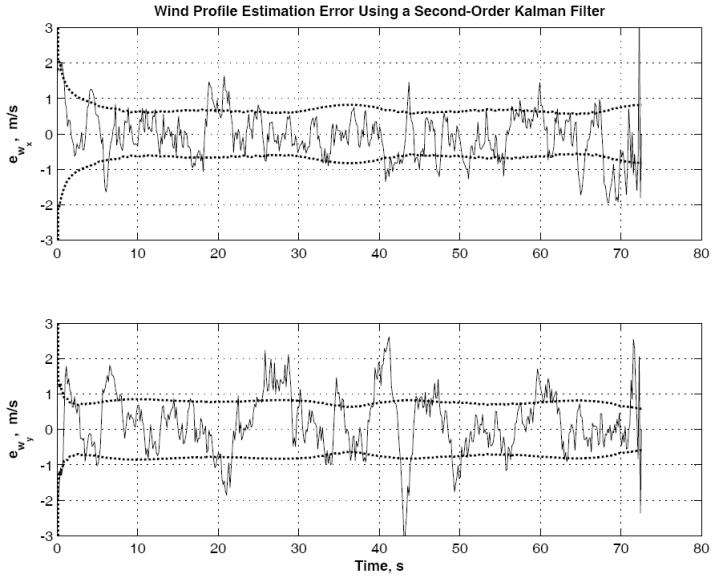

Figure 5.8 Tracking errors using a Kalman filter with a White Noise Acceleration process model with Φ_s=0.8 along the x- (top) and y-axes (bottom). The dotted lines correspond to the square-root of the predicted variance estimate provided by the filter.

$$\mathbf{x} = \begin{bmatrix} w_x \\ \dot{w}_x \\ \ddot{w}_x \\ w_y \\ \dot{w}_y \\ \ddot{w}_y \end{bmatrix} \qquad \mathbf{\Phi}_k = \begin{bmatrix} 1 & T & \frac{T^2}{2} & 0 & 0 & 0 \\ 0 & 1 & T & 0 & 0 & 0 \\ 0 & 0 & 1 & 0 & 0 & 0 \\ 0 & 0 & 0 & 1 & T & \frac{T^2}{2} \\ 0 & 0 & 0 & 0 & 1 & T \\ 0 & 0 & 0 & 0 & 0 & 1 \end{bmatrix}$$

$$\mathbf{Q}_k = \Phi_s \begin{bmatrix} \frac{T^5}{20} & \frac{T^4}{8} & \frac{T^3}{6} & 0 & 0 & 0 \\ \frac{T^4}{8} & \frac{T^3}{3} & \frac{T^2}{2} & 0 & 0 & 0 \\ \frac{T^3}{6} & \frac{T^2}{2} & T & 0 & 0 & 0 \\ 0 & 0 & 0 & \frac{T^5}{20} & \frac{T^4}{8} & \frac{T^3}{6} \\ 0 & 0 & 0 & \frac{T^4}{8} & \frac{T^3}{3} & \frac{T^2}{2} \\ 0 & 0 & 0 & \frac{T^3}{6} & \frac{T^2}{2} & T \end{bmatrix} \qquad \mathbf{H} = \begin{bmatrix} 1 & 0 & 0 & 0 & 0 & 0 \\ 0 & 0 & 0 & 1 & 0 & 0 \end{bmatrix}$$

Table 5.5 The state vector, fundamental matrix, process noise covariance matrix, and measurement matrix for the WPA process model.

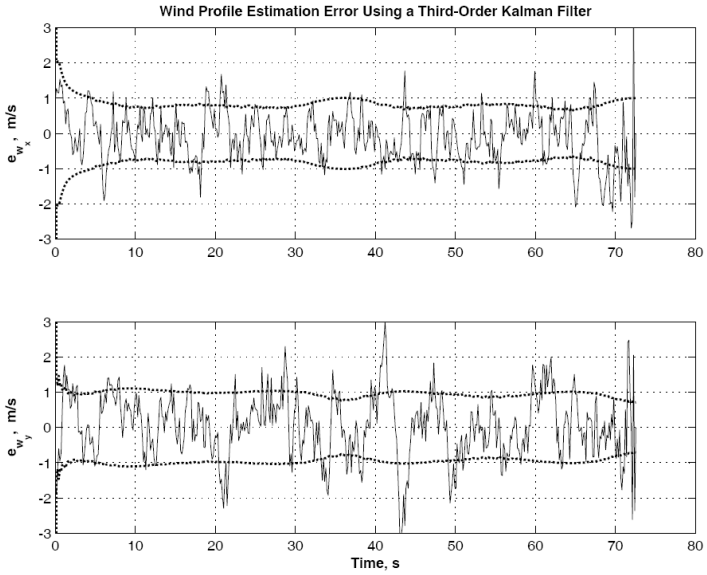

Figure 5.9 Tracking errors using a Kalman filter with a Wiener Process Acceleration model with Φ_s=2.0 along the x- (top) and y-axes (bottom). The dotted lines correspond to the square-root of the predicted variance estimate provided by the filter.

CHAPTER 6. CLOSED LOOP GUIDANCE ALGORITHM

Given the initial condition of the parafoil, the trajectory planning algorithms in Chapter 4 are called on-board to generate a reference trajectory that satisfies all the required conditions/constraints. This reference trajectory provides the guidance information for the parafoil. If the trajectory planning algorithms are called in every guidance cycle to generate the trajectory based on the current navigation data, the profiles from the resulting trajectory provides closed-loop guidance. The guidance is closed-loop in the sense that the guidance commands depend on the current condition. Our proposed trajectory planning/guidance strategy is a hybrid combination of modified Dubins paths and the minimum control-energy paths. The reason for the hybrid approach is to take advantage of the strengths of minimum control-energy and modified Dubins path techniques so as to ensure the solution of a planned trajectory in all feasible cases. The minimum control-energy paths are desired to ease the power requirements of the system by reducing control line winch activity, and the solution is guaranteed to exist as long as the altitude margin is adequate. But robustness of convergence of the search process for the solution requires that the position offset from the target is not excessively large and the normalized altitude margin is greater than approximately one. On the other hand, the modified Dubins path converges well for large offset distances and altitude margins below one, but may suffer from nonexistence of the solution for the particular set of initial conditions and given time (altitude margin) in certain other cases.

Recall that the altitude margin η is the excess maneuvering altitude normalized by the altitude required to complete one full turn at maximum turn rate. At each guid-

ance cycle the reference trajectory from the current position, orientation (azimuth), and altitude to the final position, orientation, and altitude is computed from the following steps:

1. Determine the initial position in the wind-fixed coordinate frame.
2. Determine the altitude required to complete all admissible Dubins paths.
3. Determine the normalized altitude margin η from the optimal (minimum-time) Dubins path.
4. Determine the type of reference trajectory to calculate based on the following:
   - If $\eta > 5$ compute an energy management trajectory (discussed below).
   - If $1 < \eta \leq 5$ compute a minimum control-energy trajectory.
   - If $0 \leq \eta \leq 1$ compute a modified Dubins trajectory.
   - If $\eta < 0$ track directly toward the target to minimize the miss distance.
5. Calculate and store $x^*(\tau)$, $y^*(\tau)$, and $\psi^*(\tau)$

If at any guidance cycle the specified trajectory generation method fails to converge, an attempt is made using the other trajectory generation method. If neither method converges at a given guidance cycle for any reason the last known trajectory is used for the reference trajectory. The guidance logic is summarized in Figure 6.1. The reference trajectory can be re-planned at a specified update rate, or alternatively, the re-planning can be performed only when the trajectory tracking error exceeds a specified threshold.

The energy management trajectory mentioned above is a Dubins path from the current position to a nominal radius circle centered three minimum-turn-diameters from the origin in the wind-fixed frame. The nominal radius is specified by a turn rate equal to 80% of the specified maximum turn rate of the system. The center lies along lines

passing through the origin at $\pm 45°$. The circle is located in the quadrant containing the current position of the system. The circle is tracked until the first guidance cycle update where $\eta \leq 5$. The idea behind this strategy is to bring the system close to the target using as little maneuvering energy as possible. This minimizes the potential drift due to uncertainty in the wind and canopy over- or under-performance. The position of the final turn circle is chosen to allow plenty of maneuvering room when the system exits the energy management phase and to promote rapid convergence of the terminal phase reference trajectory.

An example high margin trajectory is shown in Fig. 6.2. In this case the system has an L/D of one, an airspeed of 12 m/s and a maximum turn rate of $15°/s$. There is no wind in this case to highlight the shape and form of the trajectory. The initial altitude margin for this case was approximately seven.

Observe that the guidance logic is parameterized completely in terms of η which is derived from the specified parafoil performance parameters (L/D, V_0, and $\dot{\psi}_{max}$) and the current conditions. Furthermore, the reduced order model used to generate the reference trajectories also uses these parameters. In this way the guidance algorithm is fully adaptable to parafoil canopies with a wide range of performance characteristics. The guidance algorithm does not need to be re-tuned in any way to accommodate variations in canopy performance.

Another key difference between this algorithm and some previous parafoil guidance algorithms is that the reduction of excess energy is performed near the end of the trajectory rather than early in the trajectory. This tends to make the algorithm more robust to unknown variations in the wind profile as well as errors in the model used for trajectory planning.

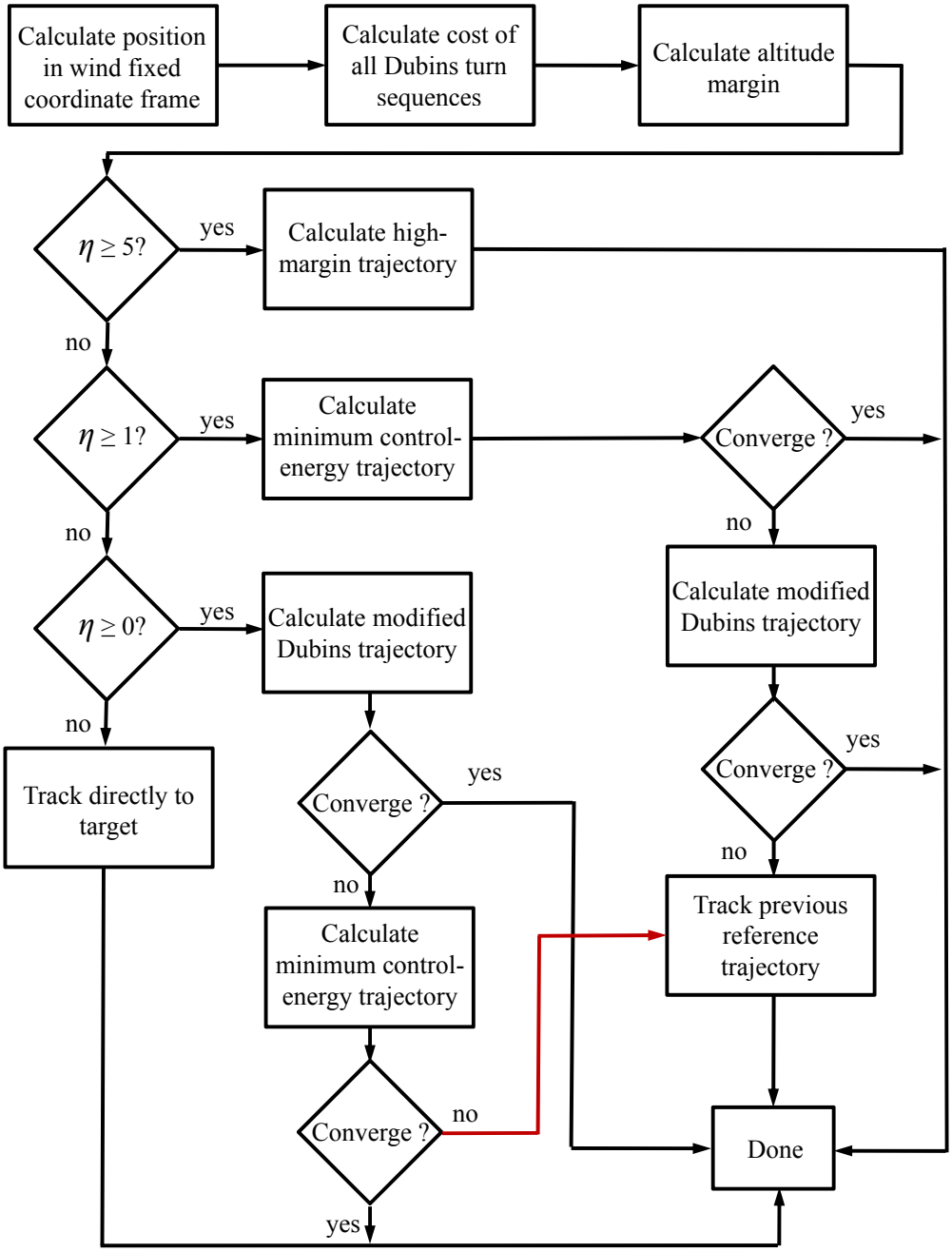

Figure 6.1 Summary of the guidance logic. This sequence is performed at every guidance update.

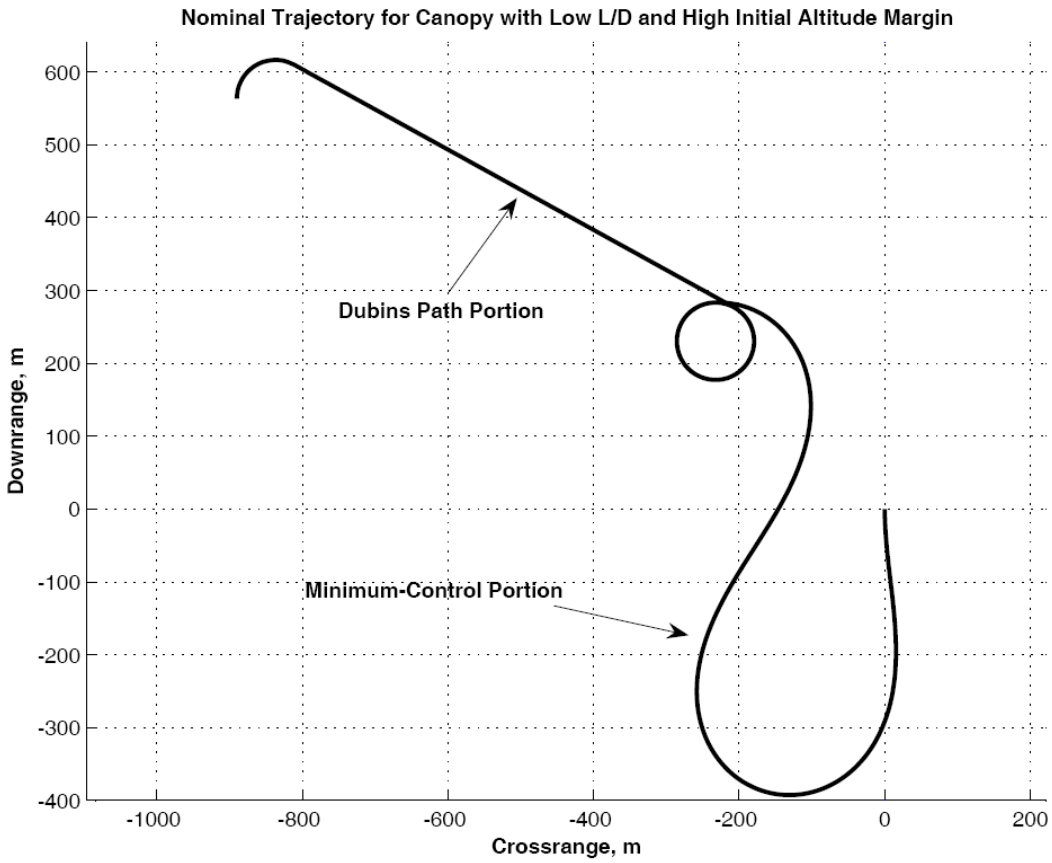

Figure 6.2 An example of a case with a high initial altitude margin ($\eta \cong 7$) for a canopy with $L/D = 1$, $V_0 = 12m/s$, and $\dot{\psi}_{max} = 15°/sec$. The initial Dubins path portion of the energy management phase is clearly distinguished in the upper-left portion of the figure. The terminal phase of the trajectory can be seen in the lower-right portion of the figure.

CHAPTER 7. TRAJECTORY TRACKING CONTROL

Once the trajectory has been planned, the parafoil is controlled to fly the planned trajectory until the reference trajectory is re-planned or updated. In this chapter we present a baseline control design for trajectory tracking. Let the reference trajectory be given by:

$$\mathbf{x}^* = \begin{bmatrix} x^*(\tau) \\ y^*(\tau) \\ \psi^*(\tau) \end{bmatrix} \tag{7.1}$$

and define the tracking error components to be

$$\begin{aligned} e_1 &= x(\tau) - x^*(\tau) \\ e_2 &= y(\tau) - y^*(\tau) \\ e_3 &= \psi(\tau) - \psi^*(\tau) \end{aligned} \tag{7.2}$$

By rotating the tracking error components e_1 and e_2 through an angle ψ^* we can define the along-track and cross-track errors as

$$\begin{aligned} e_{\text{atrack}} &= e_1 \cos\psi^* + e_2 \sin\psi^* \\ e_{\text{xtrack}} &= e_1 \sin\psi^* - e_2 \cos\psi^* \end{aligned} \tag{7.3}$$

The time rate of change of the cross-track error using t rather than τ as the independent variable can be shown to be

$$\dot{e}_{\text{xtrack}} = (\dot{x} - \dot{x}^*)\sin\psi^* - (\dot{y} - \dot{y}^*)\cos\psi^* + ((x - x^*)\cos\psi^* + (y - y^*)\sin\psi^*)\,\dot{\psi}^* \tag{7.4}$$

where $\dot{\psi}^*$ is known given the reference trajectory. From Eqs. (3.4–3.5) we see that to accurately determine $\dot{x}$ and $\dot{y}$ in the wind-fixed coordinate frame requires measurement

of the vehicle airspeed and flight path angle. Accurate measurement of both of these quantities is often difficult and increases the size and weight of the GNC hardware. As such, we use values provided from the equilibrium glide assumption to approximate the cross-track error derivative as

$$\begin{aligned} \dot{e}_{\text{xtrack}} &= V_T \cos\gamma_T \left[(\cos\psi - \cos\psi^*)\sin\psi^* - (\sin\psi - \sin\psi^*)\cos\psi^*\right] \\ &\quad + \left((x - x^*)\cos\psi^* + (y - y^*)\sin\psi^*\right)\dot{\psi}^* \\ &= -V_T \cos\gamma_T \sin e_3 + \left(e_1 \cos\psi^* + e_2 \sin\psi^*\right)\dot{\psi}^* \end{aligned} \tag{7.5}$$

By linearizing the parafoil model in Eqs. (3.1)–(3.8) about a straight-line equilibrium glide condition, one can show that the transfer function from the lateral control input to the cross-track error is given by

$$\frac{e_{\text{xtrack}}(s)}{\sigma_{com}(s)} = \frac{c}{s^2(s + 1/\tau_\sigma)} \tag{7.6}$$

where c is a constant depending on the wing loading and lift to drag ratio. Using a Routh array, one can show that proportional feedback control cannot stabilize this system. Therefore we propose a proportional-plus-derivative (PD) control law for the cross-track control channel so that the commanded input is given by

$$\sigma_{\text{com}} = \sigma^* + k_{p_{lat}} e_{\text{xtrack}} + k_d \dot{e}_{\text{xtrack}} \tag{7.7}$$

where σ^* is the modeled bank angle corresponding to $\dot{\psi}^*$ and $k_{p_{lat}} > 0$ and $k_d > 0$ are appropriately selected constants. This control law will stabilize the cross-track error dynamics as long $k_d/k_{p_{lat}} > \tau_\sigma$.

For the along-track error dynamics, linearization of Eqs. (3.1)–(3.8) yields a fourth-order transfer function for the along-track response due to longitudinal control input ε_{com}. Two poles lie on the real axis, on at the origin and one located at $-1/\tau_\varepsilon$. Furthermore, there is one zero on the real axis and two complex poles in the left-half plane, the locations of which depend on the wing loading and lift to drag ratio of the system.

The zero typically lies to the left of the actuator pole for practical wing loadings and practical values of τ_ε. Therefore, for parafoil systems for which longitudinal control is available we propose a proportional control law for the along-track control channel so that the commanded input is given by

$$\varepsilon_{\text{com}} = k_{p_{lon}} e_{\text{atrack}} \tag{7.8}$$

where we note $\varepsilon_{\text{trim}} = 0$ as discussed above. This control law will stabilize the along-track error dynamics for sufficiently small values of $k_{p_{lon}} > 0$.

CHAPTER 8. SIMULATION RESULTS

In this chapter we present the results of a series of Monte Carlo simulations which were performed to study the robustness of the guidance algorithm to navigation errors, uncertainty in the a priori wind profile, uncertainty in the payload mass, and uncertainty in the canopy performance.

8.1 Simulation Setup

To evaluate the GNC concept, the model in Eqs. 3.1–3.8 is used to represent the true motion of the parafoil. The aerodynamic model from Ref. (37) using parameters given in Table 8.1 is used to generate the lift and drag coefficients as functions of the symmetric flap (brake) deflection and rigging angle. Here we assume that $\dot{\alpha} = 0$ and use the value of α corresponding to a pitching moment of zero. Data are given for rigging angles ranging from $-4°$ to $10°$ at symmetric flap settings of zero, half, and full deflection. We choose to use symmetric flap setting for longitudinal control and select a rigging angle of $4°$ and a trim flap setting of 70% brakes which gives L/D equal to 2.1. The allowable range of symmetric flap deflection is from 50% to 90% (i.e. $\varepsilon \in [-0.2, 0.2]$) which allows L/D to vary from 1.7 to 2.9.

Using the above aerodynamic model we consider two parafoils with significant differences in performance. Parafoil 1 represents a typical small- to mid-scale system characterized by a moderate maximum turn rate and moderate to fast control response. We consider a maximum turn rate of $30°/s$ and a canopy area of 28 m^2 that is lightly

Canopy Area (S)	28 m^2
Aspect Ratio (A)	2.0
Canopy Mass (m_c)	5 kg
Payload Mass (m_p)	135 kg
Line Length to Canopy Span Ratio (R/b)	1.0
Number of Lines (n)	40
Line Diameter (d)	0.0035 m

Table 8.1 Parameters used to generate C_L and C_D vs. symmetric brake deflection using Reference (37).

loaded at 5 kg/m^2 which leads to a glide airspeed of 9.27 m/s and a minimum turn radius of 15.7 m. Parafoil 2 represents a typical large-scale system that is characterized by a slow maximum turn rate and slow control response. We consider a maximum turn rate of 10°/s and a canopy area of 560 m^2 that is highly loaded at 20 kg/m^2 which leads to a glide airspeed of 18.5 m/s and a minimum turn radius of 98.1 m. These and other parameters required for the simulation and guidance algorithm are summarized in Table 8.1. The trajectory planning algorithm uses a maximum turn rate that is 80% of the nominal value both to increase robustness to parameter uncertainty and to allow sufficient control margin for the tracking controller.

Real-world wind data are used in all simulations. The wind profiles are randomly selected from a database containing the daily NOAA balloon sounding profiles(43). The wind data are linearly interpolated between data points and the wind speeds were scaled so that they do not exceed 30 m/s. The initial altitude is fixed to 600 m for Parafoil 1 and 1200 m for Parafoil 2 for all simulations. The initial position is uniformly dispersed within a 800-meter square centered on the position of the target in the wind fixed coordinate frame, where the a-priori wind profile is used to calculate the position in the wind-fixed frame. The initial heading is uniformly dispersed between 0 and 2π.

The terminal portion of a typical closed-loop trajectory for Parafoil 1 in the presence

Parameter	Parafoil 1	Parafoil 2
Equilibrium Glide Velocity (V_0)	9.27 m/s	18.5 m/s
Equilibrium Glide Path Angle (γ_G)	$-25.2°$	$-25.2°$
Maximum Turn Rate ($\dot{\psi}_{\max}$)	$30°/s$	$10°/s$
Maximum Bank Rate ($\dot{\sigma}_{\max}$)	$30°/s$	$5°/s$
Maximum Lon. Control Rate ($\dot{\varepsilon}_{\max}$)	20%/s	10%/s
Bank Time Constant (τ_σ)	1.0	2.0
Lon. Control Time Constant (τ_ε)	0.8	2.0
Lon. Control Proportional Gain ($k_{p_{lon}}$)	0.06	0.012
Lat. Control Proportional Gain ($k_{p_{lat}}$)	0.026	0.013
Lat. Control Derivative Gain (k_d)	0.04	0.0665

Table 8.2 Parameters required by the guidance algorithm and for the simulation.

of wind uncertainty is shown in Fig. 8.1. In this case only lateral control was used and the reference trajectory was re-planned whenever the tracking error exceeded 10 meters. The dark arrows indicate the true wind velocity and direction, and the light arrows indicate the expected wind velocity and direction from the a priori wind profile. In this case, the true wind velocity is nearly half of the expected value for most of the trajectory. The closed-loop guidance was able to overcome the wind uncertainty and the final miss distance was 12 meters.

8.2 Sensitivity to Sensor Noise

Figures 8.2 and 8.3 present the results from 100 simulated drops of Parafoil 1 and Parafoil 2, respectively, that have perfect knowledge of the wind profile ($\tilde{\mathbf{W}}(\tau) = 0$). In the simulations navigation errors/uncertainty with statistics given in Table 3 are added that are unknown to the guidance and control. For each of the dispersed cases the simulation is performed with both longitudinal and cross-track control and with only cross-track control only, respectively. The dashed circles correspond to one and two minimum turn radii. It is illustrative to compare the landing position with the system

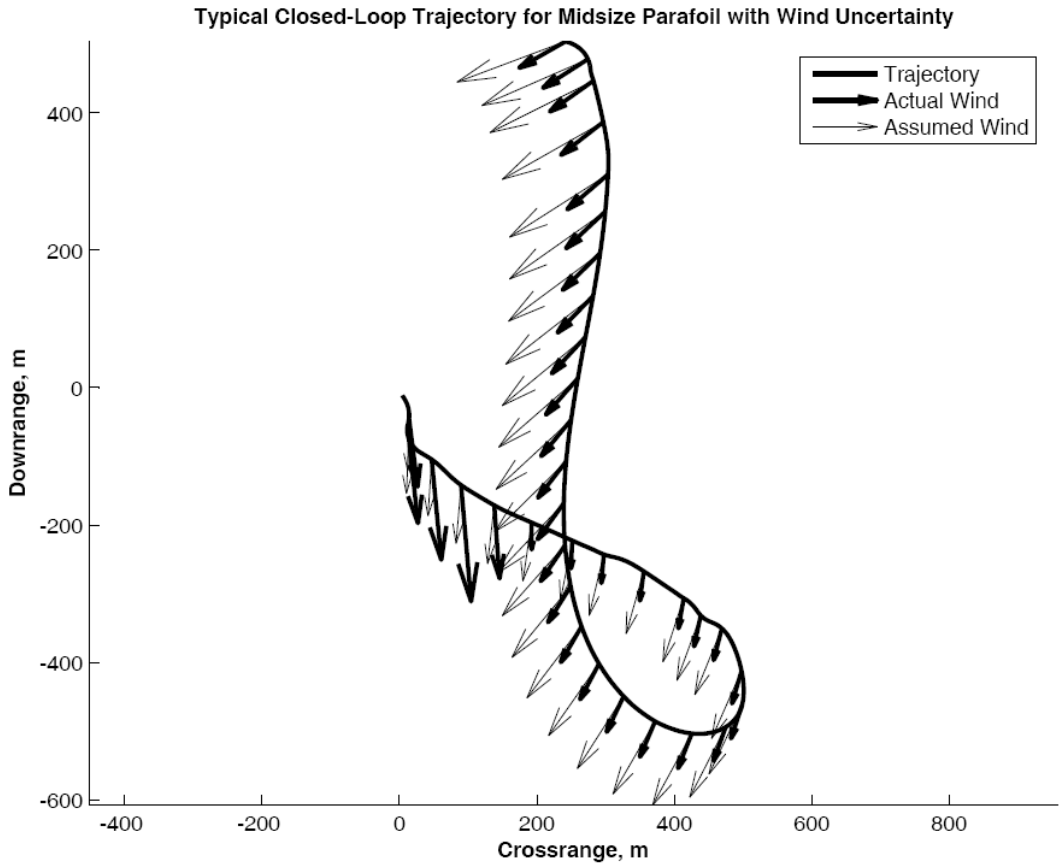

Figure 8.1 This is the terminal phase of a typical closed-loop trajectory for Parafoil 1 in the presence of wind uncertainty. Observe that the true wind velocity magnitude (dark) is nearly half of the expected value (light) for most of the trajectory.

turn radius as this gives reference to the maneuverability of the system. For Parafoil 1, the average and maximum miss distances for this case are 1.8 and 4.5 m for the system with both longitudinal and lateral control and 2.2 and 10.4 m for the system with only lateral control. For Parafoil 2, the average and maximum miss distances are 5.24 and 11.45 m for the system with both longitudinal and lateral control and 6.42 and 19.61 m for the system with only lateral control. We see that for both Parafoil 1 and Parafoil 2 that all landings occur well within one minimum turn radii and that the landing errors

Position Error	< 1 m, time-correlated
Altitude Error	< 1.7 m, time-correlated
Compass Bias	2° (1σ)
Compass Noise	2° (1σ)

Table 8.3 Sensor error statistics.

are larger in the downrange direction with the effect more pronounced for the system without longitudinal control. The elongation is primarily due to errors in the measured altitude, as every meter of altitude measurement error corresponds to approximately 2 meters of landing error in the absence of wind and at nominal $\varepsilon = 0$.

8.3 Sensitivity to Payload Mass Dispersion

Uncertainty in the payload mass leads to errors in the wing loading and thus the glide airspeed. Uncertainty in the glide airspeed introduces errors into the estimation of position in the wind fixed coordinate frame (see Eqs. 3.30–3.31) and errors in the modeled turn rate for a given flap deflection. The mass for each simulation run is modeled as

$$m = m_{\text{nom}}(1 + \delta) \tag{8.1}$$

where m_{nom} is the expected mass value and δ is a zero-mean Gaussian-distributed random variable.

Figures 8.4 and 8.5 show the results of 100 simulated drops of Parafoil 1 and Parafoil 2, respectively, for which δ has a standard deviation $\sigma = 0.05$. For Parafoil 1 the average and maximum miss distances are 0.35 and 0.90 m for the system with both longitudinal and lateral control and 2.60 and 11.8 m for the system with only lateral control. For Parafoil 2 the average and maximum miss distances are 1.04 and 3.31 m for the system with both longitudinal and lateral control and 5.49 and 25.02 m for the system with

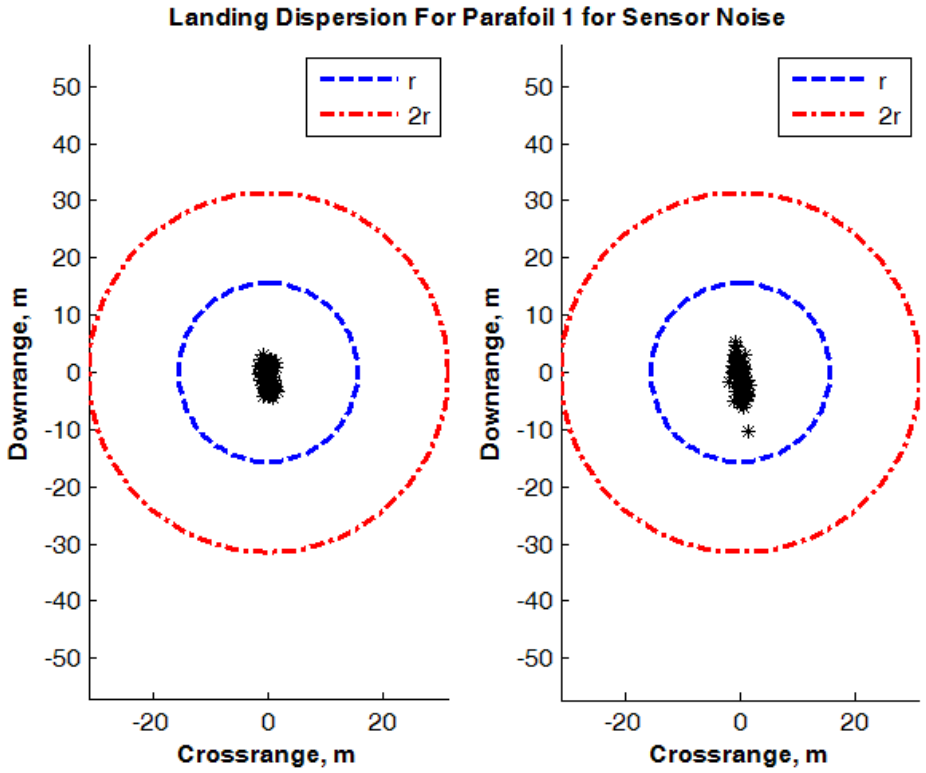

Figure 8.2 Landing dispersion results for Parafoil 1 for the case where the wind profile is perfectly known and navigation errors are present. Left: System with longitudinal and lateral control. Right: System with lateral control only.

only lateral control.

Figures 8.6 and 8.7 show the results of 100 simulated drops of Parafoil 1 and Parafoil 2, respectively, for which δ has a standard deviation $\sigma = 0.10$. For Parafoil 1 the average and maximum miss distances are 0.6 and 22.9 m for the system with both longitudinal and lateral control and 4.3 and 26.2 m for the system with only lateral control. For Parafoil 2 the average and maximum miss distances are 1.52 and 7.81 m for the system with both longitudinal and lateral control and 7.69 and 108.7 m for the system with only lateral control.

We see for both Parafoil 1 and Parafoil 2 that the system with both control channels

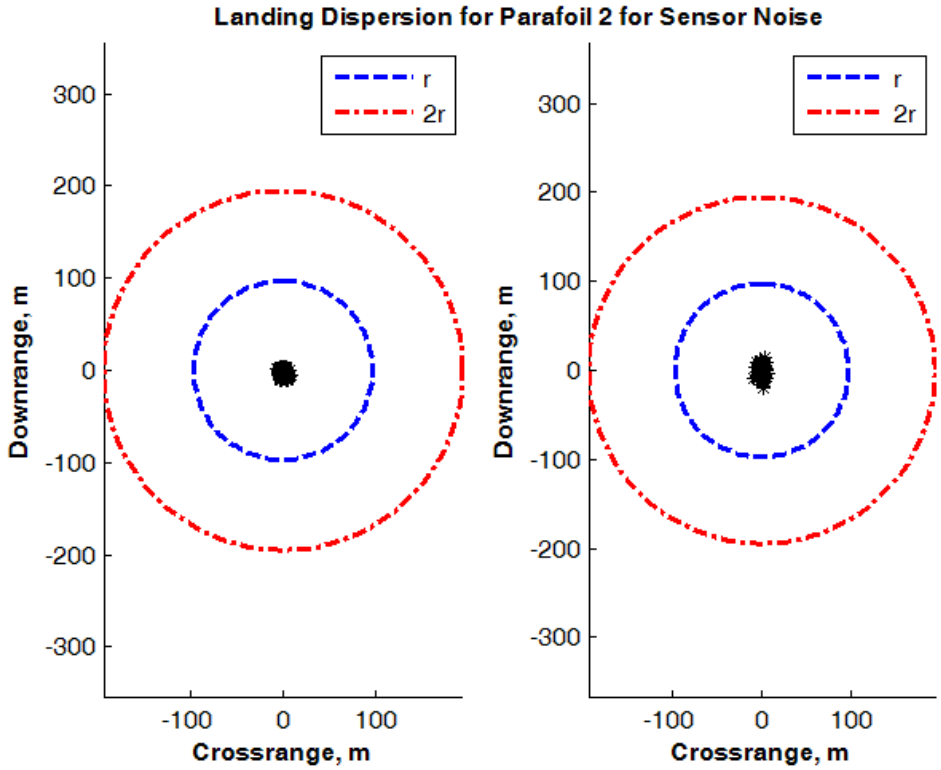

Figure 8.3 Landing dispersion results for Parafoil 2 for the case where the wind profile is perfectly known and navigation errors are present. Left: System with longitudinal and lateral control. Right: System with lateral control only.

are largely insensitive to variations in mass while the system with only lateral control see a degradation in landing accuracy. However, even with large dispersions in payload mass, both Parafoil 1 and Parafoil 2 are are able to land within one minimum turn radii 98% of the time.

8.4 Sensitivity to C_L and C_D Dispersions

Uncertainty in the trim values of C_L and C_D lead to errors in both the expected glide path angle and the expected glide airspeed.The true trim lift and drag coefficients for

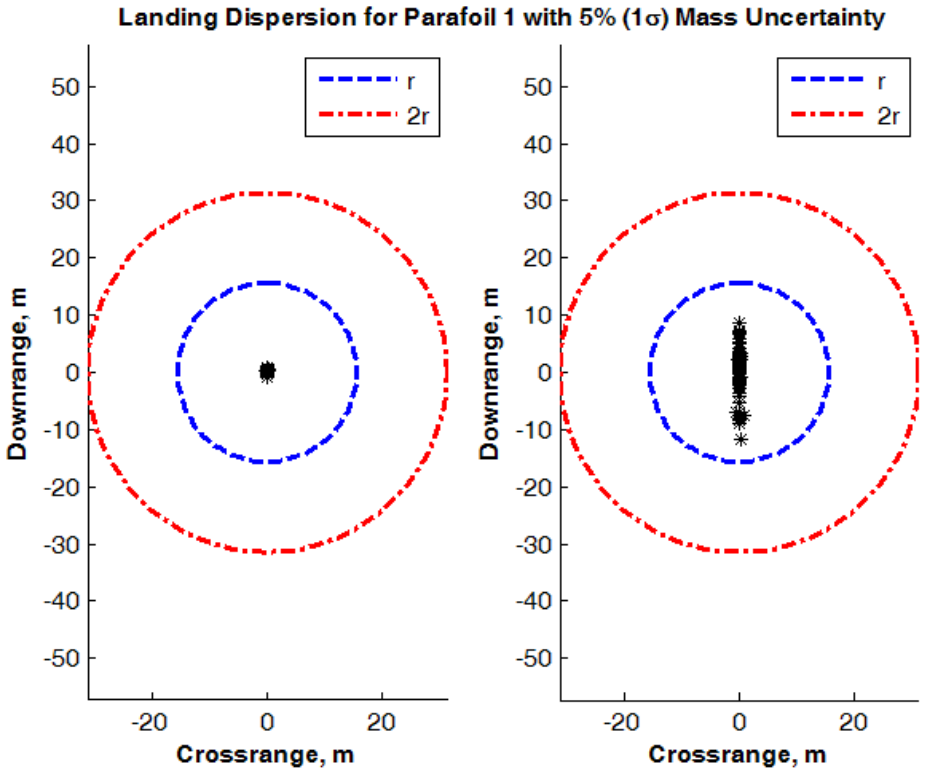

Figure 8.4 Landing dispersion results for Parafoil 1 for the case where the wind profile is perfectly known and the payload mass is varied $\pm 5\%$ (1σ) from the nominal value. Left: System with longitudinal and lateral control. Right: System with lateral control only.

each run are modeled as

$$\begin{aligned} C_L &= C_{L_{\text{nom}}}(1+\delta_1) \\ C_D &= C_{D_{\text{nom}}}(1+\delta_2) \end{aligned} \tag{8.2}$$

where δ_1 and δ_2 are independent zero-mean Gaussian-distributed random variables.

Figures 8.8 and 8.9 show the results of 100 simulated drops of Parafoil 1 and Parafoil 2, respectively, for which δ_1 and δ_2 each have a standard deviation $\sigma = 0.05$. This represents a moderate variation from the expected canopy performance. For Parafoil 1 the average and maximum miss distances are 0.7 and 2.5 m for the system with both longitudinal and lateral control, and 14.6 and 75.2 m for the system with only

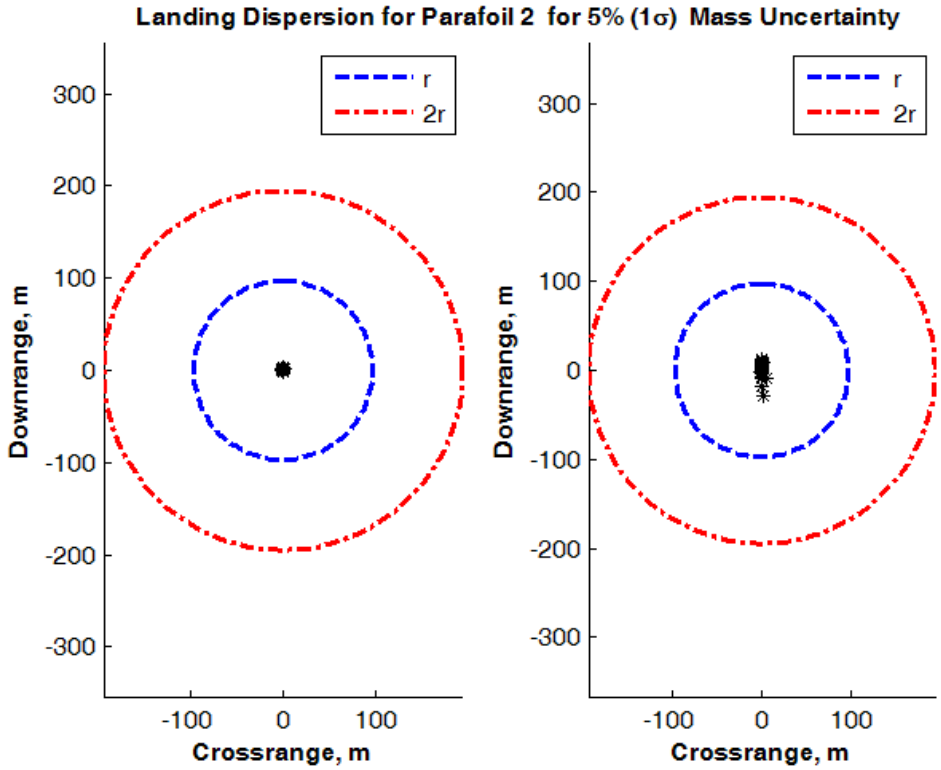

Figure 8.5 Landing dispersion results for Parafoil 2 for the case where the wind profile is perfectly known and the payload mass is varied $\pm 5\%$ (1σ) from the nominal value. Left: System with longitudinal and lateral control. Right: System with lateral control only.

lateral control. For Parafoil 2 the average and maximum miss distances are 4.48 and 44.9 m for the system with both longitudinal and lateral control, and 30.7 and 150.8 m for the system with only lateral control. For both Parafoil 1 and Parafoil 2 we see that the system with both longitudinal and lateral control is able to compensate for the performance variation with all cases landing well within one minimum turn radii. However, system with only lateral control is much more sensitive to variations in canopy performance. In all of the landings occurring outside of one minimum turn radius the ratio L/D is much lower than the expected value. Thus trajectory planning in the early

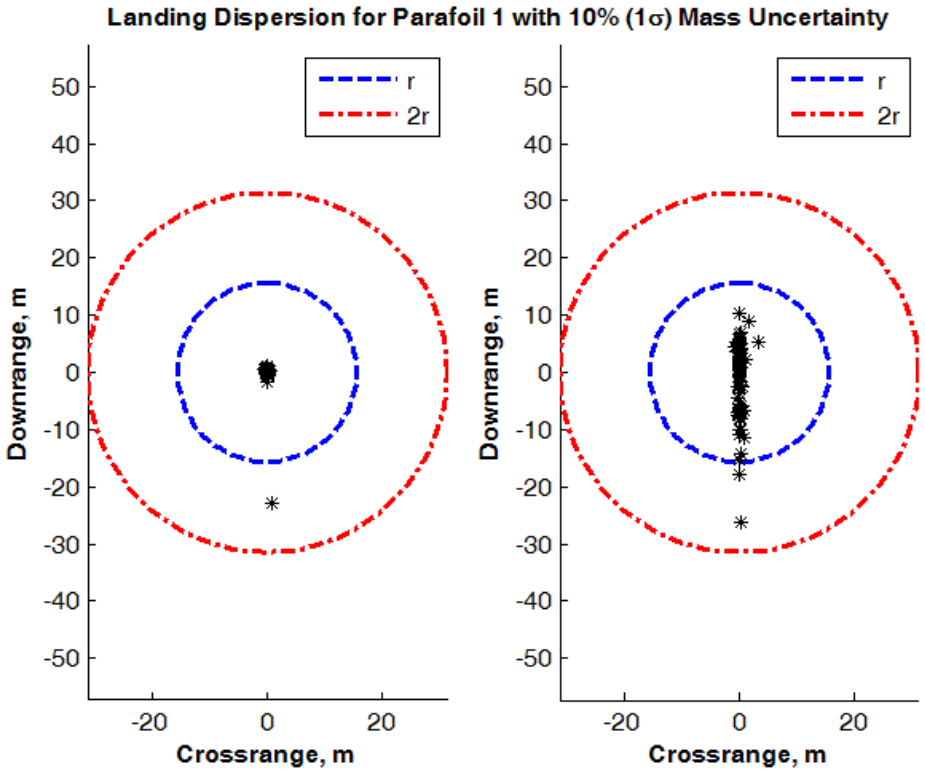

Figure 8.6 Landing dispersion results for Parafoil 1 for the case where the wind profile is perfectly known and the payload mass is varied $\pm 10\%$ (1σ) from the nominal value. Left: System with longitudinal and lateral control. Right: System with lateral control only.

portion of the trajectory assumes the maneuvering energy to be larger than it actually is and at some point along the trajectory the true altitude margin becomes negative and it is no longer possible to reach the target.

Figures 8.10 and 8.11 show the results of 100 simulated drops of Parafoil 1 and Parafoil 2, respectively, for which δ_1 and δ_2 each have a standard deviation $\sigma = 0.10$. This represents a large variation from the expected canopy performance. For Parafoil 1 the average and maximum miss distances are 1.55 and 24.4 m for the system with both longitudinal and lateral control and 28.4 and 276.8 m for the system with only

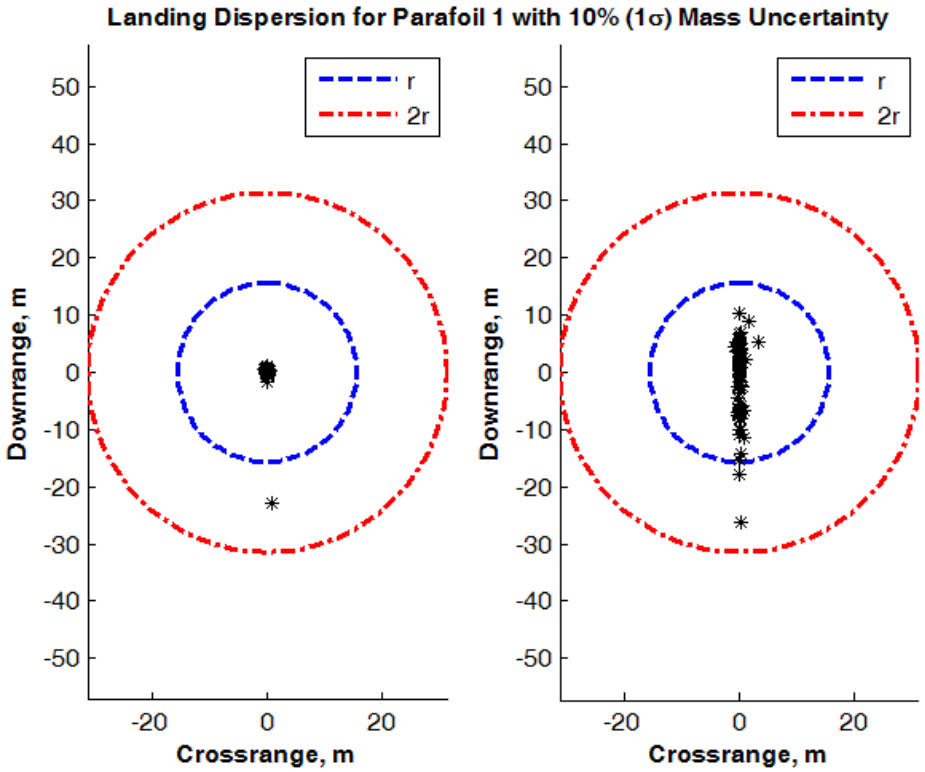

Figure 8.7 Landing dispersion results for Parafoil 2 for the case where the wind profile is perfectly known and the payload mass is varied $\pm 10\%$ (1σ) from the nominal value. Left: System with longitudinal and lateral control. Right: System with lateral control only.

lateral control. For Parafoil 2 the average and maximum miss distances are 8.94 and 61.4 m for the system with both longitudinal and lateral control and 60.8 and 348.9 m for the system with only lateral control. Again, for both Parafoil 1 and Parafoil 2 we see that the system with longitudinal control is able to compensate for the uncertainty in canopy performance. On the other hand, the system with only lateral control sees a dramatic reduction in landing accuracy. However, we see that even with a large degree of uncertainty in the canopy performance, over 90% of the landings still occur within 100 m of the target for both Parafoil 1 and Parafoil 2.

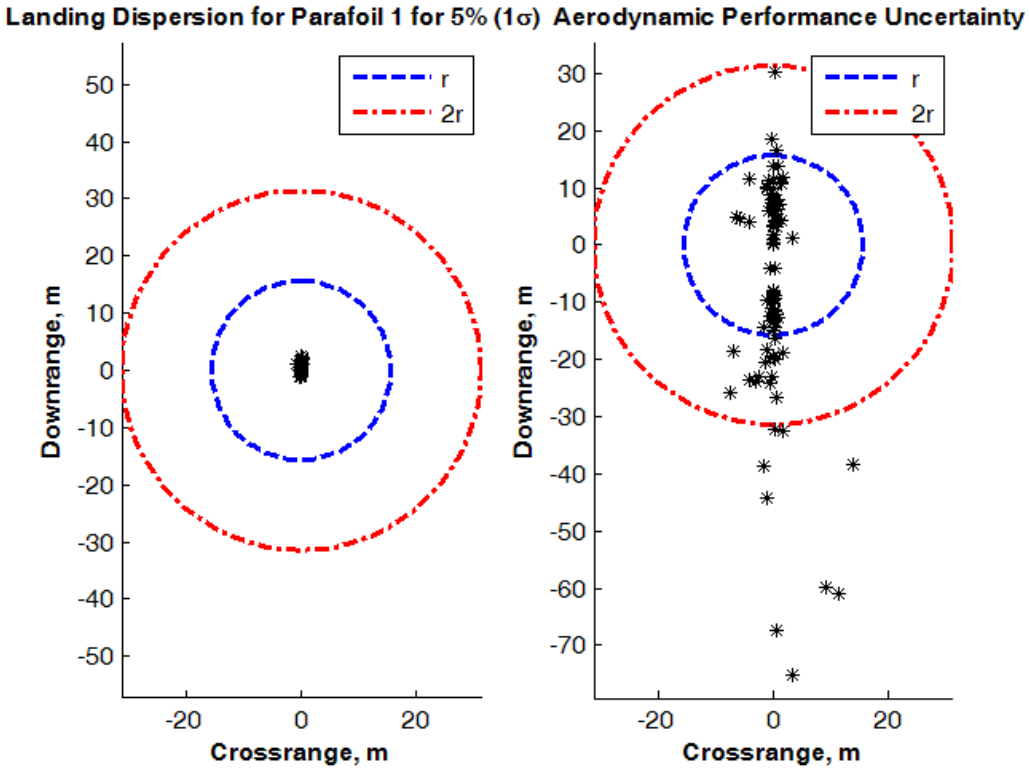

Figure 8.8 Landing dispersion results for Parafoil 1 for the case where the wind profile is perfectly known and the C_L and C_D are varied $\pm 5\%$ (1σ) from the nominal values. Left: System with longitudinal and lateral control. Right: System with lateral control only.

8.5 Sensitivity to Wind Profile Errors

The wind profile has a strong effect on the motion of the parafoil/payload system. In general, the uncertainty in the assumed a priori wind profile will be time-correlated in both magnitude and direction. The azimuth of the perturbation could lie in any direction. In this study we model both the magnitude and direction of the wind field perturbation as a random walk.

Figures 8.12 and 8.13 present the results from 100 simulated drops of Parafoil 1 and Parafoil 2, respectively, for which the random walk realization corresponding to the wind

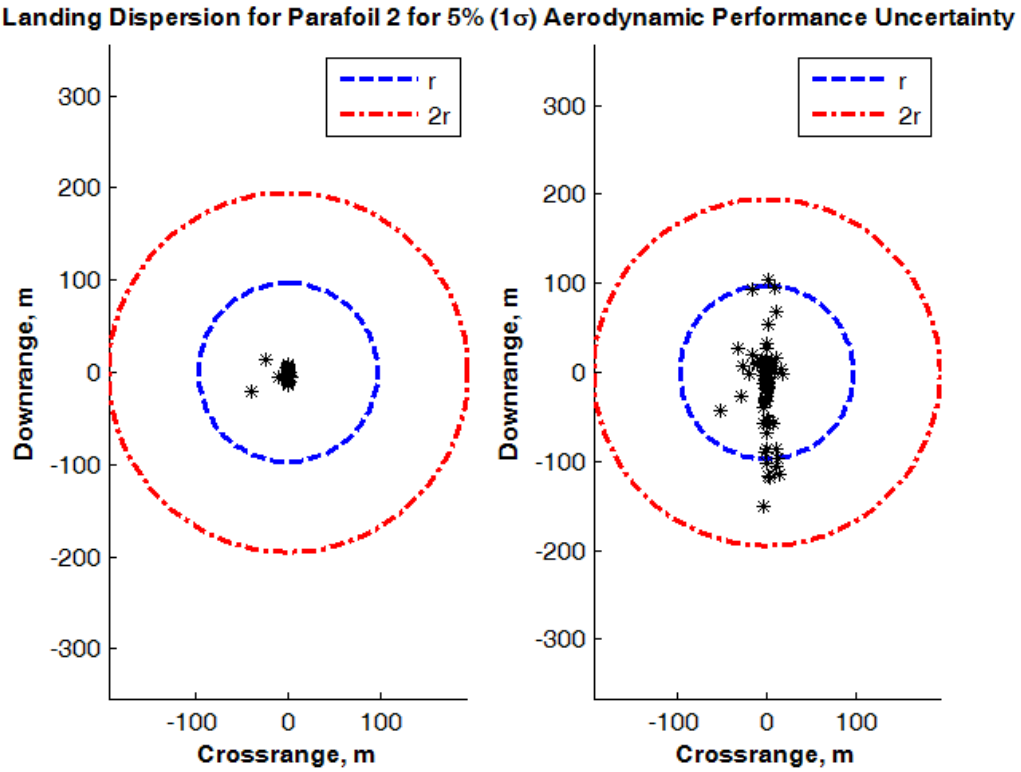

Figure 8.9 Landing dispersion results for Parafoil 2 for the case where the wind profile is perfectly known and the C_L and C_D are varied $\pm 5\%$ (1σ) from the nominal values. Left: System with longitudinal and lateral control. Right: System with lateral control only.

velocity perturbation is bounded such that

$$|\tilde{\mathbf{W}}(\tau)| \leq 0.2V_0 \tag{8.3}$$

for both Parafoil 1 and Parafoil 2. For Parafoil 1, the average and maximum miss distances are 0.88 and 3.45 m for the system with both longitudinal and lateral control, and 8.0 and 51.5 m for the system with only lateral control. For Parafoil 2, the average and maximum miss distances are 5.79 and 104.2 m for the system with both longitudinal and lateral control and 27.2 and 645.9 for the system with only lateral control. We see that for both Parafoil 1 and Parafoil 2 that the system with longitudinal and lateral

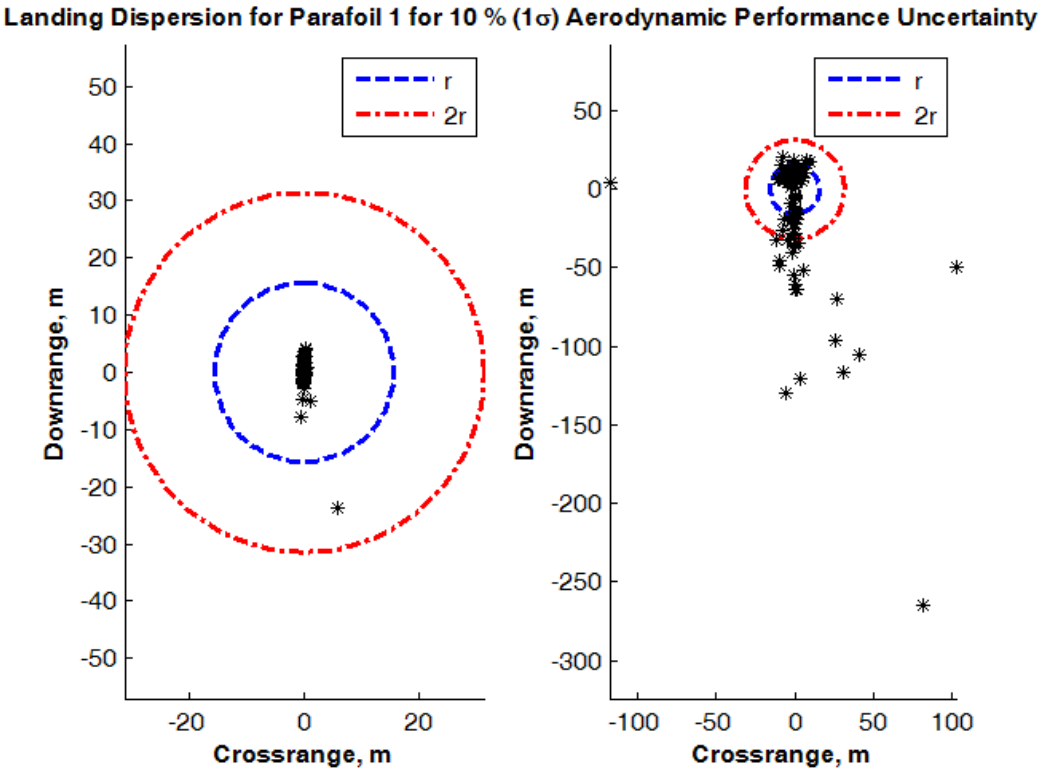

Figure 8.10 Landing dispersion results for Parafoil 1 for the case where the wind profile is perfectly known and the C_L and C_D are varied $\pm 10\%$ (1σ) from the nominal values. Left: System with longitudinal and lateral control. Right: System with lateral control only.

control is able to compensate for the wind uncertainty. For Parafoil 1 all of the cases land within one minimum turn radius, and for Parafoil 2 all but one case lands within one minimum turn radius.

On the other hand, the system with only lateral control is more sensitive to errors in the a priori wind profile. For Parafoil 1 we have 10 cases landing outside of one minimum turn radius, 4 of which are outside of two minimum turn radii. The larger landing dispersion is due primarily to errors in estimating position in the wind fixed coordinate frame early in the trajectory eventually causing the true altitude margin

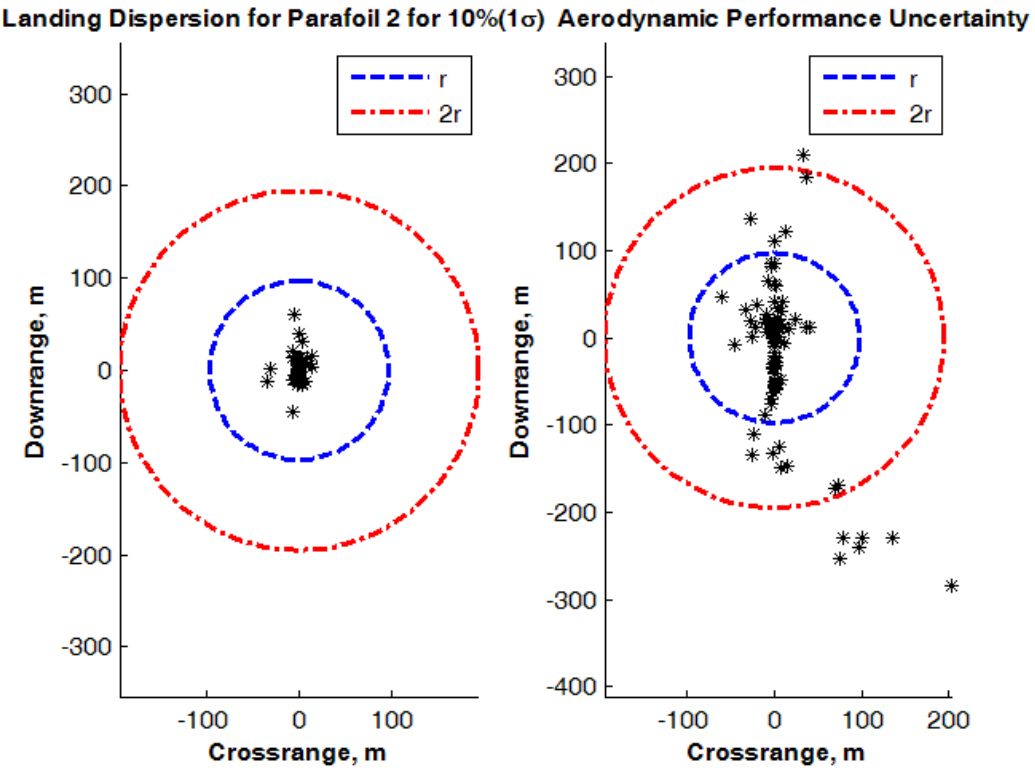

Figure 8.11 Landing dispersion results for Parafoil 2 for the case where the wind profile is perfectly known and the C_L and C_D are varied $\pm 10\%$ (1σ) from the nominal values. Left: System with longitudinal and lateral control. Right: System with lateral control only.

(based off the actual wind profile) to go negative and the inability to decrease the along-track trajectory error later in the trajectory.

Figures 8.14 and 8.15 present the results from 100 simulated drops of Parafoil 1 and Parafoil 2, respectively, for which the random walk realization corresponding to the wind velocity perturbation is bounded such that

$$|\tilde{\mathbf{W}}(\tau)| \leq 0.4 V_0 \tag{8.4}$$

which represents a large variation of the expected wind velocity compared to the vehicle airspeed. For Parafoil 1 the average and maximum miss distances are 1.97 and 14.7

m for the system with both longitudinal and lateral control and 24.1 and 187.0 m for the system with only lateral control. For Parafoil 2 the average and maximum miss distances are 12.3 and 475.8 m for the system with both longitudinal and lateral control and 53.6 and 495.6 m for the system with only lateral control. Again, for both Parafoil 1 and Parafoil 2 the system with longitudinal control is able to overcome the wind profile variation and have at least 99% of cases land within one minimum turn radii. The system with only lateral control does still achieve 80% of landings within two minimum turn radii, however it is apparent that lower wing loadings should be avoided when longitudinal control is not available.

8.6 Performance With All Dispersions

Figure 8.16 presents the results from 100 simulated drops for Parafoil 1 with all dispersions active including sensor noise, mass, C_L and C_D, and wind uncertainty all as described above. The average and maximum miss distances are 2.0 and 5.8 m for the system with both longitudinal and lateral control, and 18.8 and 206 m for the system with only lateral control. The system with longitudinal control again has all of the cases landing within the minimum turn radius circle. This shows that overall the system with longitudinal control is robust to sensor noise, parameter uncertainty, and wind variation. The system with only lateral control has 30 cases landing outside the minimum turn radius circle and 17 cases landing outside the two turn radii circle. As with previous cases, uncertainty in system parameters and the a priori wind profile lead to errors in estimating position in the wind fixed coordinate frame which couple with the inability to reduce along-track error lead to a larger landing dispersion.

Figure 8.17 presents the results from 100 simulated drops for Parafoil 2 with all dispersions active including sensor noise, mass, C_L and C_D, and wind uncertainty all as described above. The average and maximum miss distances are 12.5 and 351 m for the

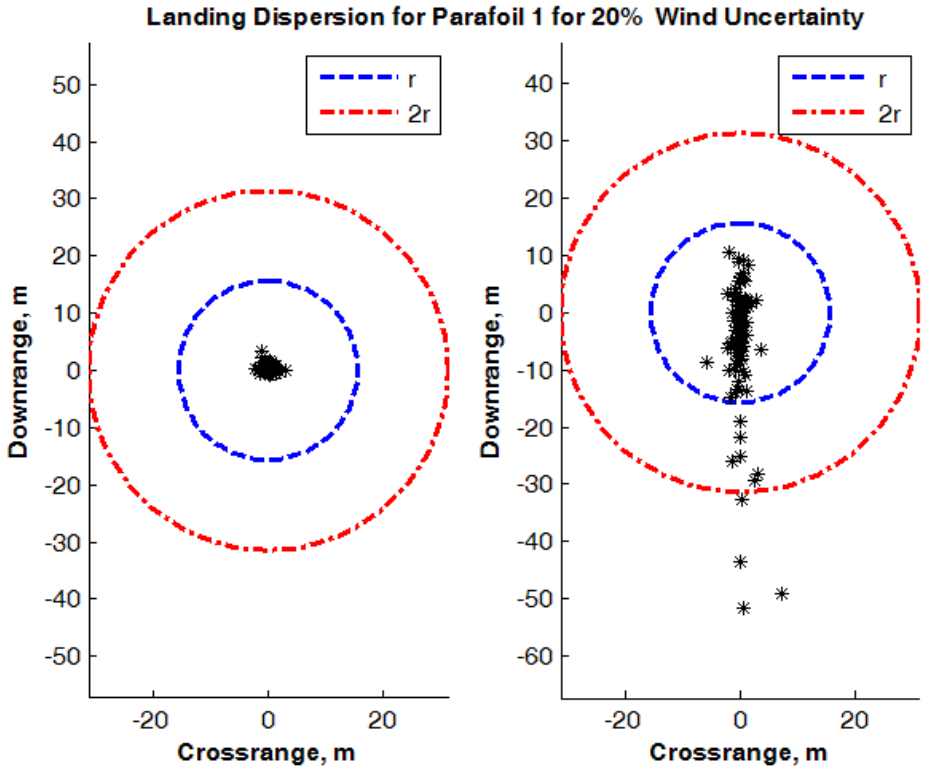

Figure 8.12 Landing dispersion results for Parafoil 1 for the case where there wind profile magnitude is in error by 20% of the nominal vehicle airspeed and the direction varies from 0 to 360°. Left: System with longitudinal and lateral control. Right: System with lateral control only.

system with both longitudinal and lateral control, and 51.1 and 557 m for the system with only lateral control. As with the smaller parafoil we see that the system with longitudinal control is largely robust to uncertainty in parameters and the wind profile. There are 2 cases that land outside the minimum turn radius circle and 1 outside of the two turn radii circle. These are cases where the wind uncertainty is largely biased along the negative x-axis and the canopy performance is significantly less than expected. The system with lateral control only has 10 cases outside the minimum turn radius circle and 2 outside of the two turn radii circle. As compared to the results for Parafoil 1,

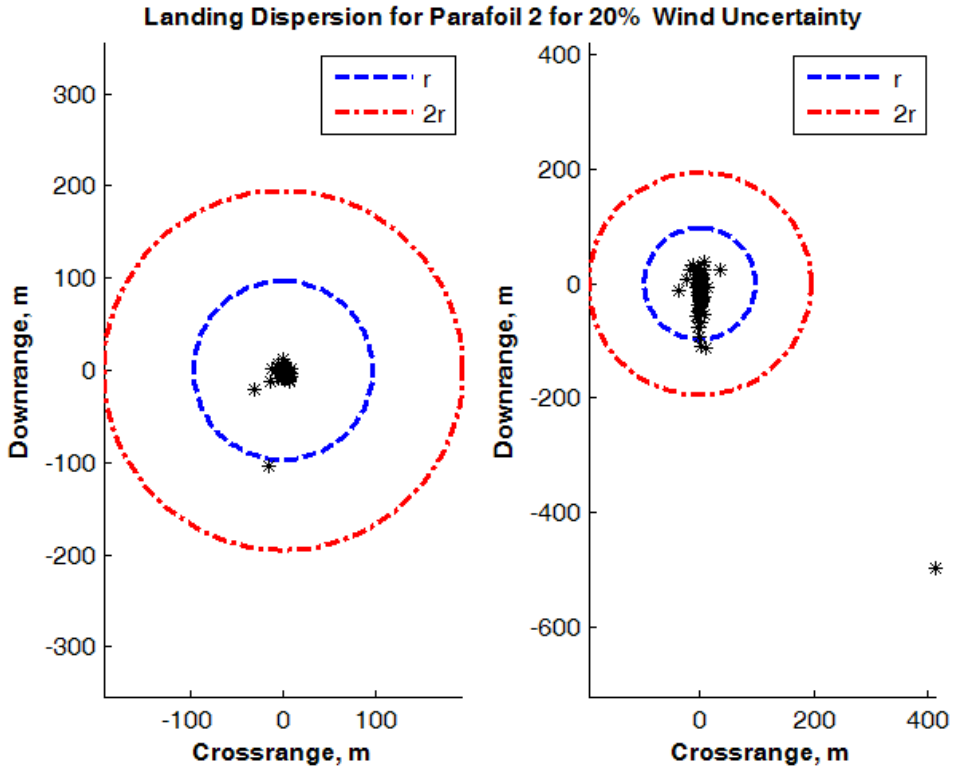

Figure 8.13 Landing dispersion results for Parafoil 2 for the case where there wind profile magnitude is in error by 20% of the nominal vehicle airspeed and the direction varies from 0 to 360°. Left: System with longitudinal and lateral control. Right: System with lateral control only.

we see that Parafoil 2 generally has a smaller landing dispersion pattern compared to its minimum turn radius for both cases with and without longitudinal control. This is largely due to the larger nominal airspeed for Parafoil 2 that reduces errors in estimating position in the wind fixed coordinate and decreases sensitivity to unknown variations in the wind.

Perturbation	**Parafoil 1** Lat. Control (avg/max)	**Parafoil 1** Lat.+Lon. Control (avg/max)	**Parafoil 2** Lat. Control (avg/max)	**Parafoil 2** Lat.+Lon. Control (avg/max)
Sensor Noise	2.2/10.4m	1.8/4.5m	6.42/19.6m	5.24/11.5m
5% Mass	2.60/11.8m	0.34/0.90m	5.49/28.0m	1.04/3.31m
10% Mass	4.3/26.2m	0.6/22.9m	7.69/109m	1.52/7.81m
5% C_L and C_D	14.6/75.2m	0.7/2.5m	30.7/151m	4.48/44.9m
10% C_L and C_D	28.4/276m	1.55/24.4m	60.8/349m	8.94/61.4m
20% Wind	8.0/51.5m	0.88/3.45m	27.2/646	5.79/104m
40% Wind	24.1/187m	1.97/14.7m	53.6/496m	12.3/476m
All	18.8/206m	2.0/5.8m	51.1/557m	12.5/351

Table 8.4 Summary of simulation results for Parafoil 1 and Parafoil 2. The case listed as "All" includes sensor noise, 5% variation of payload mass, 5% variation of C_L and C_D, and 20% variation in wind.

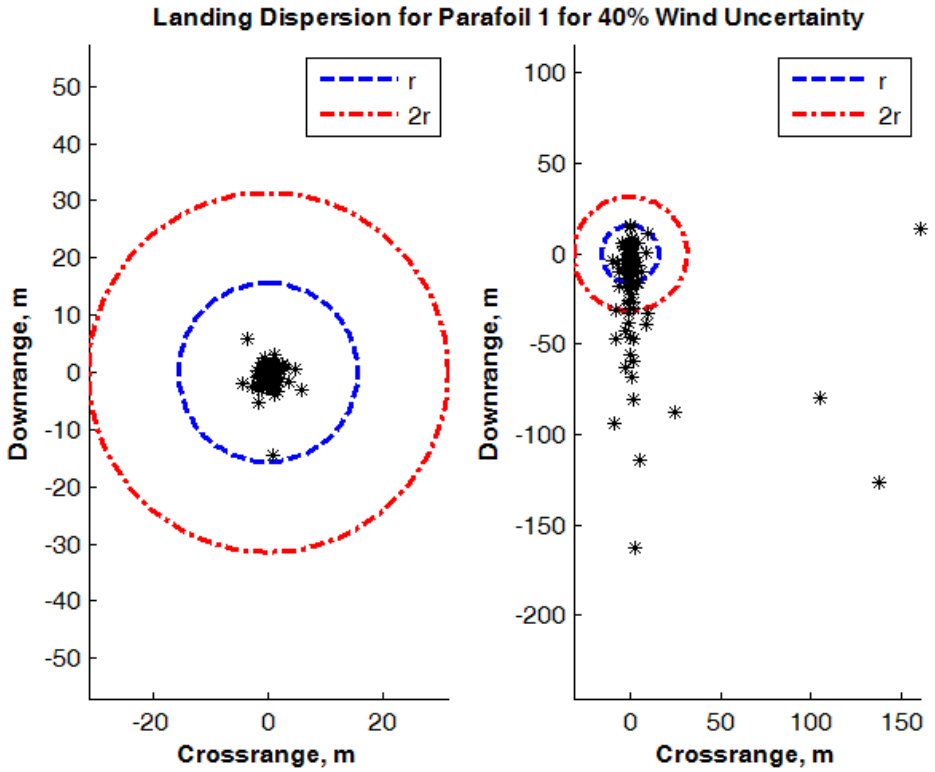

Figure 8.14 Landing dispersion results for Parafoil 1 for the case where there wind profile magnitude is in error by 40% of the nominal vehicle airspeed and the direction varies from 0 to 360°. Left: System with longitudinal and lateral control. Right: System with lateral control only.

8.7 Performance with Wind Estimation

In Chapter 5 we developed filters for estimating the local wind speed components. In this section we will consider one potential method of using this information to improve the landing accuracy. The results from the preceding sections indicate that when longitudinal control is available the landing dispersion is largely unchanged in the presence of even significant variations of the true wind field from the expected a priori wind field. In this study we shall only consider applying the measured data to improving the landing dispersion for systems with lateral control only.

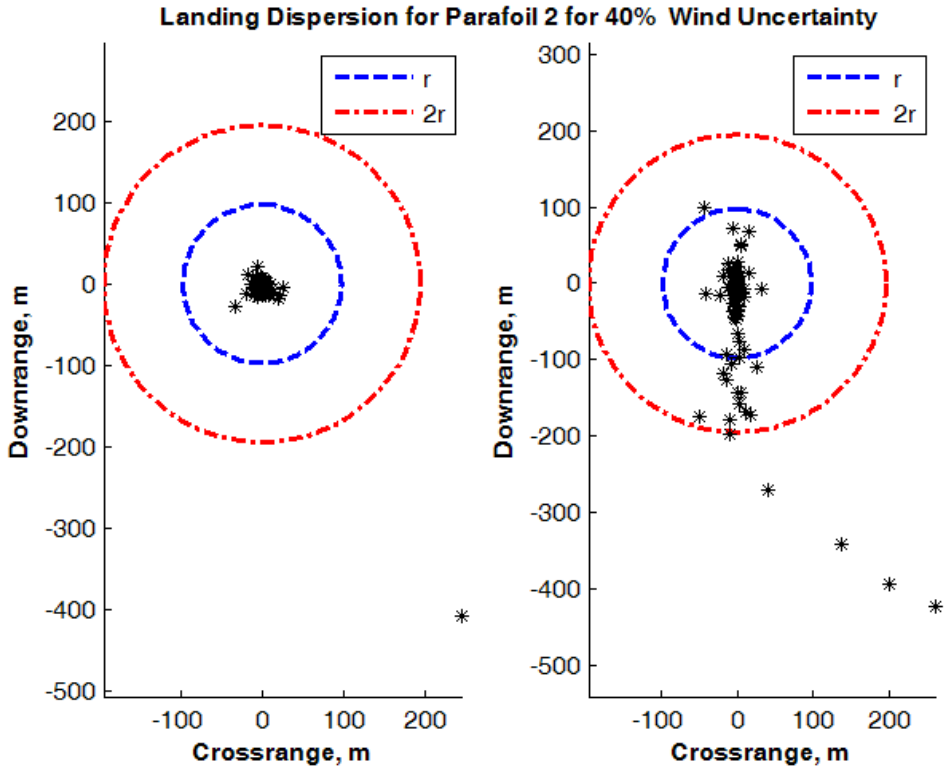

Figure 8.15 Landing dispersion results for Parafoil 2 for the case where there wind profile magnitude is in error by 40% of the nominal vehicle airspeed and the direction varies from 0 to 360°. Left: System with longitudinal and lateral control. Right: System with lateral control only.

In the most general case, the variation of the true wind profile from the expected a priori wind profile can have any magnitude and may be in any direction. In Chapter 3 we showed that the perturbation could be written as a function of altitude or time only. In this study, we assume that the perturbation is given by a bounded random process which is correlated in time. In general it is difficult to predict the value of the perturbation at some future time based on knowledge of the value of the perturbation at the current time. Our approach here is to assume that the perturbation remains constant at the current filtered value for the remainder of the flight.

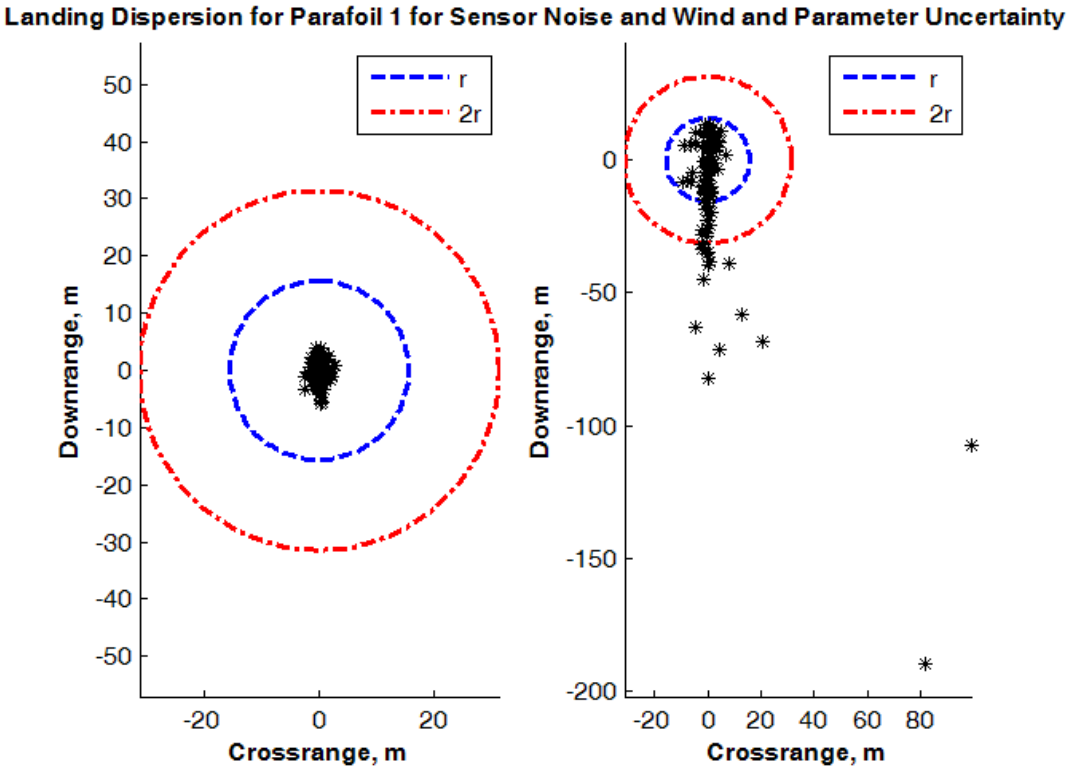

Figure 8.16 Landing dispersion results for Parafoil 1 for the case including navigation errors, wind uncertainty, and variations in aerodynamic performance and payload mass. Left: System with longitudinal and lateral control. Right: System with lateral control only.

Figure 8.18 shows the results of 50 simulated drops of Parafoil 2 for which the wind profile perturbation (the true value of which is unknown to the guidance and control) is constant. The left plot shows cases where the magnitude is uniformly distributed between 0 and 4 m/s and the direction is uniformly distributed between 0 and 2π. The right plot shows cases where the magnitude is uniformly distributed between 0 and 8 m/s. The average and maximum miss distances are 8.10 and 34.4 m for the first case and 5.74 and 27.4 m for the second case. We see that when the wind perturbation is constant (i.e. matches the assumed perturbation) that wind estimation can significantly

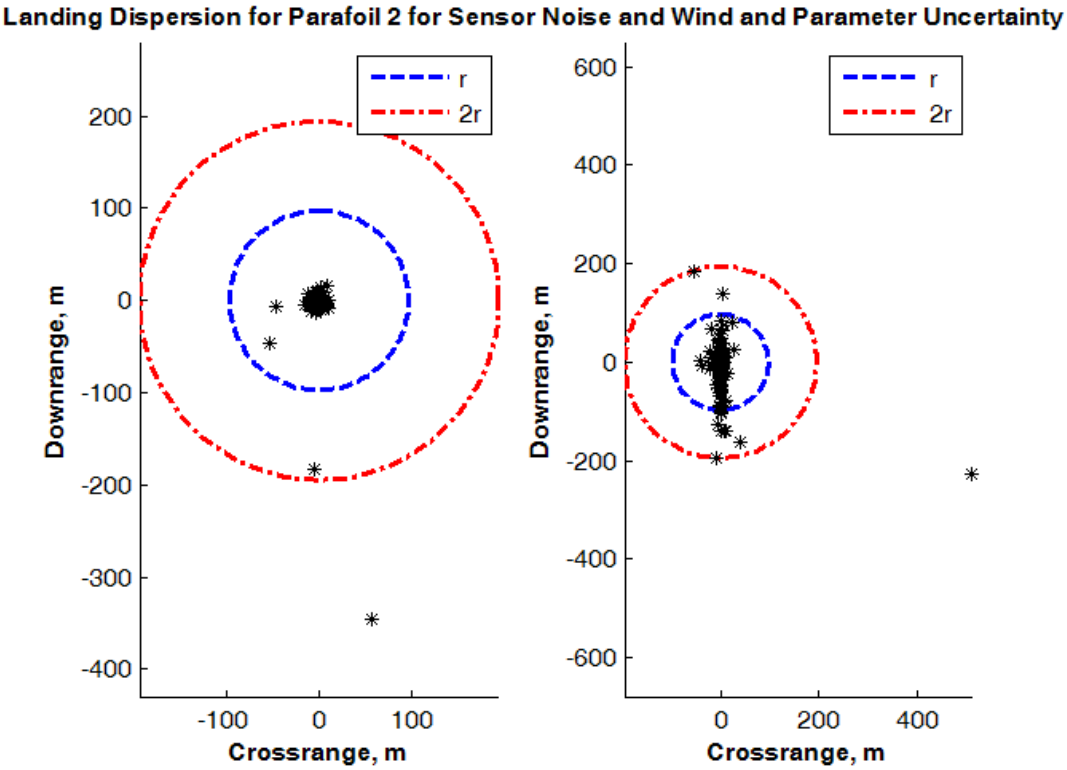

Figure 8.17 Landing dispersion results for Parafoil 2 for the case including navigation errors, wind uncertainty, and variations in aerodynamic performance and payload mass. Left: System with longitudinal and lateral control. Right: System with lateral control only.

reduce the landing dispersion (compare Figure 8.18 to the right side plots of Figures 8.13 and 8.15).

For the remaining cases we will model the magnitude and direction of the wind field perturbation as a bounded first-order Markov process. The process is given by

$$\tilde{x}_{k+1} = 0.999x_k + \delta \tag{8.5}$$

where δ is a zero mean Gaussian distributed random variable with a standard deviation $\sigma = 0.1$. The bound is enforced by generating a realization of the process and scaling it so that the maximum value is equal to the bound. The direction variation is centered

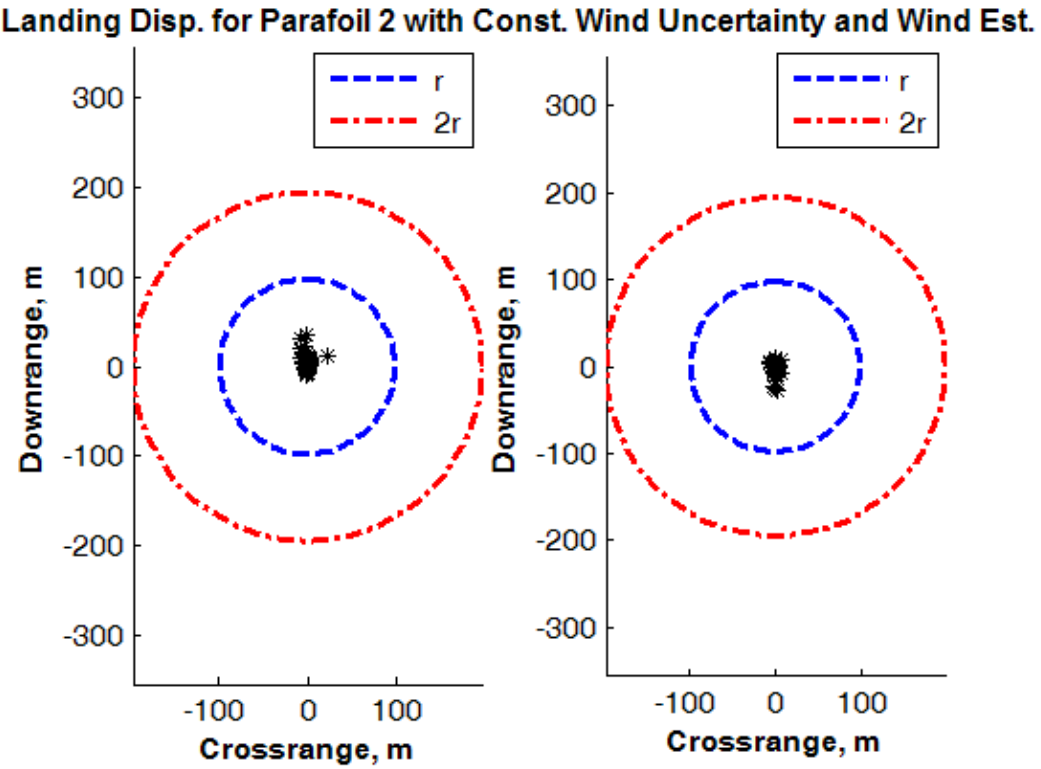

Figure 8.18 Landing dispersion results for Parafoil 2 with wind estimation for the case where the wind perturbation is constant. Left: wind error magnitude is uniformly distributed on [0,4] m/s, Right: wind error magnitude is uniformly distributed on [0,8] m/s.

on a random azimuth which is uniformly distributed from 0 to 2π.

Figure 8.19 presents the results from 50 simulated drops of Parafoil 2 for which the wind direction perturbation is bounded to be less than 15 degrees. The left plot shows cases where the velocity perturbation is bounded to be less than 4 m/s and the right plot shows cases where the bound is 8 m/s. The average and maximum miss distances are 13.6 and 175 m for the first case and 28.5 and 211 m for the second case. As compared to the case with a constant wind field perturbation we see that even a small directional variance begins to degrade the landing accuracy.

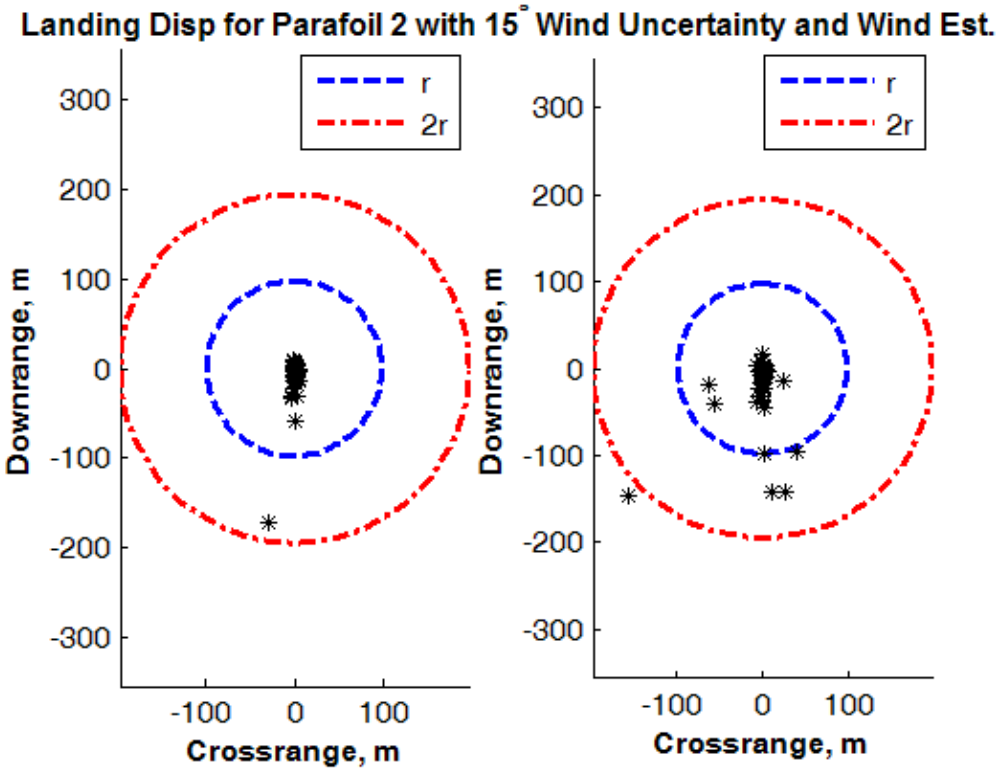

Figure 8.19 Landing dispersion results for Parafoil 2 with wind estimation for the case where the direction of the wind perturbation is limited to be within a 15° window. Left: wind error magnitude is a first-order Markov process bounded by [0,4] m/s, Right: bounded by [0,8] m/s.

Figure 8.20 presents the results from 50 simulated drops of Parafoil 2 for which the wind direction perturbation is bounded to be less than 30 degrees. The left plot shows cases where the velocity perturbation is bounded to be less than 4 m/s and the right plot shows cases where the bound is 8 m/s. The average and maximum miss distances are 16.5 and 216 for the first case and 42.9 and 406 m for the second case. Again we not that an increase in the allowed directional variation of the wind perturbation has a negative effect on landing accuracy.

Figure 8.21 presents the results from 50 simulated drops of Parafoil 2 for which the

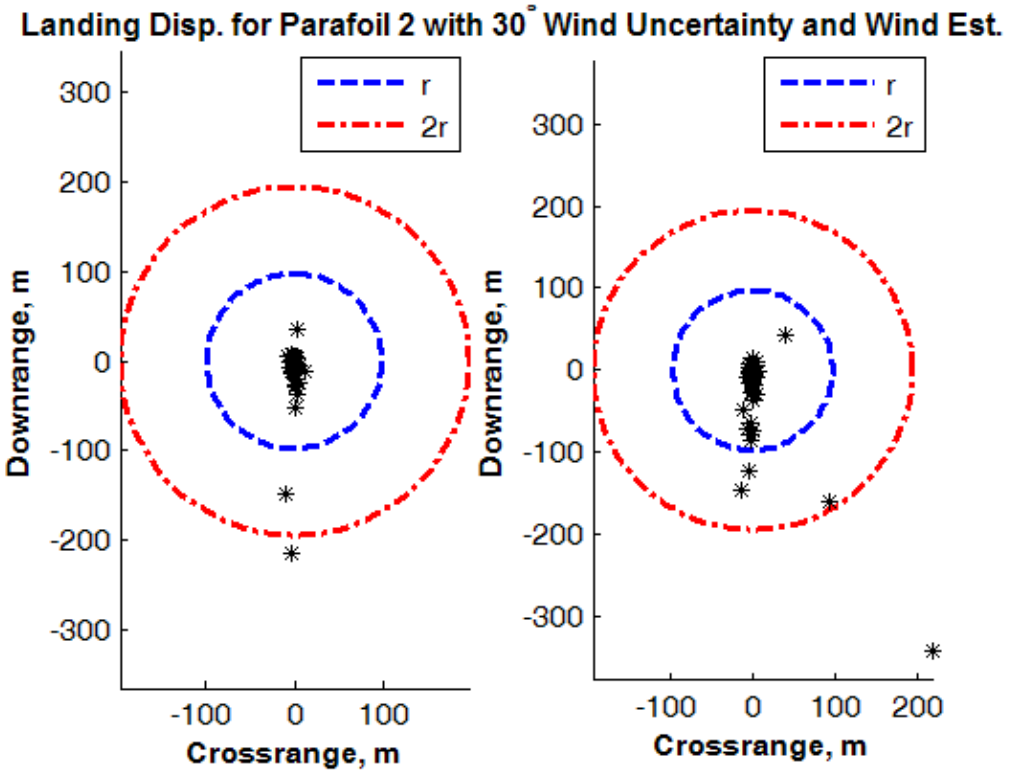

Figure 8.20 Landing dispersion results for Parafoil 2 with wind estimation for the case where the direction of the wind perturbation is limited to be within a 30° window. Left: wind error magnitude is a first-order Markov process bounded by [0,4] m/s, Right: bounded by [0,8] m/s.

wind direction perturbation is bounded to be less than 60 degrees. The left plot shows cases where the velocity perturbation is bounded to be less than 4 m/s and the right plot shows cases where the bound is 8 m/s. The average and maximum miss distances are 26.6 and 438 for the first case and 312 and 1598 m for the second case. For this case we see that with a maximum wind speed variation of 4 m/s most cases land within one minimum turn radius. However when the maximum wind speed variation is increased to 8 m/s there is a dramatic reduction in landing performance with many cases landing well outside of two minimum turn radii. Increasing the bounds on the directional variation

Directional Variation	4 m/s Speed Variation (Avg/Max)	8 m/s Speed Variation (Avg/Max)
Constnt	8.10/34.4 m	5.74/27.4 m
15 deg	13.6/175 m	28.5/211 m
30 deg	16.5/216 m	42.9/406 m
60 deg	26.6/438 m	312/1598 m

Table 8.5 Summary of simulation results for Parafoil 2 using on-board wind estimation in an attempt to improve landing accuracy in the presence of unknown wind field variation.

above 60 degrees further increases the landing dispersion. Recall, we mentioned that it is difficult or impossible to infer or predict the wind perturbation at future altitudes based on measurements of the perturbation at the current altitude. Since no other information is available, this led to the assumption that the wind perturbation remains constant from the current altitude to the ground. For small directional variation we do see improvement in landing accuracy by using wind estimation. However, as the directional variability increases we actually see a degradation in performance (compare the right plots of Figures 8.21 and 8.15). Thus, the application of wind estimation may have limited practical use when the expected wind field perturbation from the a priori wind profile is large. A summary of the results of simulations using wind estimation is given in Table 8.7.

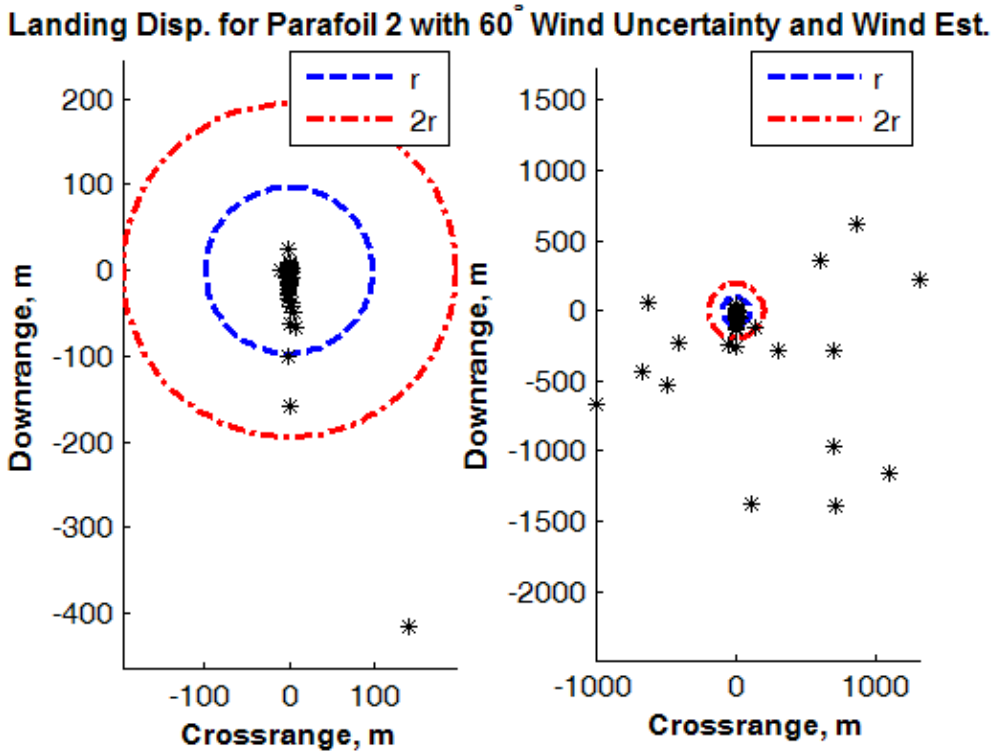

Figure 8.21 Landing dispersion results for Parafoil 2 with wind estimation for the case where the direction of the wind perturbation is limited to be within a 60° window. Left: wind error magnitude is a first-order Markov process bounded by [0,4] m/s, Right: bounded by [0,8] m/s.

CHAPTER 9. CONCLUSION

This dissertation presents an advanced guidance algorithm for a broad class of autonomous parafoils that encompass gross variations in the lift to drag ratio, wing loading, and maximum turn rate. The foundation of the algorithm is a fixed-time trajectory planner which generates one of two types of trajectories, both with a fixed final heading, based on the position relative to the target and known information on the wind profile and parafoil canopy performance. The planning algorithm utilizes a low-fidelity model which requires only three parameters that adequately summarize the behavior of the system and are readily available for a given canopy and payload weight. In this way the guidance is fully parameterized on known information about the system and is readily adapted to different canopies and/or payloads.

The algorithm was demonstrated for two different classes of parafoil systems, one a typical small- to mid-scale canopy with light loading, and the other a typical large-scale system with high loading. Cases were run for both systems using lateral control only and lateral plus longitudinal control. It was shown that the system with longitudinal control was robust to variations from expected system parameters and wind profile uncertainty. It was also shown that systems with lateral control only are more sensitive to both wind profile and parameter uncertainty, with the strongest sensitivity being to uncertainty in the system lift to drag ratio (L/D) and wind profile uncertainty.

9.1 Contributions of this Study

The key contributions of this work to the area of parafoil GNC are

- We show in Chapter 3 that with simple assumptions the motion of a parafoil can be described by a simple three state kinematic model. This model is widely used in the robotics community for path planning. The model also lends itself to the use of geometric methods for guidance and control.

- The reduced order model used for trajectory planning incorporates the change in airspeed and glide path angle that occur in a turn whereas current parafoil GNC algorithms assume the sink rate is constant.

- Using the reduced order model, the trajectory planning problem was cast as a two-dimensional fixed-time problem, in contrast to a three-dimensional free final time problem.

- The guidance algorithm incorporates the user-supplied maximum turn rate to ensure the generated reference trajectories are kinematically feasible.

- The guidance algorithm places no constraint on the maximum wind speed. The algorithm can handle cases where the wind speed exceeds the vehicle airspeed so that the system cannot make forward progress with respect to the ground.

- The altitude margin defined in Chapter 3 can be used to determine if the target is reachable and give a quantitative measure of the amount of excess energy that needs to be dissipated.

- It was shown that using simple measurements that the local wind field could be measured on-board the parafoil system.

9.2 Recommendations for Future Work

In the present study, the use of modified Dubins paths restricts the trajectory to have all turns performed using the same turn radius. Allowing the turns to have different radii may be one way to overcome the non-existence of fixed-time paths with a given fixed time in some instances.

Another concept that should be considered is changing the trim value of L/D between a few discrete levels as needed during the flight. In the present study the value of L/D used for planning remains fixed. Allowing this value to change would provide an intermediate capability between systems with both longitudinal and lateral control and those with only lateral control. This may also help overcome the non-existence of fixed-time paths for certain values of the fixed final time, and also give the ability to increase or decrease the altitude margin in-flight.

Finally, though we have shown in the present study that the wind profile can be measured reasonably well at the current altitude of the system, it is difficult or impossible to infer what the perturbation from the a priori assumed profile will be for the remaining portion of the trajectory. Therefore it is unclear how best to use the on-board wind estimation to improve landing accuracy.

APPENDIX A. THE CONTINUOUS-DISCRETE KALMAN FILTER

In this appendix we present the equations for the continuous-discrete linear Kalman filter. The continuous-discrete formulation of the filter is used to filter a continuous-time process using discrete measurements. We shall follow the development in Ref. (47).

Consider the continuous-time system of linear differential equations given by

$$\dot{\mathbf{x}} = \mathbf{F}\mathbf{x} + \mathbf{w} \tag{A.1}$$

where $\mathbf{x}$ is the $n \times 1$ state vector, $\mathbf{F}$ is the $n \times n$ system dynamics matrix, and $\mathbf{w}$ is an $n \times 1$ process noise vector. The covariance of the process noise vector is given by

$$\mathbf{Q} = E[\mathbf{w}\mathbf{w}^T] \tag{A.2}$$

The measurements are defined as a linear combination of the states given by the equation

$$\mathbf{z} = \mathbf{H}\mathbf{x} + \mathbf{v} \tag{A.3}$$

where $\mathbf{z}$ is the $p \times 1$ measurement vector, $\mathbf{H}$ is the $p \times n$ measurement matrix, and $\mathbf{v}$ is a $p \times 1$ measurement noise vector. The covariance of the measurement noise vector is given by

$$\mathbf{R} = E[\mathbf{v}\mathbf{v}^T] \tag{A.4}$$

In practice the measurements are available at discrete instants in time, thus the preceding equations must be discretized before implementing the filter. The sample

time shall be denoted by T. The discretization will require the fundamental matrix corresponding to the system dynamics and is defined as

$$\mathbf{\Phi}(t) = \mathcal{L}^{-1}[(s\mathbf{I} - \mathbf{F})^{-1}] \tag{A.5}$$

where $\mathbf{I}$ is the identity matrix and $\mathcal{L}^{-1}$ is the inverse Laplace transform. The fundamental matrix can also be found by expanding the matrix exponential $e^{(F)t}$ in a Taylor series

$$\mathbf{\Phi}(t) = \mathbf{I} + \mathbf{F}t + \frac{(\mathbf{F}t)^2}{2!} + \cdots + \frac{(\mathbf{F}t)^n}{n!} + \cdots \tag{A.6}$$

Once the fundamental matrix is known, the discrete-time state transition matrix can be found by evaluating the fundamental matrix at the sampling time T

$$\mathbf{\Phi}_k = \mathbf{\Phi}(T) \tag{A.7}$$

The discrete-time measurement equation at the k^{th} iteration is

$$\mathbf{z}_k = \mathbf{H}\mathbf{x}_k + \mathbf{v}_k \tag{A.8}$$

and the k^{th} measurement covariance matrix is

$$\mathbf{R}_k = E[\mathbf{v}_k\mathbf{v}_k^T] \tag{A.9}$$

The filter update equation is given by

$$\hat{\mathbf{x}}_k = \mathbf{\Phi}_k\hat{\mathbf{x}}_{k-1} + \mathbf{K}_k(\mathbf{z}_k - \mathbf{H}\mathbf{\Phi}_k\hat{\mathbf{x}}_{k-1}) \tag{A.10}$$

where $\hat{\mathbf{x}}$ is the state estimate and $\mathbf{K}_k$ is the Kalman gain. The Kalman gain is computed from the matrix Ricatti equations given by

$$\mathbf{M}_k = \mathbf{\Phi}_k\mathbf{P}_{k-1}\mathbf{\Phi}_k^T + \mathbf{Q}_k \tag{A.11}$$

$$\mathbf{K}_k = \mathbf{M}_k\mathbf{H}^T(\mathbf{H}\mathbf{M}_k\mathbf{H}^T + \mathbf{R}_k)^{-1} \tag{A.12}$$

$$\mathbf{P}_k = (\mathbf{I} - \mathbf{K}_k\mathbf{H})\mathbf{M}_k \tag{A.13}$$

Here, $\mathbf{M}_k$ is the covariance of the state estimation error prior to the update, $\mathbf{P}_k$ is the covariance of the state estimation error after the measurement update, and $\mathbf{Q}_k$ is the discrete process noise matrix computed by

$$\mathbf{Q}_k = \int_0^T \mathbf{\Phi}^T(\tau)\mathbf{Q}\mathbf{\Phi}(\tau)d\tau \tag{A.14}$$

APPENDIX B. PROCESS MODELS FOR TRACKING

In this appendix we will present three general process models for tracking applications. The models are known as the White Noise Velocity (WNV) model, the White Noise Acceleration (WNA) model, and the Wiener Process Acceleration (WPA) model (47; 48). We will present the system dynamics matrix, state transition matrix, and process noise matrix for each.

These models are derived by setting a specified derivative of the state equal to zero, or equivalently, by assuming that the signal behaves as a polynomial in time of a certain order.

White Noise Velocity Model

Let x be the process we are interested in measuring. The White Noise Velocity model assumes the process is given by

$$x = a_0 \tag{B.1}$$

where a_0 is a random constant. To allow for the possibility that a_0 varies slowly with time and to speed up convergence we model the process as

$$\dot{x} = v \tag{B.2}$$

where v is a zero-mean, Gaussian distributed random variable, i.e. the 'velocity' of the process is white noise. The state vector is given by

$$\mathbf{x} = x \tag{B.3}$$

and the system dynamics matrix is given by

$$\mathbf{F} = 0 \tag{B.4}$$

Using A.6 the discrete fundamental matrix is given by

$$\mathbf{\Phi}_k = 1 \tag{B.5}$$

The continuous-time process covariance is given by

$$\mathbf{Q} = \Phi_s \tag{B.6}$$

and using A.14 the discrete process covariance is

$$\mathbf{Q}_k = \Phi_s T \tag{B.7}$$

Finally, the measurement and measurement covariance matrices are given by

$$\mathbf{H} = 1 \tag{B.8}$$

$$\mathbf{R}_k = \sigma_n^2 \tag{B.9}$$

where σ_n^2 is the variance of the measurement noise.

White Noise Acceleration Model

The White Noise Acceleration model assumes the process is given by

$$x = a_0 + a_1 t \tag{B.10}$$

where a_0 and a_1 are random constants so that the process is a random ramp. To allow for the possibility that the slope varies slowly with time and to speed up filter convergence we model the process as

$$\dot{x} = a_1 \tag{B.11}$$

$$\ddot{x} = v \tag{B.12}$$

where v is a zero-mean Gaussian distributed variable, i.e. the 'acceleration' of the process is white noise. The state vector is given by

$$\mathbf{x} = \begin{bmatrix} x \\ \dot{x} \end{bmatrix} \tag{B.13}$$

and the system dynamics matrix is given by

$$\mathbf{F} = \begin{bmatrix} 0 & 1 \\ 0 & 0 \end{bmatrix} \tag{B.14}$$

Using Eq. A.6 the discrete fundamental matrix is given by

$$\mathbf{\Phi}_k = \begin{bmatrix} 1 & T \\ 0 & 1 \end{bmatrix} \tag{B.15}$$

The continuous time process noise covariance is given by

$$\mathbf{Q} = \Phi_s \begin{bmatrix} 0 & 0 \\ 0 & 1 \end{bmatrix} \tag{B.16}$$

and using Eq. A.14 the discrete process covariance is

$$\mathbf{Q}_k = \Phi_s \begin{bmatrix} \frac{T^3}{3} & \frac{T^2}{2} \\ \frac{T^2}{2} & T \end{bmatrix} \tag{B.17}$$

Finally, the measurement and measurement covariance matrices are

$$\mathbf{H} = \begin{bmatrix} 1 & 0 \end{bmatrix} \tag{B.18}$$

$$\mathbf{R}_k = \sigma_n^2 \tag{B.19}$$

where σ_n^2 is the variance of the measurement noise.

Wiener Process Acceleration Model

The Wiener Process Acceleration model assumes that the process is given by

$$x = a_0 + a_1 t + a_2 t^2 \tag{B.20}$$

where a_0, a_1, and a_2 are random constants so that the process is parabolic. We model the process as

$$\dot{x} = a_1 + a_2 t \tag{B.21}$$

$$\ddot{x} = a_2 \tag{B.22}$$

$$\dddot{x} = v \tag{B.23}$$

where v is a zero-mean Gaussian distributed variable, i.e. the 'acceleration' of the process is a Wiener process. The state vector is given by

$$\mathbf{x} = \begin{bmatrix} x \\ \dot{x} \\ \ddot{x} \end{bmatrix} \tag{B.24}$$

and the system dynamics matrix is given by

$$\mathbf{F} = \begin{bmatrix} 0 & 1 & 0 \\ 0 & 0 & 1 \\ 0 & 0 & 0 \end{bmatrix} \tag{B.25}$$

Using Eq. A.6 the discrete fundamental matrix is given by

$$\mathbf{\Phi}_k = \begin{bmatrix} 1 & T & 0.5T^2 \\ 0 & 1 & T \\ 0 & 0 & 1 \end{bmatrix} \tag{B.26}$$

The continuous time process noise covariance is given by

$$\mathbf{Q} = \Phi_s \begin{bmatrix} 0 & 0 & 0 \\ 0 & 0 & 0 \\ 0 & 0 & 1 \end{bmatrix} \tag{B.27}$$

and using Eq. A.14 the discrete process covariance is

$$\mathbf{Q}_k = \Phi_s \begin{bmatrix} \frac{T^5}{20} & \frac{T^4}{8} & \frac{T^3}{6} \\ \frac{T^4}{8} & \frac{T^3}{3} & \frac{T^2}{2} \\ \frac{T^3}{6} & \frac{T^2}{2} & T \end{bmatrix} \tag{B.28}$$

Finally, the measurement and covariance matrices are

$$\mathbf{H} = \begin{bmatrix} 1 & 0 & 0 \end{bmatrix} \tag{B.29}$$

$$\mathbf{R}_k = \sigma_n^2 \tag{B.30}$$

where σ_n^2 is the variance of the measurement noise.

APPENDIX C. UNBIASED POLAR-TO-CARTESIAN CONVERSION

In this appendix we present a method to convert polar coordinates that are corrupted by zero-mean noise to Cartesian coordinates. It was shown by Lerro and Bar-Shalom in Ref. (44) that the using the standard polar-to-Cartesian transformation with noisy measurements leads to a bias in the mean of the output and errors in the covariance matrix of the transformed variables. We follow the approach in (45) to prove the existance of the bias and show that it is multiplicative in nature. We then present the unbiased measurement conversion of Ref. (46).

Consider the familiar polar-to-Cartesian conversion

$$x = r\cos\psi \tag{C.1}$$

$$y = r\sin\psi \tag{C.2}$$

Suppose that the measurements of r and ψ contain additive noise. Let the measured quantities be

$$r_m = r + \tilde{r} \tag{C.3}$$

$$\psi_m = \psi + \tilde{\psi} \tag{C.4}$$

where we assume that $\tilde{r}$ and $\tilde{\psi}$ are independent and zero-mean (i.e. $E[\tilde{r}] = E[\tilde{\psi}] = 0$). The standard measurement conversion uses the noisy measurements in Eqs. C.1 and

C.2 to calculate the Cartesian quantities, i.e.

$$x_m = r_m \cos\psi_m = (r + \tilde{r}) \cos(\psi + \tilde{\psi}) \tag{C.5}$$

$$y_m = r_m \sin\psi_m = (r + \tilde{r}) \sin(\psi + \tilde{\psi}) \tag{C.6}$$

Expanding the right hand side we have

$$x_m = r\cos\psi\cos\tilde{\psi} - r\sin\psi\sin\tilde{\psi} + \tilde{r}\cos\psi\cos\tilde{\psi} - \tilde{r}\sin\psi\sin\tilde{\psi} \tag{C.7}$$

$$y_m = r\sin\psi\cos\tilde{\psi} + r\cos\psi\sin\tilde{\psi} + \tilde{r}\sin\psi\cos\tilde{\psi} + \tilde{r}\cos\psi\sin\tilde{\psi} \tag{C.8}$$

At this point we can go no further without making assumptions about the probability distribution function (pdf) of the angle measurement noise $\tilde{\psi}$. The analysis that follows will assume that the probability distribution is symmetric. In this case, $E[\sin\tilde{\psi}] = 0$. Taking expectations of both sides we have

$$E[x_m] = r\cos\psi E[\cos\tilde{\psi}] \tag{C.9}$$

$$E[y_m] = r\sin\psi E[\cos\tilde{\psi}] \tag{C.10}$$

It is clear that if $E[\cos\tilde{\psi}] \neq 1$ there is a bias in the converted measurement and the bias is multiplicative.

The unbiased converted measurement is given by

$$x_{m_u} = \lambda^{-1} r_m \cos\psi_m \tag{C.11}$$

$$y_{m_u} = \lambda^{-1} r_m \sin\psi_m \tag{C.12}$$

where

$$\lambda = E[\cos\tilde{\psi}] \tag{C.13}$$

The elements of the covariance matrix of the converted measurements were shown in

Quantity	$\tilde{\psi}$ Gaussian Distributed	$\tilde{\psi}$ Uniformly Distributed on $[-a, a]$
$E[\cos\tilde{\psi}]$	$e^{-\sigma_{\psi}^2/2}$	$\frac{\sin a}{a}$
$E[\cos 2\tilde{\psi}]$	$e^{-2\sigma_{\psi}^2}$	$\frac{\sin 2a}{2a}$

Table C.1 Parameters required to compute the unbiased measurement conversion for cases where $\tilde{\psi}$ is uniformly and Gaussian distributed.

Ref. (46) to be

$$\begin{aligned}
\mathbf{R}_{11} &= \mathrm{var}(x_{m_u}|r_m, psi_m) \\
&= -\lambda^2 r_m^2 \cos^2\psi_m + \frac{1}{2}(r_m^2+\sigma_r^2)(1+\lambda'\cos 2\psi_m) \qquad \text{(C.14)} \\
\mathbf{R}_{22} &= \mathrm{var}(y_{m_u}|r_m, \psi_m) \\
&= -\lambda^2 r_m^2 \sin^2\psi_m + \frac{1}{2}(r_m^2+\sigma_r^2)(1-\lambda'\cos 2\psi_m) \qquad \text{(C.15)} \\
\mathbf{R}_{12} &= \mathrm{cov}(x_{m_u}, y_{m_u}|r_m, psi_m) \\
&= -\lambda^2 r_m^2 \sin\psi_m\cos\psi_m + \frac{1}{2}(r_m^2+\sigma_r^2)\lambda'\sin 2\psi_m \qquad \text{(C.16)}
\end{aligned}$$

where

$$\lambda' = E[\cos 2\tilde{\psi}] \qquad \text{(C.17)}$$

The values of λ and λ' are given for the case where $\tilde{\psi}$ has uniform and Gassian distributions in Table C.1.

APPENDIX D. THE UNSCENTED TRANSFORMATION

The unscented transformation provides a means to approximate the mean and covariance of a random variable that undergoes a nonlinear transformation. It can be shown that the unscented transformation approximates the true mean and covariance up to third order (49).

Consider an n-element vector $\mathbf{x}$ with a known mean $\bar{\mathbf{x}}$ and covariance $\mathbf{P}$. We wish to find the mean and covariance of $\mathbf{y}$, denoted as $\bar{\mathbf{y}}_u$ and $\mathbf{P}_u$, where $\mathbf{y}$ is given by

$$\mathbf{y} = h(\mathbf{x}) \tag{D.1}$$

The so-called sigma point vectors $\mathbf{x}^{(i)}$ are formed as follows:

$$\mathbf{x}^{(i)} = \bar{\mathbf{x}} + \tilde{\mathbf{x}}^{(i)} \qquad i = 1, \ldots, 2n \tag{D.2}$$

where

$$\tilde{\mathbf{x}}^{(i)} = \left(\sqrt{n\mathbf{P}}\right)_i^T \qquad i = 1, \ldots, n \tag{D.3}$$

$$\tilde{\mathbf{x}}^{(n+i)} = -\left(\sqrt{n\mathbf{P}}\right)_i^T \qquad i = 1, \ldots, n \tag{D.4}$$

Here, $\sqrt{n\mathbf{P}}$ is the square root of $n\mathbf{P}$ so that $\left(\sqrt{n\mathbf{P}}\right)^T \sqrt{n\mathbf{P}} = n\mathbf{P}$ and $\left(\sqrt{n\mathbf{P}}\right)_i$ is the ith row of $\sqrt{n\mathbf{P}}$. The sigma points are then transformed as follows:

$$\mathbf{y}^{(i)} = h(\mathbf{x}^{(i)}) \qquad i = 1, \ldots, n \tag{D.5}$$

The mean and covariance of $\mathbf{y}$ are then approximated by

$$\bar{\mathbf{y}}_u = \frac{1}{2n} \sum_{i=1}^{2n} \mathbf{y}^{(i)} \tag{D.6}$$

and

$$\mathbf{P}_u = \frac{1}{2n} \sum_{i=1}^{2n} \left(\mathbf{y}^{(i)} - \bar{\mathbf{y}}\right) \left(\mathbf{y}^{(i)} - \bar{\mathbf{y}}\right)^T \tag{D.7}$$

BIBLIOGRAPHY

[1] Nicolaides, J.D., Speelman, R.J., and Menard, G.L.C., "A Review of Para-Foil Applications," *Journal of Aircraft*, Vol. 7, No. 5, 1970, pp 423–431.

[2] Knacke, T.W., *Parachute Recovery Systems Design Manual*. Para Publishing, Santa Barbara, California, 1992.

[3] Allen, R.F., "Orion Advanced Precision Airborne Delivery System," AIAA Paper 1995-1539, 1995.

[4] Goodrick, T.T., Pearson, A., and Murphy, A.L., Jr., "Analysis of Various Automatic Homing Techniques for Gliding Airdrop Systems With Comparative Performance in Adverse Winds," AIAA Paper 1973-462, 1973.

[5] Murray, J.E., Sim, A.G., and Neufeld, D.D., "Further Development and Flight Test of an Autonomous Precision Landing System Using a Parafoil," NASA-TM-4599, 1994.

[6] Wailes, W.K., and Harrington, N.E., "The Guided Parafoil Airborne Delivery System Program," AIAA Paper 1995-1538, 1995.

[7] Tavan, S., "Status and Context of High Altitude Precision Aerial Delivery Systems," AIAA Paper 2006-6793, 2006.

[8] Calise, A.J., and Preston, D, "Swarming/Flocking and Collision Avoidance for Mass Airdrop of Autonomous Guided Parafoils," *Journal of Guidance, Control, and Dynamics*, Vol 31, No. 4, 2008, pp 1123–1132.

[9] Jann, T., "Advanced Features for Autonomous Parafoil Guidance, Navigation, and Control," *Journal of Guidance, Control, and Dynamics*, Vol. 31, No. 4, 2008, pp 1123–1132.

[10] Rademacher, B.J., "Minimum Complexity Guidance, Navigation, and Control for an Autonomous Parafoil Payload Delivery System," M.S. Thesis, Iowa State University, 2005.

[11] Soppa, U., Görlach, T., and Roenneke, A.J., "German Contribution to the X-38 CRV Demonstrator in the Field of Guidance, Navigation, and Control (GNC)," *Acta Astronautica*, Vol. 56, 2005, pp. 737–749.

[12] Kaminer, I.I. and Yakimenko, O.A., "Development of Control Algorithm for the Autonomous Gliding Delivery System," AIAA Paper 2003-2116, 2003.

[13] Gimadieva, T.Z., "Optimal Control of a Gliding Parachute System," *Journal of Mathematical Sciences*, Vol. 103, No. 1, 2001.

[14] Hattis, P.D., Campbell, D.P., Carter, D.W, and McConley, M., "Providing Means for Precision Airdrop Delivery from High Altitude," AIAA Paper 2006-6790, 2006.

[15] Slegers, N., Beyer, E., and Costello, M., "Use of Variable Incidence Angle for Glide Slope Control of Autonomous Parafoils," *Journal of Guidance,Control, and Dynamics*, Vol. 31, No. 3, 2008, pp. 585–596.

[16] Dubins, L.E., "On curves of minimal length with a constraint on average curvature and with prescribed initial and terminal positions and tangents," *American Journal of Mathematics*, Vol. 79, No. 3, 1957, pp. 497–516.

[17] Boissonnat, J.D., Cérézo, A., and Leblond, J., "Shortest paths of bounded curvature in the plane," Proceedings of the 1992 IEEE International Conference on Robotics and Automation, Nice, France, 1992.

[18] McGee, T.G., Spry, S. and Hedrick, J.K., "Optimal path planning in a constant wind with a bounded turning rate," AIAA Paper 2005-6186, 2005.

[19] McNeely, R., Iyer, R., and Chandler, P., "Tour Planning for an Unmanned Air Vehicle Under Wind Conditions," *Journal of Guidance, Control, and Dynamics*, Vol 30, No. 5, 2007, pp 1299–1306.

[20] Larson, R.A., Pachter, M. and Mears, M.J., "Path Planning by Unmanned Air Vehicles for Engaging and Integrated Radar Network," AIAA Paper 2005-6191, 2005.

[21] Sussmann, H.J., "Shortest 3-dimensional paths with a prescribed curvature bound," Proceedings of the 34th Conference on Decision & Control, New Orleans, LA, 1995.

[22] Liang, T.C., Liu, J.S., Hung, G.T., and Chang, Y.Z., "Practical and flexible path planning for car-like mobile robot using maximal-curvature cubic spiral," *Robotics and Autonomous Systems*, Vol. 52, 2005, pp. 312–335.

[23] Moll, M. and Kavraki, L.E., "Path Planning for Minimal Energy Curves of Constant Length," Proceedings of the 2004 IEEE International Conference on Robotics & Automation, New Orleans, LA, 2004.

[24] Lu, P. and Chavez, F.R., "Nonlinear Optimal Guidance," AIAA Paper 2006-6087, August 2006.

[25] Crimi, P., "Lateral Stability of Gliding Parachutes," *Journal of Guidance, Control, and Dynamics*, Vol. 13, No. 6, 1990, pp 1060–1063.

[26] Goodrick, T.F., "Scale Effects on Performance of Ram Air Wings," AIAA Paper 1984-783, 1984.

[27] Slegers, N., and Costello, M., "On the Use of Rigging Angle and Canopy Tilt For Control of A Parafoil and Payload System," AIAA Paper 2003-5609, 2003.

[28] Slegers, N. and Costello, M., "Aspects of Control for a Parafoil and Payload System," *Journal of Guidance, Control, and Dynamics*, Vol. 26, No. 6, 2003, pp 898–905.

[29] Iacomini, C.S., and Cerimele, C.J., "Lateral-Directional Aerodynamics From A Large-Scale Parafoil Test Program," AIAA Paper 1999-1731, 1999.

[30] Iacomini, C.S., and Madsen, C.M., "Investigation of Large Parafoil Rigging Angles: Analytical and Drop Test Results," AIAA Paper 1999-1752, 1999.

[31] Iacomini, C.S., and Cerimele, C.J., "Longitudinal Aerodynamics From A Large-Scale Parafoil Test Program," AIAA Paper 1999-1732, 1999.

[32] Lingard, J.S., "Aerodynamics of Gliding Parachutes," Parachute Short Course Handout, University of Minnesota, 1994.

[33] Lissaman, P.B.S., and Brown, G.J., "Apparent Mass Effects on Parafoil Dynamics," AIAA Paper 1993-1236, 1993.

[34] Thomasson, P.G., "Equations of Motion of a Vehicle in a Moving Fluid," *Journal of Aircraft*, Vol. 37, No. 4, 2000, pp. 630–639.

[35] Barrows, T.M., "Apparent Mass of Parafoils with Spanwise Camber," *Journal of Aircraft*, Vol. 39, No. 3, 2002, pp. 445–451.

[36] Brown, G.J., "Parafoil Steady Turn Response to Control Input," AIAA Paper 1993-1241, 1993.

[37] Lingard, J.S., "The Performance and Design of Ram-Air Gliding Parachutes," Royal Aircraft Establishment Technical Report 81103, 1981.

[38] Jardin, M.R., and Erzberger, H., "Atmospheric data acquisition and interpolation for enhanced trajectory-prediction accuracy in the Center-TRACON Automation System," AIAA Paper 2996-271, 1996.

[39] Kelly, K., Peña, B., "Wind Study and GPS Dropsonde Applicability to Airdrop Testing," AIAA Paper 2001-2022, 2001.

[40] Lee, E. B. and Markus, L., *Foundations of Optimal Control Theory*, John Wiley & Sons, New York, 1967, pp. 259–265.

[41] LaValle, S.M., *Planning Algorithms*. Cambridge, New York, New York, 2006, pp. 728–732.

[42] Shkel, A.M., and Lumelsky, V., "Classification of the Dubins Set," *Robotics and Autonomous Sytems*, Vol. 34, No. 4, 2001, pp. 179–202.

[43] "Atmospheric Soundings." *University of Wyoming Department of Atmospheric Science.* Accessed July 3, 2008. <http://weather.uwyo.edu/upperair/sounding.html>.

[44] Lerro, D. and Bar-Shalom, Y., "Tracking With Debiased Consistent Converted Measurements Versus EKF," *IEEE Transactions on Aerospace and Electronic Systems*, Vol. 29, No. 3, 1995, pp 1015–1022.

[45] Longbin, M., and Bar-Shalom, Y., "Unbiased Converted Measurements for Tracking," *IEEE Transactions on Aerospace and Electronic Systems*, Vol. 34, No. 3, 1998, pp 1023–1027.

[46] Duan, Z., Han, C., and Li, X.R., "Comments on 'Unbiased Converted Measurements for Tracking,'" *IEEE Transactions on Aerospace and Electronic Systems*, Vol. 40, No. 4, 2004, pp 1374–1377.

[47] Zarchan, P., and Musoff, H., *Fundamentals of Kalman Filtering: A Practical Approach*, 2nd ed., AIAA Progress in Astronautics and Aeronautics, Vol 208, Reston, Virginia, 2005.

[48] Bar-Shalom, Y., Li, X.R., and Kirubarajan, T., *Estimation with Applications to Tracking and Navigation*. John Wiley & Sons, New York, New York, 2001, pp 272–275.

[49] Simon, D., *Optimal State Estimation: Kalman, H_∞, and Nonlinear Approaches*. John Wiley & Sons, Hoboken, New Jersey, 2006, pp 441-446.